UNIVERSITY OF CALIFORNIA
RIVERSIDE

Towards Highly Scalable, Environmentally Benign, High Performance Silicon-Based Lithium-ion Battery Anodes

A Dissertation submitted in partial satisfaction
of the requirements for the degree of

Doctor of Philosophy

in

Materials Science and Engineering

by

Zachary James Favors

March 2015

Dissertation Committee:
Dr. Cengiz S. Ozkan, Chairperson
Dr. Sandeep Kumar
Dr. Mihrimah Ozkan
Dr. Javier Garay

The Dissertation of Zachary James Favors is approved:

_____

_____

_____

_____

Committee Chairperson

University of California, Riverside

Acknowledgements

I would like to express my sincerest gratitude to all individuals who have assisted me morally, intellectually, or financially throughout my Ph.D. I would first like to show my gratitude for my advisor and co-advisor Dr. Cengiz S. Ozkan and Dr. Mihrimah Ozkan, respectively. They have provided me with the upmost freedom of thought throughout my work, allowing me to pursue any of my own ideas no matter the financial burden. They have provided me with the best energy storage laboratory anyone could ask for. I would also like to thank my committee members Dr. Sandeep Kumar and Dr. Javier Garay for taking the time to serve during my Ph.D. exams and providing me with valuable feedback and insights.

I thank all of my colleagues who have helped me during my Ph.D. in any way possible, whether it was performing characterization, helping with experiments, or simply answering a question. Specifically I thank Dr. Wei Wang for his fruitful collaborations and unwavering guidance in the field of energy storage. Without his help I would not be the scientist I have become in four short years.

Lastly, and most importantly I would like to thank my family and especially my wife Nicole for their undying support emotionally and financially. I thank my family for all of their love and support some 1500 miles away. I thank my wife for putting up with the long hours both in lab and at home, dealing with the stress of graduate school, always supporting my academic dreams, for working long hours to support us financially throughout these demanding four years, and for carrying our first child.

Copyright Acknowledgement

Dedication

This dissertation is dedicated to my parents, Jim and Trish Favors, who have always supported my academic ambitions and fostered my obsession with science and the natural world. Lastly, and certainly not least, I dedicate this dissertation to my wife Nicole for her unwavering love and support over the past five years of undergraduate and graduate studies.

ABSTRACT OF THE DISSERTATION

Towards Highly Scalable, Environmentally Benign, High Performance Silicon-Based Lithium-ion Battery Anodes

by

Zachary James Favors

Doctor of Philosophy, Graduate Program in Materials Science and Engineering
University of California, Riverside, March 2015
Dr. Cengiz S. Ozkan, Chairperson

Silicon-based nanostructures were synthesized and characterized with the ultimate aim of creating a high performance, environmentally benign, and highly scalable material technology for next-generation Li-ion battery (LIB) anodes. Herein, four distinct silicon-based nanomaterials were synthesized and thoroughly characterized including silicon nanowires (SiNWs), silicon dioxide nanotubes (SiO_2 NTs), nano-silicon from beach sand (nano-Si), and silicon nanofibers (SiNFs). Scanning electron microscopy (SEM), transmission electron microscopy (TEM), atomic force microscopy (AFM), cyclic voltammetry (CV), potentiostatic electrochemical impedance spectroscopy (PEIS), and galvanostatic cycling are all notable techniques used to characterize these various materials

Metal assisted chemical etching (MACE) of crystalline silicon wafers is investigated as a means of synthesizing high aspect ratio SiNWs and characterized in the half-cell configuration. Electron beam evaporated gold thin films are used as an etching assistant using *in situ* synthesized anodic aluminum oxide (AAO) templates. A discussion

on the attempted fabrication of silicon nanotubes (SiNTs) is also included using argon sputter redeposition (ASR).

Silicon dioxide is discussed and analyzed as a potential next-generation LIB material in the form of SiO_2 NTs synthesized via chemical vapor deposition (CVD) of polydimethylsiloxane (PMDS) elastomer on anodic aluminum oxide (AAO) templates. SiO_2 NTs produce a highly stable specific capacity of 1266 mAh g^{-1} after 100 cycles with Coulombic efficiencies (CEs) in excess of 98.5%.

Magnesiothermic reduction (MTR) is used to synthesize nano-Si from naturally occurring sand and to fabricate SiNFs from electrospun SiO_2 nanofibers (SiO_2 NFs). Nano-Si delivers a reversible capacity of 1024 mAh g^{-1} after a staggering 1000 cycles at a current density of 2 A g^{-1} with CEs in excess of 99%. The nano-Si technology demonstrates scalability, performance, and environmental benignity rarely reported in literature or industry.

Electrospun SiNFs demonstrate the highest performance of all the structures synthesized herein with a reversible capacity of 802 mAh g^{-1} after 659 cycles while still offering a relatively scalable, non-toxic, and environmentally friendly approach to LIB material synthesis. Elimination of copper current collectors and inactive polymer binders make this technology a candidate for producing a potential leap in LIB performance in lieu of the incremental improvements seen year after year.

Table of Contents

Acknowledgements iv

Copyright Acknowledgement v

Dedication vi

Abstract vii

Table of Contents ix

List of Figures xii

List of Tables xiv

List of Abbreviations xv

Chapter 1: Introduction 1

1.1: A Brief History of the LIB 1

1.2: Impetuses for Adoption of EVs 3

1.3: Next-Generation LIB Candidate Materials 4

1.4: Silicon as an Anode Material 8

1.5: Silicon Synthesis Routes 11

1.6: References 17

Chapter 2: SiNWs and SiNTs via MACE of Si Wafers 23

2.1: Introduction 23

2.2: Synthesis of SiNWs 25

2.3: Characterization of SiNWs 29

2.4: Electrochemical Characterization of SiNWs 30

2.5: Synthesis and Characterization of SiNTs 34

2.6: Conclusions....38
2.7: References....40
Chapter 3: SiO_2 NTs via CVD of PDMS on AAO....41
3.1: Introduction....41
3.2: Synthesis of SiO_2 NTs....44
3.3: Characterization of SiO_2 NTs....46
3.4: Electrochemical Characterization of SiO_2 NTs....53
3.5: Conclusions....57
3.6: References....59
Chapter 4: Nano-Si from Beach Sand via MTR....62
4.1: Introduction....62
4.2: Synthesis of Nano-Si via MTR of Sand....66
4.3: Characterization of Nano-Si....70
4.4: Electrochemical Characterization of Nano-Si....74
4.5: Conclusions....77
4.6: References....79
Chapter 5: Electrospun SiNFs via MTR....82
5.1: Introduction....82
5.2: Synthesis and Characterization of SiNFs....84
5.3: Electrochemical Characterization of SiNFs....91
5.4: Conclusions....96
5.5: References....99

Chapter 6: Full Cell LIB Applications of Nano-Si 101

6.1: Introduction.....101

6.2: Full Cell LIB Preparation and Characterization using Nano-Si 107

6.3: Conclusions 115

6.4: References 116

List of Figures

Figure 1.1 Energy density trend of LIBs 2

Figure 1.2 Potential and capacity of anode and cathode materials 5

Figure 1.3 Relative atomic abundance of elements in the earth's crust and phase diagram of the Li-Si system 9

Figure 1.4 Size-dependent silicon and SEI lithiation phenomenon 11

Figure 1.5 Carbothermic reduction process 12

Figure 2.1 MACE diffusion models.....24

Figure 2.2 SEM of *in situ* synthesized AAO on Si wafer 26

Figure 2.3 SiNW synthesis procedure 28

Figure 2.4 SEM of SiNWs via MACE.....30

Figure 2.5 Cycling data for SiNWs.....31

Figure 2.6 Electrochemical data for SiNWs 33

Figure 2.7 Fabrication procedure for SiNTs and NRs 35

Figure 2.8 SEM of NRs 37

Figure 3.1 Fabrication process for SiO_2 NTs.....46

Figure 3.2 SEM and XRF of SiO_2 NTs.....48

Figure 3.3 SEM and EDS of SiO_2 NTs.....50

Figure 3.4 AFM of SiO_2 NTs.....52

Figure 3.5 BET data for SiO_2 NTs.....53

Figure 3.6 Electrochemical data for SiO_2 NTs 54

Figure 3.7 Post-cycling TEM of SiO_2 NTs.....57

Figure 4.1 Si production roadmap, optical images of sand throughout synthesis process, and schematic of nano-Si synthesis process 65

Figure 4.2 SEM, EDS, and XRD of nano-Si and sand 68

Figure 4.3 TEM and BET data for nano-Si.....72

Figure 4.4 Electrochemical data for nano-Si 75

Figure 5.1 Fabrication process and optical images of SiNFs.....85

Figure 5.2 SEM and XRD of SiNFs 88

Figure 5.3 BET and yield data for SiNFs 89

Figure 5.4 TEM of SiNFs 90

Figure 5.5 Electrochemical data for SiNFs.....93

Figure 6.1 Theoretical CE vs. Cycle relationships 102

Figure 6.2 High versus low capacity anode visualization.....106

Figure 6.3 Prelithiation electrochemical data 109

Figure 6.4 SEM, Raman, and electrochemical data for nano-Si@C 112

Figure 6.5 Cycling data for NMC-Si full cells 113

Figure 6.6 Cycling data for MoO_3-Si full cells.....114

List of Abbreviations

SiNW	silicon nanowire
SiNT	silicon nanotube
SiNF	silicon nanofiber
SiNP	silicon nanoparticle
SiO_2 NT	silicon dioxide nanotube
NR	nanoring
CVD	chemical vapor deposition
AAO	anodic aluminum oxide
PDMS	polydimethylsiloxane
MTR	magnesiothermic reduction
ASR	argon sputter redeposition
SEM	scanning electron microscopy
TEM	transmission electron microscopy
AFM	atomic force microscopy
EDS	energy dispersive x-ray sectroscopy
ICE	internal combustion engine
CE	Coulombic efficiency
CV	cyclic voltammetry
PEIS	potentiostatic electrochemical impedance spectroscopy
LIB	lithium-ion battery
LCO	lithium cobalt oxide

LFP	lithium iron phosphate
NMC	nickel manganese cobalt oxide
NCA	nickel cobalt aluminum oxide
EV	electric vehicle
CNT	carbon nanotube
PGN	pillared graphene nanostructure
MG-Si	metallurgical grade silicon
SEI	solid electrolyte interphase
VLS	vapor liquid solid
AuNM	gold nanomesh
MACE	metal assisted chemical etching
AgNP	silver nanoparticle
IPA	isopropyl alcohol
EtOH	ethanol
DI	deionized
ICP-RIE	inductively coupled plasma-reactive ion etching
HF	hydrofluoric acid
XRD	x-ray diffraction
STEM	scanning transmission electron microscopy
BET	Brunauer-Emmet-Teller
TEOS	tetraethyl orthosilicate
HRTEM	high resolution transmission electron microscopy

Nano-Si@C	core-shell nano-silicon carbon
PAA	poly(acrylic acid)
PVDF	polyvinylidene fluoride
AB	acetylene black
ESR	equivalent series resistance
EC	ethylene carbonate
DMC	dimethyl carbonate
NMP	N-methyl-2-pyrrolidone

Chapter 1: Introduction

1.1 A Brief History of the LIB

The vast majority of commercially available LIBs today comprise a lithium metal oxide cathode ($LiCoO_2$, NCA, etc.) and a graphite anode. The intercalation graphite anode was first proposed by Besenhard and Eichinger in 1976, which led to the first secondary, or rechargeable, Li-ion battery in 1983 by Yazami.[1-3] In 1979 Goodenough developed the reversible $LiCoO_2$ (LCO) cathode, which was paired with graphite by Sony in 1991 to produce the first commercially available LIB.[4] The graphite anode is currently the most widely used anode material in commercially available LIBs today, while cathodes can take on several forms of lithium metal oxides. Since the advent of the first commercial LIB, the materials have by and large remain unchanged, which is especially true of the graphite anode. Graphite is widely used due to its excellent cycle life over thousands of cycles, good conductivity, and relatively low cost in comparison to numerous potential anode materials.[5,6] This investigation will focus on the development of next-generation anode materials that can supersede graphite.

Figure 1.1 displays the trend of increasing battery energy density with respect to time since the advent of the first LIB in 1991 by Sony. While incremental increases in performance have been realized every year, a leap in performance, and one that would make for competition with internal combustion engines (ICEs), has yet to be achieved commercially. The fundamental energy storing materials have largely remained unchanged for over 20 years. The anode still utilizes graphite and many commercial LIBs still use LCO as the cathode material. Enhancements in material purity, synthesis, packing density,

etc. have led to small increases in performance since 1991. However, the incremental pace of performance increase is not sufficient in light of increasing petroleum prices, increasing amounts of atmospheric CO_2, and humanity's large dependence on fossil fuels for energy. A leap in performance is necessary to displace this dependence on ICEs for vehicle propulsion by making LIBs comparably energy dense to gasoline.

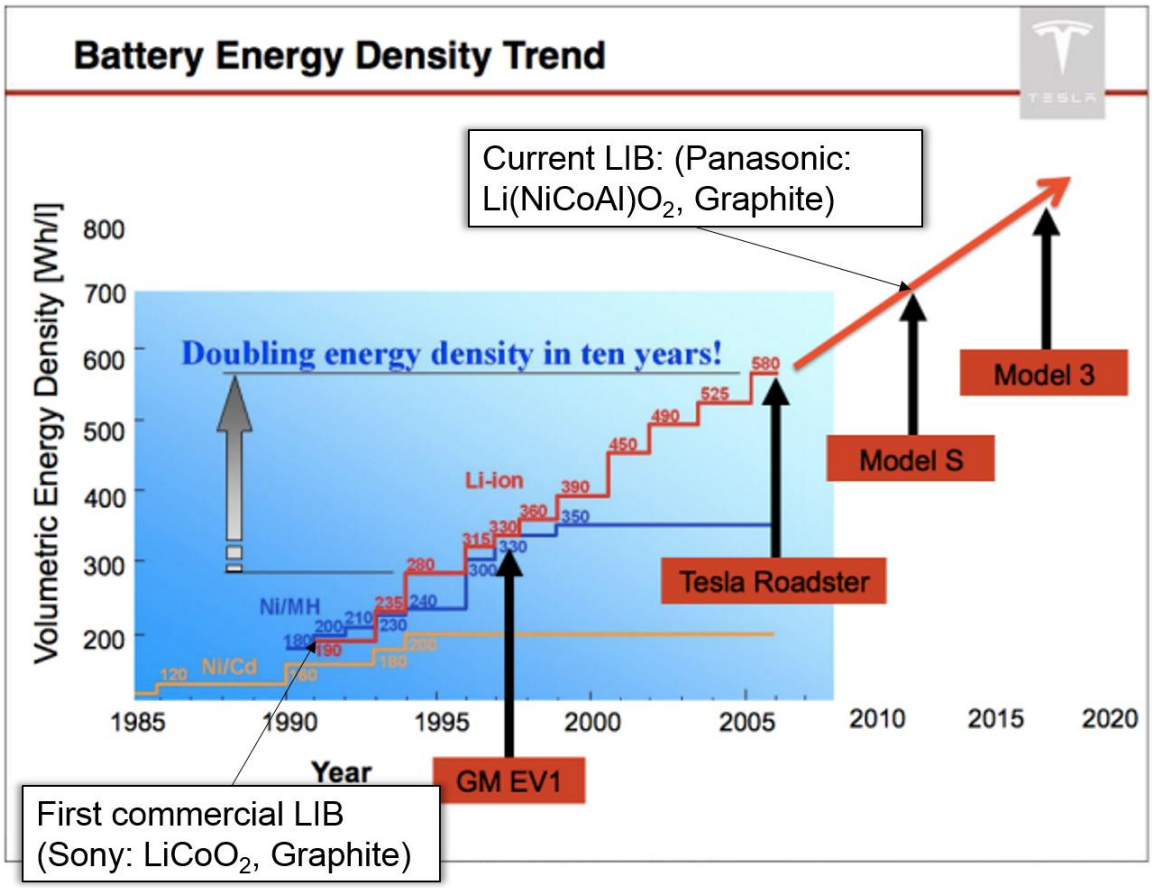

Figure 1.1 Energy density trend of LIBs since the advent of the first LIB in 1991 with notable EVs. (Figure adopted from Tesla)[7]

1.2 Impetuses for Adoption of EVs

While the actual timeline for Peak Oil or the complete exhaustion of earthly oil reserves is one of intense debate and varying opinion, it is true that Peak Oil has not occurred and the exhaustion of oil reserves may not come for at least 150 years.[8] However, the earth does not replenish oil anywhere near the human time scale of energy consumption, thus Peak Oil is inevitable at some point within the coming decades. Advancements in oil and gas exploration have led to a recent US oil and gas boom, which has seen relatively low gas prices at times.[9] However, the price of oil, and hence gasoline, continues to rise on average which will eventually intersect the decreasing price in LIB packs. While the prospect of dwindling oil production not happening for several decades may not be enough of a push for the average consumer to switch to an electric vehicle (EV), the deleterious and measurable environmental impacts of continually burning sequestered carbon and release of CO_2 into the atmosphere is.[10,11] Regardless of the intense debate on climate change, numerous observable phenomena derived from humanity's rigorous fossil fuel diet are occurring in recent times. The measured rise in atmospheric CO_2 levels enhances the greenhouse gas effect occurring in the atmosphere.[12] CO_2 also dissolves in earth's vast oceans leading to acidification, which carries numerous frightening consequences.[13] These CO_2 levels can be measured in ice cores, which has indicated a significantly higher CO_2 level than in the last 800,000 years.; this undoubtedly from the human contribution via combustion of fossil fuels.[14] The subject of renewable energy sources is beyond the immediate scope of this dissertation, but the subject of alternative energy sources for powering vehicles is one this dissertation seeks to address.

The combination of rising oil prices, compounding environmental impacts, and advancements in energy storage technology will slowly provide the impetus for making EVs competitive with ICEs on a cost and performance basis. Present day EVs, such as the Tesla model S and Nissan Leaf suffer from several drawbacks compared to their ICE cousins. The price of LIB packs and the performance of these packs both hinder the widespread adoption of EVs by the general public.[15] Affordable EVs such as the Nissan Leaf are so because the battery banks are smaller and, hence, cost less than pricier EVs such as the Tesla Model S which has a significantly larger battery bank.[16] The price of these LIB packs is dependent on numerous factors including materials (such as graphite, Li, etc.), size of the packs, and the lack of a large scale manufacturing plant that can produce economies of scale to bring the price down. By adding additional cells into a LIB pack, we can increase the range of the EV in an incremental fashion, but this also increases the price of packs incrementally in turn. The materials that comprise the cells are a significant cost contributing factor due to the relatively high cost of Li metal and Li metal ores used to produce the transition metal oxide cathodes.[17] Creating new LIBs with more energy dense materials such as silicon (anode) and sulfur (cathode) would allow for a significant reduction in weight and cost while affording a significant increase in range.

1.3 Next-Generation LIB Candidate Materials

Numerous materials have recently been proposed as replacement materials for graphite as the anode for LIBs, including germanium, tin, 2D-carbon, TiO_2, and silicon. Figure 1.2 displays the approximate theoretical reversible specific capacities, or amount of

electric charge per unit mass, for various anode materials and their respective discharge potentials. The discharge potential refers to the average voltage an anode material outputs when delithiating (discharging). All values are measured versus Li metal, and lower discharge potentials are highly desired to increase the full cell potential; full cell potential is measured by taking the difference between the cathode lithiation voltage and the anode delithiation voltage. While silicon has the highest theoretical specific capacity of 4200 mAh g^{-1}, this is only achievable above the melting temperature of Li.[19] At room temperature the theoretical reversible specific capacity of Si is 3579 mAh g^{-1}, which corresponds to an ambient temperature formation of a $Li_{15}Si_4$ phase.[20]

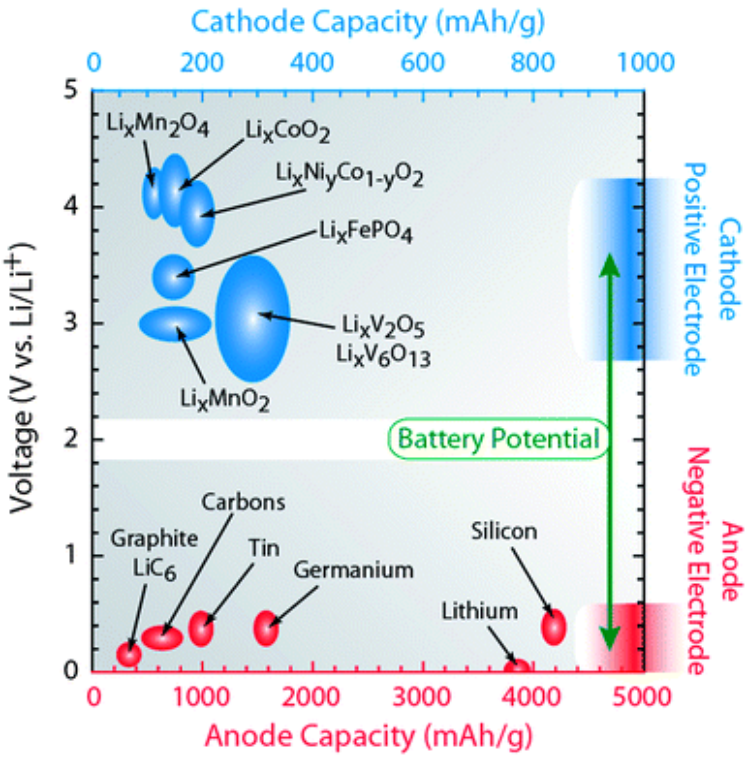

Figure 1.2 Plot displaying various anode and cathode materials plotted according specific capacity and typical operating potential window. Figure taken from [18]

Li metal is the most ideal anode material in terms of electrochemical performance because it has high conductivity as a metal, it is the lightest of all metals, operates via plating in lieu of alloying/intercalation, does not require any specific structuring, and has the highest theoretical specific capacity of 3860 mAh g^{-1}.[21] In terms of safety and processibility, however, Li metal is very much not the ideal anode material. Li metal is highly reactive with moisture and can quickly oxidize in a dry room environment based on its reactivity with oxygen; thus, Li metal must be handled in costly inert atmosphere environments. If a Li metal battery were to be punctured in a real world setting, the risk of fire is significantly increased when compared to conventional LIBs.[22]

Since reversible charging and discharging of Li metal operates on the principle of electrochemical plating, dendrites may form on the surface of Li foil and grow across the battery, resulting in a short circuit.[23] These dendrites also carry a very high specific surface area in comparison to metal foil, which increases their reactivity with the electrolyte and atmosphere, if exposed.[24] This high surface area is also detrimental due to the increased surface area for irreversible reactions with the electrolyte. Currently, Li metal anodes are not used commercially due to the phenomena of low Coulombic efficiency (CE), or the ratio of energy produced, or discharged, by the battery versus the energy charged into the battery.[25] For EV applications, a CE of 99.99% is desired to permit operation to 3000 cycles or more. Current Li metal anodes can only produce CE values between 98-99.5%, which indicates significant irreversible losses with each cycle.[26]

Based on these safety, processibility, and performance issues, anodes such as the ones listed in Figure 1.2 have received serious attention. Numerous carbon allotropes such as graphene, carbon nanotubes (CNTs), fullerenes, carbon nanofibers, pillared graphene nanostructure (PGN), and porous carbon have all been proposed as anode materials.[27-32] These materials benefit from outstanding conductivity, high surface area, and relatively higher capacity compared to graphite. However, many of these structures are produced via chemical vapor deposition (CVD), which is a serial process that cannot produce material at an industrially significant level. The capacity of many of these materials only slightly outperforms that of graphite in comparison to other anode candidates and does not warrant the added processing cost (replacing carbon with carbon).

Germanium, which assumes the same valence state as Si, has the second highest theoretical capacity behind silicon due to its heavier atomic nucleus and thus higher mass. Structures such as nanowires, nanoparticles, and Ge-graphene hybrids have been successfully demonstrated with good electrochemical performance.[33-35] However, the single biggest hindrance that germanium-based materials face is the exorbitant cost of germanium (~$1940.00/kg) compared to other potential high-capacity anode materials such as 98.5% MG-silicon (~$1.86/kg) and tin (~$19.85/kg).[36,37]

Tin (and its oxide) has been proposed as a high capacity anode candidate material based on its theoretical reversible capacity of 992 mAh g^{-1} and high conductivity as a metal. Structures such as nanoparticles, nanowires, nanotubes, and hollow nanospheres have all been demonstrated as high-performance anode materials.[38-41] Tin has the advantage of high conductivity as a metal, non-toxicity, and relatively low cost, but it suffers from significant

volume expansion issues associated with the uptake of large amounts of Li. The low melting temperature of bulk tin (232^{o}C) and nanoscale tin (11 nm, ~177^{o}C) also limits its processibility for any high temperature synthesis or post-treatments such as carbon coating (~900^{o}C).[42] As before, tin is around ten times the cost of MG-Si, making it much less attractive than silicon on an industrial scale.

1.4 Silicon as an Anode Material

Lastly, silicon has garnered significant attention in recent times due to its highest theoretical capacity of 3579 mAh g^{-1}, its high abundance as the second most abundant element in the earth's crust (Figure 1.3a), non-toxicity, low cost, and environmental benignity.[43,44] Silicon is one of the most well-studied elements based on its extensive use in the semiconductor industry, but has only recently gained attention as a possible anode material for LIBs. Numerous structures have been synthesized with excellent electrochemical performance including nanowires, nanospheres, nanotubes, nanoparticles, and thin films.[45-49]

However, Si faces many well-known issues as an anode material including large volume expansion and contraction (up to ~400%) during lithiation and delithiation, relatively high resistivity as a semiconductor (~6.4 x 10^2 Ωm), and degradation of the SEI layer during cycling.[47,50,51] The large volume expansion is associated with the large uptake of Li during charging to a metastable $Li_{3.75}Si$ (Figure 1.3b), which is also responsible for the degradation and reformation of the SEI during cycling (Figure 1.4). The SEI layer cannot contract like Si back to its original form since it does not contain reversibly stored

Li, and thus can fracture and repeatedly expose fresh silicon surface to the electrolyte. This freshly exposed Si surface will generate new SEI, consuming Li-ions and electrolyte. Growth of the SEI layer can significantly reduce Coulombic efficiency below 99.9%, making Si-anodes unfeasible in commercial LIBs.

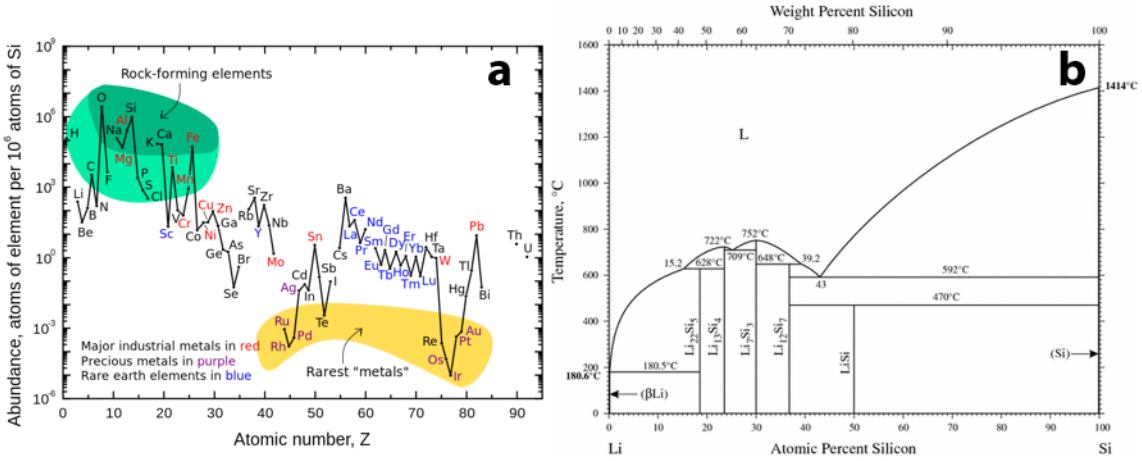

Figure 1.3 (a) Relative atomic abundance of elements in the earth's crust (figure adopted from Haxel, *et al.*).[44] (b) Phase diagram of the Li-Si system (figure adopted from Okamoto).[52]

Besides degradation of the valuable SEI layer, this large volume expansion can pulverize Si active material if it is larger than a critical dimension, as suggested in Figure 1.4b. Liu *et al.* proposed that fracturing of SiNPs can be avoided if the diameter is less than ~150 nm; SiNPs larger than this critical dimension can experience pulverization until the dimension of those new particles is below 150 nm.[53] Ryu *et al.* proposed performed similar work on SiNWs in which they determined the critical dimension for avoiding fracture is ~300 nm.[54] With the added dimension of length in NWs, the hoop stress may be subsequently reduced and thus a larger diameter can be accommodated. These studies show

the importance of structuring the Si well below the micron scale in order to avoid pulverization. Pulverization not only exposes fresh Si surface for new SEI to form, it also deteriorates the mechanical integrity of the electrodes by breaking apart the network of Si, binder, and carbon black. Fractured SiNPs may lose electrical conductivity altogether and move freely about the battery, rendering them electrochemically inactive. When the Si expands and fractures, electrical connectivity may be compromised between electrode material and the current collector or between carbon black and Si.[55]

Silicon is a semiconductor, hence its resistivity (~6.4×10^{2} Ωm) is significantly higher than that of other anode materials such as graphite (~2.5×10^{-6} Ωm) or tin (~1.1×10^{-7} Ωm).[51] In LIBs, we desire the highest electrical conductivity possible in all aspects of the electrodes, including the current collector and active material. In order to increase the conductivity of Si, numerous coatings have been applied to the surface, namely copper or carbon.[56,57] Thus, Si will not be used as a standalone active material in industry, but will rather be used in conjunction with conductive matrices such as carbon.

Okamoto suggested the most Li rich phase at room temperature is $Li_{13}Si_4$ as in Figure 1.3b, but Obravac & Christensen have proven the existence of an even more Li rich metastable crystalline phase of $Li_{15}Si_4$; this is the phase associated with the theoretical room temperature specific capacity of 3579 mAh g^{-1}.[52,58] Many have incorrectly assumed that the theoretical capacity of Si is ~4200 mAh g^{-1} associated with $Li_{21}Si_5$ or $Li_{22}Si_5$, but this has not been confirmed at room temperature as evidenced in the phase diagram in Figure 1.3a.

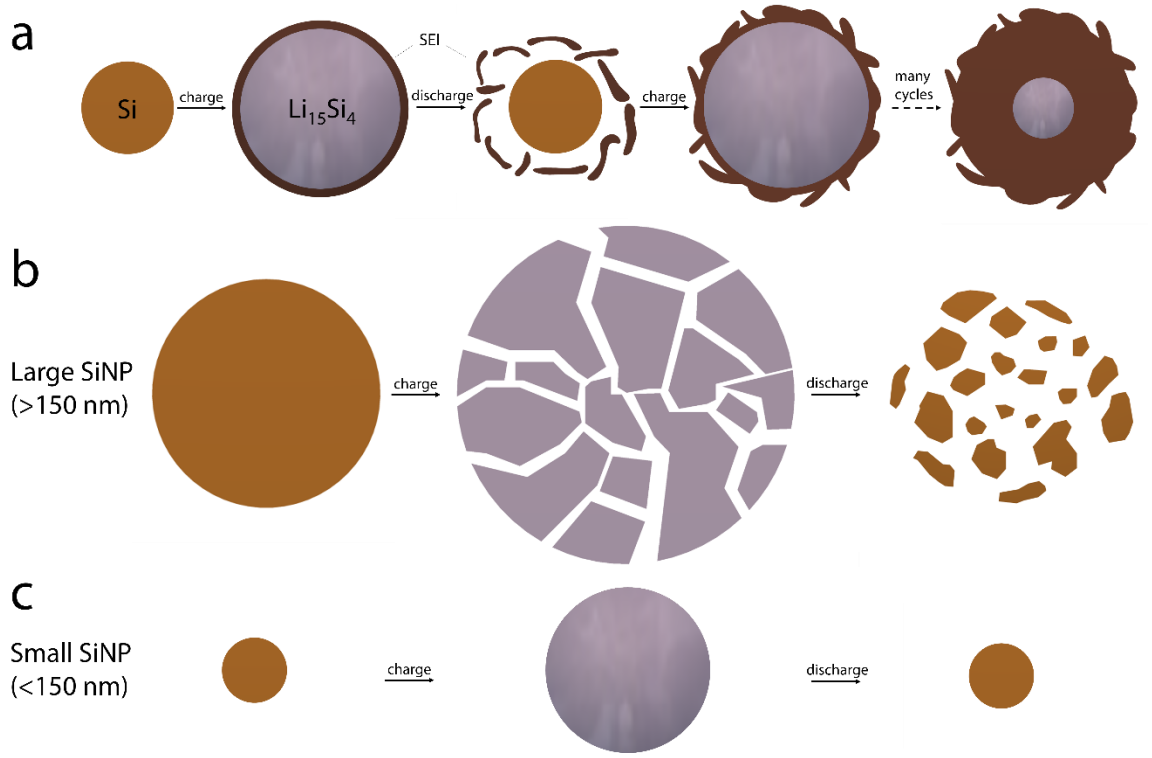

Figure 1.4 (a) Representation of SEI fracture and growth during repeated cycling in Si anodes. Representation of behavior of relatively large Si structures (b) and relatively small Si structures (c) during repeated lithiation/delithiation.

1.5 Silicon Synthesis Routes

The predominant industrial synthesis route for producing silicon is carbothermic reduction. High purity quartzite rock is combined with reducing carbon agents, such as graphite and charcoal, and heated in an electric arc furnace in excess of 2000°C; lab scale demonstrations can produce Si as low as ~1500°C.[59,60] The reaction proceeds generally as in Equation 1.1:

$$SiO_2(s) + 2C(s) \rightarrow Si(s) + 2CO(g) \quad (1.1)$$

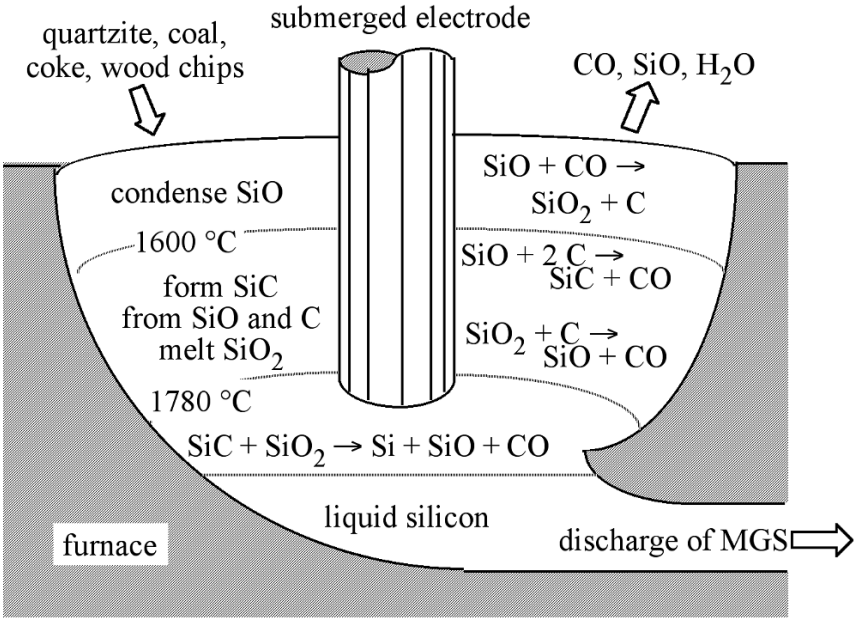

Figure 1.5 Illustration of the carbothermic reduction process as taken from Smith & Barron.[61]

Notably, carbon monoxide (CO) is the main byproduct of this reaction, which is poisonous and reacts with hydroxyl radicals in the atmosphere to produce CO_2, a well-known greenhouse gas.[62] The reaction in itself is not a carbon neutral synthesis route for production of silicon, which is a major concern today due to increasing CO_2 levels in the atmosphere. Molten silicon, categorized as metallurgical grade silicon (MG-Si) at this point, is the predominant species produced from these furnaces. While this synthesis route is capable of producing vast quantities of MG-Si, it requires large amounts of energy and produces several tons of carbonaceous gases per year. Another drawback of this synthesis route is its inability to preserve any original morphology associated with the Si-based precursor, which instead produces bulk silicon with no nanoscale morphology. These Si-

based precursors are usually quartz or quartzite, but recent research has seen more exotic siliceous precursors such as diatomaceous earth, beach sand, and rice husks. [43,63,64]

Aluminothermic reduction is another low temperature route (660°C) for synthesizing MG-Si, which proceeds as in Equation 1.2:

$$3SiO_2(s) + 4Al(s) \rightarrow 3Si(s) + 2Al_2O_3(s) \quad (1.2)$$

Reduction may actually initiate well below the melting point of aluminum at 500°C, which makes aluminothermic reduction a feasible solid state synthesis route for production of Si.[65] This reduction route also avoids the use of carbonaceous reducing agents and is thus carbon neutral in itself. However, deleterious reactions between silica and alumina, in Equation 3, produce mullite in addition to the desired product of alumina:

$$3Al_2O_3(s) + 2SiO_2(s) \rightarrow Al_6Si_2O_{13}(s) \quad (1.3)$$

The presence of mullite and alumina pose significant barriers to purification of the Si given the high difficulty in leaching these minerals.

A third class of thermic reduction, magnesiothermic reduction (MTR), affords another relatively low temperature route (650°C) for synthesizing MG-Si on an industrial scale and has garnered significant attention in recent times. Magnesium is the 8th most abundant element in the earth's crust and is commonly found in rock composed of MgO, which comprises 5.44% of the earth's crust, and in $MgCl_2$ as sea brine.[66] Its relatively high abundance and ease of production make Mg a relatively low cost reducing agent for SiO_2. MTR of SiO_2 proceeds in the following fashion, as in Equation 1.4:

$$2Mg(g) + SiO_2(s) \rightarrow Si(s) + 2MgO(s) \quad (1.4)$$

This reaction is carried out at or slightly above the melting temperature of Mg (650°C), where the vapor pressure of Mg is ~875 torr.[67] While the vapor pressure is lower than that of alkali metals (K and Na) at the same temperature, Mg is easily handled in ambient atmosphere whereas K and Na are highly reactive to moisture and must be dealt with in inert environments. The combination of all of these attributes make Mg an ideal candidate as a reducing agent. One possible deleterious byproduct of MTR is magnesium silicide (Mg_2Si), which is produced when excess Mg is present, as in Equation 1.5. Mg_2Si is not harmful in itself, but poses significant danger during the leaching of MgO (Equation 1.6) after MTR, as in Equation 1.7.

$$2Mg(g) + Si(s) \rightarrow 2Mg_2Si(s) \quad (1.5)$$

$$MgO(s) + 2HCl(l) \rightarrow MgCl_2(aq) + 2H_2O(l) \quad (1.6)$$

$$Mg_2Si(s) + 4HCl(l) \rightarrow SiH_4(g) + 2MgCl_2(aq) \quad (1.7)$$

$$SiH_4(g) + O_2(g) \rightarrow SiO_2(s) + 2H_2O(g) \quad (1.8)$$

The danger arises when silane evolves during HCl etching (Equation 1.8), which is a highly pyrophoric and toxic gas that carries high explosion danger.[68] However, this risk is mitigated by tailoring the molar ratio of Mg to Si such that Mg_2Si is not formed. The desired product, MgO, is easily removed via HCl to form magnesium chloride ($MgCl_2$), which may be recycled back into Mg via electrolysis; this is the predominant industrial route for synthesizing Mg from brine.[69] Aside from the energy used to initiate the reduction, MTR is a completely carbon neutral reaction which is highly important when considering a materials synthesis method on an industrial scale. The lower energy

consumption via the lower operating temperatures and carbon neutral nature of MTR make it a much more favorable production route than carbothermic reduction.

Another phenomenon that must be taken into account is the homogeneity of the reduction products with respect to the layout of the reduction setup. Several groups have synthesized silicon from SiO_2 by relying on the vaporization of Mg and transport of that Mg gas downstream to the SiO_2 species.[63,70] The Mg powder is placed adjacent to the SiO_2 powder in order to prevent an excessive buildup of heat during the exothermic reaction. While this solves one problem, another arises in lack of homogeneity of reaction products. Richman *et al.* reported that an excess of Mg nearest the SiO_2 created unwanted Mg_2Si, while a deficiency in Mg farthest from the SiO_2 did not fully reduce silica to silicon.[70] The presence of Mg_2Si and unreacted SiO_2 significantly reduces the overall yield of the process since these products must be leached. Additionally, only small quantities of reactants can be used due to the inability to dissipate the large amount of heat generated. Both of these issues must be resolved in order for MTR to become an industrially viable synthesis route.

Another less commonly known low-temperature reduction route uses another alkali earth metal, calcium, to reduce silica into silicon (Equation 1.9):

$$2Ca(s) + SiO_2(s) \rightarrow Si(s) + 2CaO(s) \quad (1.9)$$

The operating temperatures for this reduction are slightly higher than those required for MTR but still significantly lower than those for carbothermic reduction. Similarly to MTR, the reaction products can be facilely removed via acid treatments. However, calcium metal is highly reactive, flammable, hazardous to the health of personnel, and must be kept under inert atmosphere. In contrast, magnesium metal can be facilely handled in ambient

atmosphere in bulk or powder form due to its low reactivity, flammability, and health hazard. For these reasons, MTR is a much more viable reduction route than calciothermic reduction.

1.6 References

1 Besenhard, J. O. & Eichenger, G. High energy density lithium cells: Part I. Electrolytes and anodes. *J. Electroanal. Chem. Interfacial Electrochem.* **68**, 1-18 (1976).

2 Eichinger, G. & Besenhard, J. O. High energy density lithium cells: Part II. Cathodes and complete cells. *J. Electroanal. Chem. Interfacial Electrochem.* **72**, 1-31 (1976).

3 Yazami, R. & Touzain, P. A reversible graphite-lithium negative electrode for electrochemical generators. *J. Power Sources* **9**, 365-371 (1983).

4 Mizushima, K., Jones, P. C., Wiseman, P. J. & Goodenough, J. B. Li_xCoO_2 ($0<x<-1$): A new cathode material for batteries of high energy density. *Mater. Res. Bull.* **15**, 783-789 (1980).

5 Fukuda, K., Kikuya, K., Isono, K. & Yoshio, M. Foliated natural graphite as the anode material for rechargeable lithium-ion cells. *J. Power Sources* **69**, 165-168 (1997).

6 Lu, M., Cheng, H. & Yang, Y. A comparison of solid electrolyte interphase (SEI) on the artificial graphite anode of the aged and cycled commercial lithium ion cells. *Electrochim. Acta* **53**, 3539-3546 (2008).

7 Straubel, J. B. *Tesla: Southern California Energy Summit*, URL: http://www.slideshare.net/larkly/teslas-jc-straubel-at-sces2014-future-of-evs-gigafactories-battery-storage-and-the-grid. (2014).

8 Chapman, I. The end of Peak Oil? Why this topic is still relevant despite recent denials. *Energy Policy* **64**, 93-101 (2014).

9 Lento, C. J. Shifting Sands: An Analysis of OPEC Under US Antitrust and EU Competition Law and How the US Oil Boom Might Change It All. *LSU Journal of Energy Law and Resources* **2**, 6 (2014).

10 Verspagen, J. M., Van de Waal, D. B., Finke, J. F., Visser, P. M. & Huisman, J. Contrasting effects of rising CO_2 on primary production and ecological stoichiometry at different nutrient levels. *Ecol. Lett.* **17**, 951-960 (2014).

11 Kunnas, J. *et al.* Counting carbon: historic emissions from fossil fuels, long-run measures of sustainable development and carbon debt. *Scand. Econ. Hist. Rev.* **62**, 243-265 (2014).

12 Rodhe, H. A comparison of the contribution of various gases to the greenhouse effect. *Science*, 1217-1219 (1990).

13 Doney, S. C., Fabry, V. J., Feely, R. A. & Kleypas, J. A. Ocean acidification: the other CO_2 problem. *Mar. Sci.* **1** (2009).

14 Lüthi, D. *et al.* High-resolution carbon dioxide concentration record 650,000–800,000 years before present. *Nature* **453**, 379-382 (2008).

15 Kodjak, D. Consumer acceptance of electric vehicles in the US. *USA: The International Council for Clean Transportation* (2012).

16 Hayes, J. G., de Oliveira, R. P. R., Vaughan, S. & Egan, M. G. in *Vehicle Power and Propulsion Conference (VPPC), 2011 IEEE.* 1-5 (IEEE).

17 Scrosati, B. & Garche, J. Lithium batteries: Status, prospects and future. *J. Power Sources* **195**, 2419-2430 (2010).

18 Landi, B. J., Ganter, M. J., Cress, C. D., DiLeo, R. A. & Rafaelle, R. P. Carbon nanotubes for lithium ion batteries. *Energy Environ. Sci.* **2**, 638-654 (2009).

19 Ding, N. *et al.* Improvement of cyclability of Si as anode for Li-ion batteries. *J. Power Sources* **192**, 644-651 (2009).

20 Chou, S.-L. *et al.* Enhanced reversible lithium storage in a nanosize silicon/graphene composite. *Electrochem. Commun.* **12**, 303-306 (2010).

21 Xu, W. *et al.* Lithium metal anodes for rechargeable batteries. *Energy Environ. Sci.* **7**, 513-537 (2014).

22 Lisbona, D. & Snee, T. A review of hazards associated with primary lithium and lithium-ion batteries. *Process Saf. Environ.* **89**, 434-442 (2011).

23 Tarascon, J.-M. & Armand, M. Issues and challenges facing rechargeable lithium batteries. *Nature* **414**, 359-367 (2001).

24 Xu, K. Nonaqueous liquid electrolytes for lithium-based rechargeable batteries. *Chem. Rev.* **104**, 4303-4418 (2004).

25 Aurbach, D., Zinigrad, E., Cohen, Y. & Teller, H. A short review of failure mechanisms of lithium metal and lithiated graphite anodes in liquid electrolyte solutions. *Solid State Ionics* **148**, 405-416 (2002).

26 Seki, S. *et al.* Reversibility of lithium secondary batteries using a room-temperature ionic liquid mixture and lithium metal. *Electrochem. Solid-State Lett.* **8**, A577-A578 (2005).

27 Wang, W. *et al.* Pillared CNT and Graphene Nanostructure for Lithium Ion Battery Anode. *Nano Energy* (2013).

28 Wu, Y., Reddy, M. V., Chowdari, B. V. R. & Ramakrishna, S. Long-Term Cycling Studies on Electrospun Carbon Nanofibers as Anode Material for Lithium Ion Batteries. *ACS Appl. Mater. Interfaces* **5**, 12175-12184 (2013).

29 Arie, A. A., Song, J. O. & Lee, J. K. Structural and electrochemical properties of fullerene-coated silicon thin film as anode materials for lithium secondary batteries. *Mater. Chem. Phys.* **113**, 249-254 (2009).

30 Chen, Y. e. a. Hollow Carbon-Nanotube/Carbon-Nanofiber Hybrid Anodes for Li-Ion Batteries. *J. Am. Chem. Soc.* **135**, 16280-16283 (2013).

31 Tian, W. Q. e. a. Hierarchical porous carbon spheres as an anode material for lithium ion batteries. *R. Soc. Chem. Adv.* **3**, 10823-10827 (2013).

32 Lian, P. *et al.* Large reversible capacity of high quality graphene sheets as an anode material for lithium-ion batteries. *Electrochem. Acta* **55**, 3909-3914 (2010).

33 Kennedy, T. e. a. High-Performance Germanium Nanowire-Based Lithium-Ion Battery Anodes Extending over 1000 Cycles Through in Situ Formation of a Continuous Porous Network. *Nano Lett.* **14**, 716-723 (2014).

34 Jo, G., Choi, I., Ahn, H. & Park, M. Binder-free Ge nanoparticles–carbon hybrids for anode materials of advanced lithium batteries with high capacity and rate capability. *Chem. Commun.* **48**, 3987-3989 (2012).

35 Ren, J. G. *et al.* Germanium–graphene composite anode for high-energy lithium batteries with long cycle life. *J. Mater. Chem. A* **1**, 1821-1826 (2013).

36 Reuters, T. *Commodity Cash Prices*, URL: http://www.financialpost.com/markets/data/commodity-cash_prices.html. (2014).

37 *Silicon Metal- 98.5%*, URL: http://www.metalprices.com/metal/silicon/silicon-metal-98-5-china. (2014).

38 Zhang, W. M. e. a. Tin-Nanoparticles Encapsulated in Elastic Hollow Carbon Spheres for High-Performance Anode Material in Lithium-Ion Batteries. *Adv. Mater.* **20**, 1160-1165 (2008).

39 Kim, J.-H., Khanal, S., Islam, M., Khatri, A. & Choi, D. Electrochemical characterization of vertical arrays of tin nanowires grown on silicon substrate as anode materials for lithium rechargeable microbatteries. *Electrochem. Commun.* **10**, 1688-1690 (2008).

40 Chen, P., Wu, F. & Wang, Y. Four-Layer Tin–Carbon Nanotube Yolk–Shell Materials for High-Performance Lithium-Ion Batteries. *Chem. Sus. Chem.* **7**, 1407-1414 (2014).

41 Han, S., Jang, B., Kim, T., Oh, S. M. & Hyeon, T. Simple Synthesis of Hollow Tin Dioxide Microspheres and Their Application to Lithium-Ion Battery Anodes. *Adv. Funct. Mater.* **15**, 1845-1850 (2005).

42 Jo, Y. H., Jung, I., Choi, C. S., Kim, I. & Lee, H. M. Synthesis and characterization of low temperature Sn nanoparticles for the fabrication of highly conductive ink. *Nanotechnology.* **22** (2011).

43 Favors, Z. *et al.* Scalable Synthesis of Nano-Silicon from Beach Sand for Long Cycle Life Li-ion Batteries. *Sci. Rep.* **4** (2014).

44 Haxel, G. B., Hendrick, J. B. & Orris, G. J. *Rare Earth Elements—Critical Resources for High Technology*, (2005).

45 Ge, M., Rong, J., Fang, X. & Zhou, C. Porous Doped Silicon Nanowires for Lithium Ion Battery Anode with Long Cycle Life. *Nano Lett.* **12**, 2318-2323 (2012).

46 Yao, Y. *et al.* Interconnected Silicon Hollow Nanospheres for Lithium-Ion Battery Anodes with Long Cycle Life. *Nano Lett.* **11**, 2949-2954 (2011).

47 Wu, H. *et al.* Stable cycling of double-walled silicon nanotube battery anodes through solid-electrolyte interphase control. *Nat. Nanotechnol.* **7**, 310-315 (2012).

48 Ge, M. *et al.* Scalable preparation of porous silicon nanoparticles and their application for lithium-ion battery anodes. *Nano Res.* **6**, 174-181 (2013).

49 Yu, C. e. a. Silicon Thin Films as Anodes for High-Performance Lithium-Ion Batteries with Effective Stress Relaxation. *Adv. Energy Mater.* **2**, 68-73 (2011).

50 Zhao, K. e. a. Concurrent Reaction and Plasticity during Initial Lithiation of Crystalline Silicon in Lithium-Ion Batteries. *J. Electrochem. Soc.* **159**, A238-A243 (2012).

51 Serway, R. A. *Principles of Physics*. 2nd edn, (Saunders College Division, 1998).

52 Okamoto, H. Li-Si (lithium Silicon). *J. Phase Equilib. Diff.* **30**, 118-119 (2009).

53 Liu, X. H. *et al.* Size-Dependent Fracture of Silicon Nanoparticles During Lithiation. *ACS Nano* **6**, 1522-1531 (2012).

54 Ryu, I., Choi, J. W., Cui, Y. & Nix, W. D. Size-dependent fracture of Si nanowire battery anodes. *J.Mech. Phys. Solids* **59**, 1717-1730 (2011).

55 Park, Y. e. a. A photo-cross-linkable polymeric binder for silicon anodes in lithium ion batteries. *RSC Adv.* **3**, 12625-12630 (2013).

56 Murugesan, S., Harris, J. T., Korgel, B. A. & Stevenson, K. J. Copper-Coated Amorphous Silicon Particles as an Anode Material for Lithium-Ion Batteries. *Chem. Mater.* **24**, 1306-1315 (2012).

57 Dimov, N., Kugino, S. & Yoshio, M. Carbon-coated silicon as anode material for lithium ion batteries: advantages and limitations. *Electrochem. Acta* **48**, 1579-1587 (2003).

58 Obravac, M. N. & Christensen, L. Structural Changes in Silicon Anodes during Lithium Insertion/Extraction. *Electrochem. Solid-State Lett.* **7**, A93-A96 (2004).

59 Khalafalla, S. E. & Haas, L. A. Kinetics of Carbothermal Reduction of Quartz Under Vacuum. *J. Am. Ceram. Soc* **55**, 414-417 (1972).

60 Hutchison, S. G., Richardson, L. S. & Wai, C. M. Carbothermic reduction of silicon dioxide- a thermodynamic investigation. *Metall. Mater. Trans. B* **19**, 249-253 (1988).

61 Smith, C. & Barron, A. R. Synthesis and Purification of Bulk Semiconductors. *Connexions* (2009).

62 Reeves, C. E. e. a. Potential for photochemical ozone formation in the troposphere over the North Atlantic as derived from aircraft observations during ACSOE. *J. Geophys. Res* **107**, ACH 14-11 -ACH 14-14 (2002).

63 Liu, N., Huo, K., McDowell, M. T., Zhao, J. & Cui, Y. Rice husks as a sustainable source of nanostructured silicon for high performance Li-ion battery anodes. *Sci. Rep.* **3** (2013).

64 Luo, W. *et al.* Efficient Fabrication of Nanoporous Si and Si/Ge Enabled by a Heat Scavenger in Magnesiothermic Reactions. *Sci. Rep.* **3** (2013).

65 Deqing, W. & Ziyuan, S. Aluminothermic Reduction of Silica for Synthesis of Alumina-Aluminum-Silicon Composite. *J. Mater. Synth. Process.* **9** (2001).

66 Yaroshevsky, A. A. Abundances of Chemical Elements in the Earth's Crust. *Geochem. Int.* **44**, 48-55 (2006).

67 Smith, J. & Smythe, R. Vapor pressure measurements over calcium, magnesium and their alloys and the thermodynamics of formation of CaMg 2. *Acta Metallurgica* **7**, 261-267 (1959).

68 Kondo, S., Tokuhashi, K., Nagai, H., Iwasaka, M. & Kaise, M. Spontaneous ignition limits of silane and phosphine. *Combust. Flame* **101**, 170-174 (1995).

69 Kipouros, G. J. & Sadoway, D. R. The chemistry and electrochemistry of magnesium production. *Adv. Molt. Salt Chem.* **6**, 127-209 (1987).

70 Richman, E. K., Kang, C. B., Brezesinski, T. & Tolbert, S. H. Ordered Mesoporous Silicon through Magnesium Reduction of Polymer Templated Silica Thin Films. *Nano Lett.* **8**, 3075-3079 (2008).

Chapter 2: SiNWs and SiNTs via MACE of Si Wafers

2.1 Introduction

One of the first appearances of nano-Si in LIBs was demonstrated in 2007 by Chan *et al.* in the form of CVD grown silicon nanowires (SiNWs).[1] Using AuNP catalysts and silane as a gaseous Si precursor, SiNWs were grown via the vapor-liquid-solid (VLS) phenomena. Shortly thereafter, significant attention was focused on the synthesis of SiNWs using various synthesis techniques. The major drawback of Chan *et al.*'s synthesis technique is the complete lack of scalability. Microgram level batches of SiNWs can only be synthesized via CVD using silane in this manner, despite the excellent electrochemical performance that was demonstrated over a few cycles. An alternative method to synthesizing these high aspect ratio SiNWs that has been extensively studied in this dissertation and elsewhere is metal assisted chemical etching (MACE) of crystalline Si wafers.[2,3]

As mentioned, MG-Si is predominantly produced via carbothermic reduction, which is the main starting point for all Si-based precursors and chemicals. After quartzite is reduced into MG-Si, the silicon may be used in several avenues of production for various Si-based gases, liquids, and solids. One of the most common uses of MG-Si is in the semiconductor industry for production of solar cells or silicon wafers. MG-Si undergoes significant purification to increase the purity level depending on the application, which in turn adds significant cost to the final high-purity silicon product. Significant research has been done on metal assisted chemical etching (MACE) of single crystal silicon wafers of varying dopant densities, dopant types, and crystal orientations.[4]

MACE involves the physical or chemical deposition of a noble metal (Ag, Au, Pd, or Pt) onto the wafer with subsequent chemical etching in an HF-based solution. Ge *et al.* synthesized highly porous doped silicon nanowires via MACE using Ag as the charge injection agent.[5] It is believed that dopants (P, As, B) serve as pore nucleation sites during MACE, which results in a highly porous SiNW. These pores serve as effective volume expansion buffer sites that absorb the large volume increase experienced during lithiation. Briefly, Ag^+ dissolved in an HF solution as $AgNO_3$ precipitates into silver nanoparticles (AgNPs) on the surface of the wafer. A solution comprising HF:H_2O_2 then chemically etches the oxidized Si underneath the AgNPs, essentially drilling vertically down through the surface of the wafer in the favored [100] direction (Figure 1.6).[3] Despite the outstanding performance and template-free nature of this process, the silicon wafers are entirely too expensive to make this a feasible synthesis route for nano-Si. Additionally, the amount of material produced is on the order of milligrams per wafer, as discovered in this investigation.

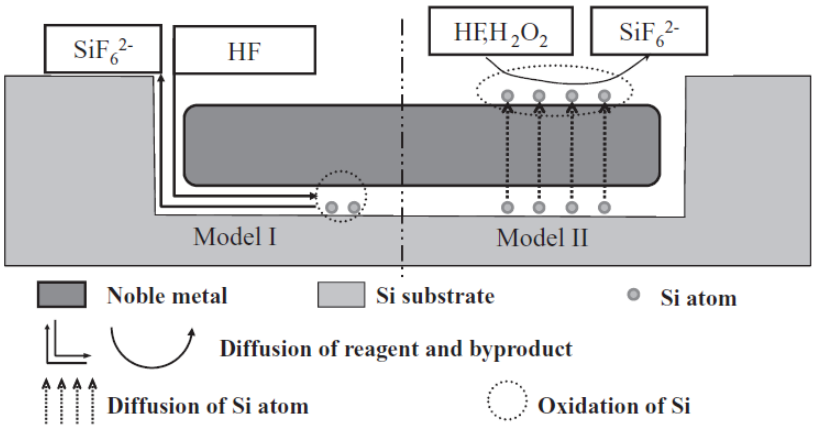

Figure 2.1 Schematic of two possible diffusion models that may occur during MACE. (Reproduced from Huang *et al.*)[4]

Despite these drawbacks, MACE of highly doped Si wafers was investigated as means of potentially producing on-chip LIBs. In contrast to other published SiNWs produced via CVD and MACE, herein I have synthesized SiNWs using a highly controllable template-assisted MACE procedure using an Au etching assistant. Briefly, an *in situ* anodic aluminum oxide (AAO) template was synthesized on-wafer to control the diameter and density of SiNWs with a narrow size distribution. This is in contrast to the relatively uncontrolled etching of Si wafers using chemically deposited AgNPs.

2.2 Synthesis of SiNWs

Herein, high aspect ratio silicon nanowires have been synthesized via template-assisted MACE of crystalline Si wafers. Highly doped n-type (As-doped) Si wafers were first rinsed with acetone and IPA to remove organic residue and then submerged in 5% HF for 30 seconds to remove the native oxide and to hydrogen terminate the surface of the wafer. Hydrogen termination provides better adhesion between the evaporated metal and wafer. Wafers were immediately transferred to an electron beam evaporator and the chamber was pumped down to 10^{-7} torr. Once under vacuum, 120 nm of aluminum was evaporated onto the wafer at a rate of 2 Å/s and left to cool for 10 min. Al-coated wafers we then connected to the positive terminal of a DC voltage supply via alligator clip as the cathode and a platinum wire electrode was connected to the negative side as the anode. The platinum wire and wafer were submerged in a 1M oxalic acid solution under vigorous stirring. Vigorous stirring is necessary to avoid local accumulation of heat while anodizing, which may damage the surface, and to sweep away reaction products while bringing fresh

solution to the anodization sites. A 40 V potential was then applied across the electrodes with a multimeter connected in series to detect when anodization had finished. Anodization takes ~30 seconds to fully anodize the aluminum film, which highlights the rapid template production process. Once anodized, the wafers are immediately washed with DI water to remove oxalic acid and then transferred to a 1M H_3PO_4 bath to soak for 1 hour. Soaking in this phosphoric acid bath allows for controlled widening of the pores in the AAO; anodization alone is not enough to produce wide enough pores for further processing. After pore widening the wafers are again rinsed with DI water to remove acid and dried under nitrogen stream. Typical AAO templates synthesized under these conditions can be seen in Figure 2.2a and 2.2b, and the pore diameter is 75 nm on average.

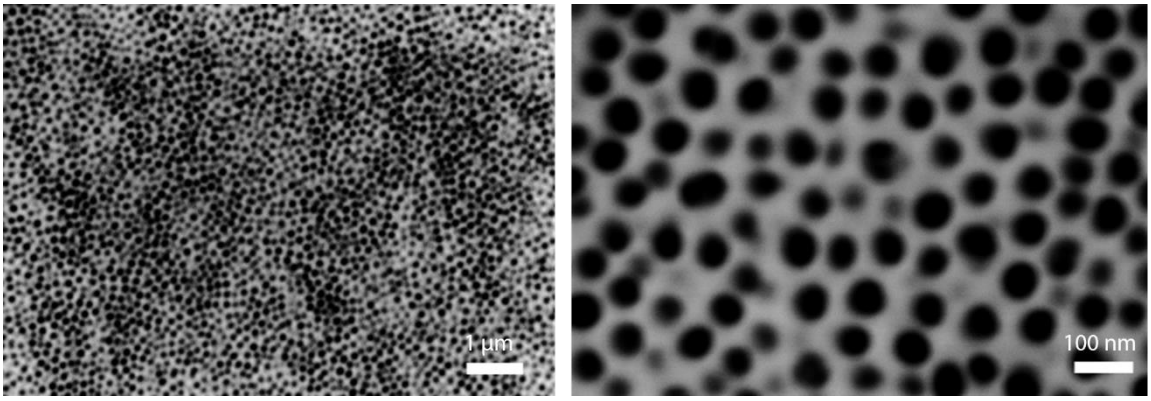

Figure 2.2 (a) SEM image of *in situ* synthesized AAO on Si wafer. (b) Higher magnification SEM image showing pore diameters.

AAO-coated wafers are transferred back into the e-beam evaporator and vacuumed down to 10^{-7} torr as before. Then 15 nm of Au is evaporated perpendicular to the wafer surface at a rate of 1 Å/s. The Au film takes on the porous geometry of the AAO, thus forming a Au nanomesh (AuNM). Au is also evaporated down the pores of the AAO to

form AuNPs, but these NPs do not etch at the same rates as the relatively larger AuNM. Wafers are then transferred to a 1.2% H_2O_2 and 10% HF 4:1 EtOH:H_2O bath to etch for select times. The HF immediately etches the AAO template from underneath the AuNM, which allows the AuNM to precipitate on the surface of the Si wafer to begin MACE. The AuNM etches vertically along the preferred [100] direction since it is the fastest etching direction in Si. Any silicon that is in contact with the AuNM will become oxidized and etched away by the etching solution; any areas not in direct contact with the AuNM will become SiNWs.

The addition of ethanol to the etching bath is critical for liberating the large amount of hydrogen generated during etching of Si and ensures sufficient wetting of the aqueous solution in between the dense forest of SiNWs. Unfortunately, as the AuNM etches deeper into the wafer it becomes increasingly difficult to supply fresh etchant to the AuNM while sweeping away reaction products. Thus, etching slows down the further into the wafer the AuNM goes and becomes increasingly heterogeneous. An equally troublesome phenomenon arises known as hydrogen bubble coalescence, which can destroy the wafer, SiNWs, and AuNM via violent microscopic explosions.[6] As Si is oxidized and etched during MACE, microscopic hydrogen bubbles evolve and can eventually grow into larger bubbles via coalescence, or joining, of two smaller H_2 bubbles into a larger H_2 bubble. The coalescence of two H_2 bubbles produces interfacial velocities that far exceed the length scale of the surrounding structures. These super high interfacial velocities push the surrounding fluid out in a violent and sudden burst which can create impact craters that are a result of both the immense pressure and heat generated in conjunction with etching

underneath these bigger H_2 bubbles. The sticking of H_2 bubbles to Si and the subsequent coalescence can wreak havoc on the etching homogeneity across the wafer and throughout the etching duration. The entire fabrication process for SiNWs can be visualized in Figure 2.3 below.

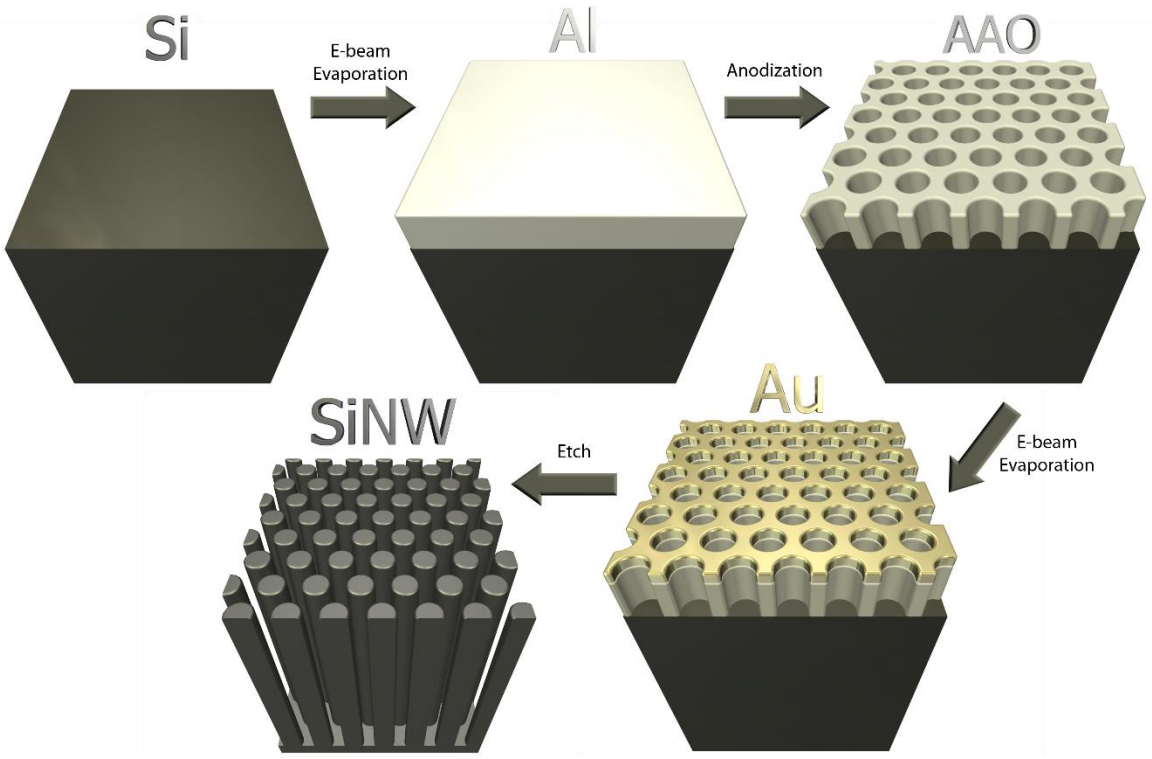

Figure 2.3 Schematic representation of the SiNW synthesis procedure.

While it is possible to produce dense forests of SiNWs across the entire wafer surface, each wafer can only produce usable SiNW powder on the order of a few milligrams, as mentioned prior. This is again due to the increasingly sluggish pace of the etching reaction as the AuNM proceeds deeper into the wafer. Additionally, single crystal silicon wafers are relatively costly in comparison to the MG-Si from whence it was derived. Despite the good electrochemical performance of SiNWs, the inability to produce material

on an industrially significant level coupled with the high costs associated with the starting wafers make this technology unfeasible in a real world setting.

2.3 Characterization of SiNWs

SiNWs were characterized via SEM in Figure 2.4, revealing the high density of SiNWs on wafer and the remarkable flexibility of these nanoscale structure. Despite silicon's high stiffness and brittleness in bulk form, at the nanoscale these SiNWs demonstrate the ability to be bent 180^{o} without any sign of fracture. This is due to the critical dimension, or diameter, of the SiNWs being smaller than the minimum crack propagation distance required to fracture a SiNW.[7] Figure 2.4b shows 2 individual SiNWs revealing a diameter of ~75 nm. Figure 2.4c shows a forest of SiNWs still anchored to the wafer after a 1 hour etch, while Figure 2.4d shows a shorter etching time of 30 minutes. The AuNM can be seen at the base of the SiNWs in Figure 2.4d indicated by the bright white film at the floor of the forest. The SiNWs tend to form bundles simply due to the drying of the wafers after etching. When etchant is washed and then dried from in between the SiNWs a capillary force is exerted due to the surface tension of the liquid in between. This meniscus, which produces a non-negligible surface tension, produces enough force to bend the SiNWs inward toward each other until they stick via van der Waals forces.[8]

Unfortunately, SiNWs beyond 15-20 μm in length were never demonstrated even after several hours of MACE. This highlights the lack of scalability that this technology affords due to the increasingly slowing pace of etching. Four inch wafers were only able to produce a few tens of milligrams of material per wafer, which is not significant enough

given the high cost of the wafers and extensive fabrication steps. However, this material does achieve outstanding electrochemical performance as highlighted in the next section.

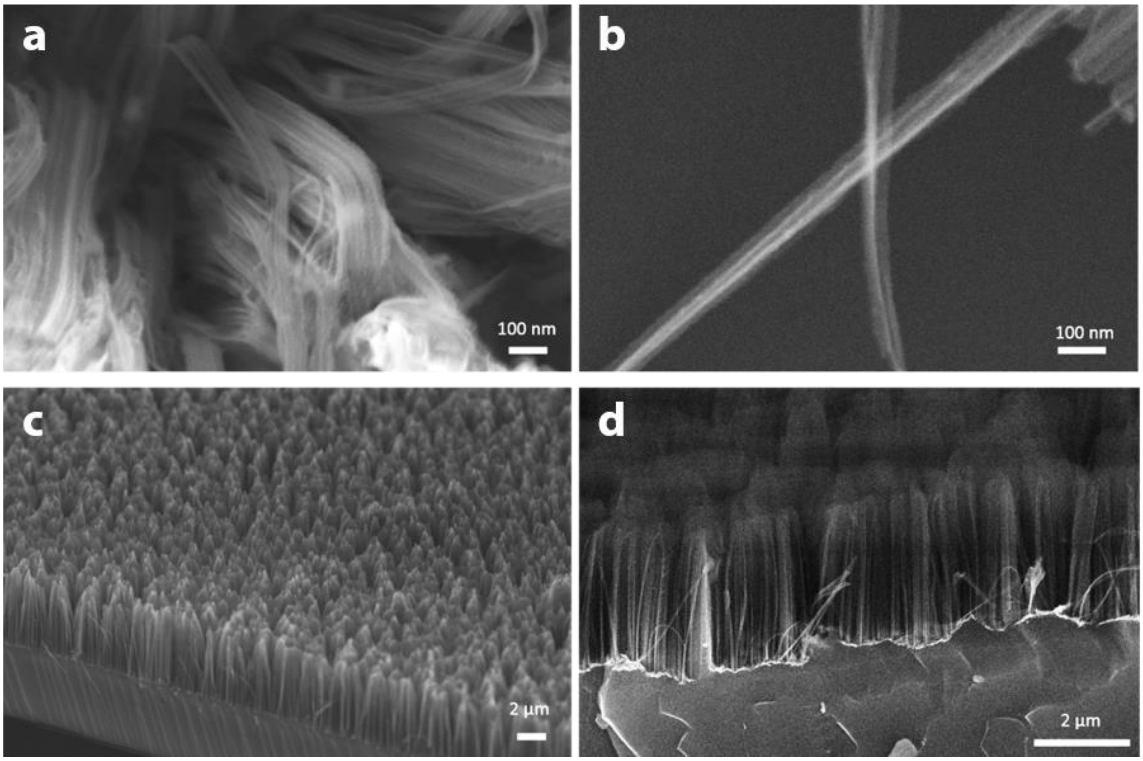

Figure 2.4 SEM images of (a) bundles of SiNWs showing their high flexibility, (b) two individual SiNWs revealing their diameter, (c) cross section of a forest of SiNWs on wafer after a brief period of etching, and (d) cross section of a SiNW forest on wafer highlighting the AuNM at the base of the forest.

2.4 Electrochemical Characterization of SiNWs

Briefly, SiNWs-on-wafer were sonicated for one hour in IPA to liberate the NWs from the wafer and subsequently centrifuged and dried. A slurry was produced with 70 wt.% SiNWs, 10% AB, and 20% PVDF in NMP. The slurry was cast onto copper foils and

dried for four hours at 105°C under vacuum to remove moisture and NMP. 2032-type coin cells were assembled in an Ar-filled glovebox with 0.09 ppm O_2 and 0.50 ppm H_2O. All cells were tested with a Li metal wafer counterelectrode with a 1M $LiPF_6$ in 1:1 v:v EC:DMC electrolyte. Figure 2.5a shows the cycling at a rate of C/10 (1C = 4 A g^{-1}), which demonstrates stable cycling over 130 cycles with excellent CE (~99.99%). After the first cycle there is minimum capacity fade, suggesting the SEI forms predominantly on the first cycle and is stable thereafter. The high CE around 99.99% each cycle is indicative of the potential for these anodes to be used in EVs, based solely on performance.

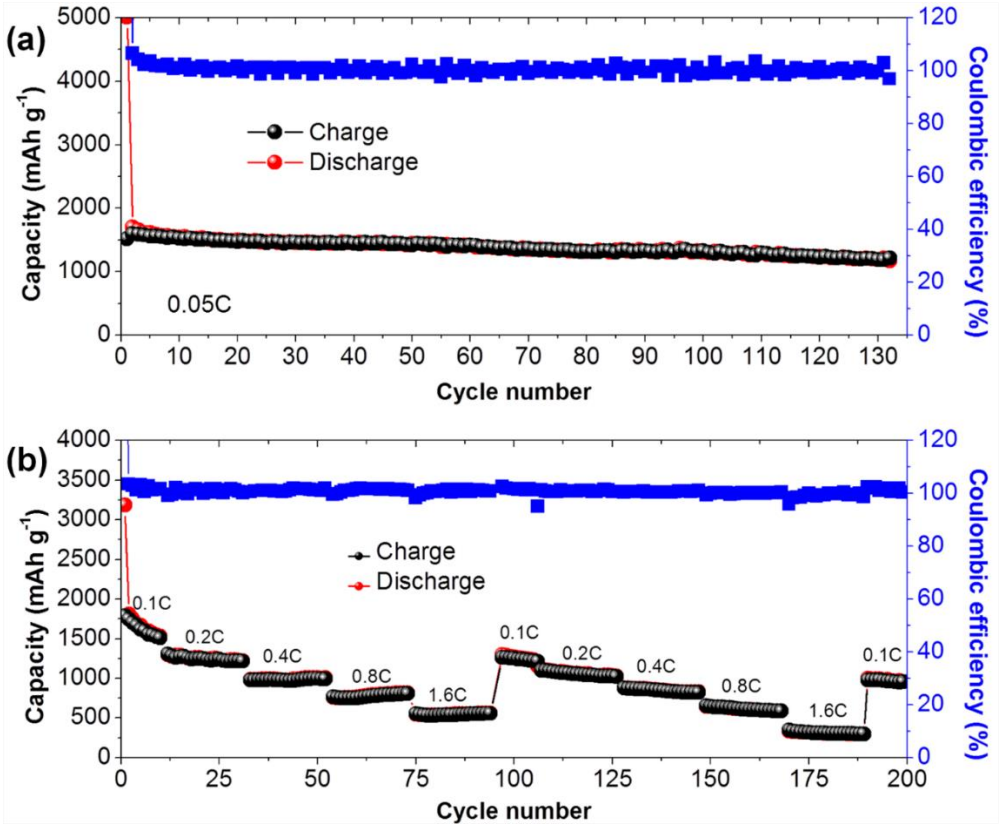

Figure 2.5. (a) Galvanostatic cycling of SiNW electrodes at a rate of C/10 (1C = 4A g^{-1}), with first cycle performed at C/40. (b) C-rate testing of SiNW electrodes at various current densities.

Figure 2.5b displays the rate capability of the SiNWs at various current densities over 200 cycles. A rate as high as 1.6C demonstrated performance greater than graphite, which equates to an actual charge-discharge time of ~7 minutes. Beyond 1.6C, the capacity produced is lower than that of graphite which is due to the low conductivity of Si compared to graphite. The addition of a conformal carbon coating would allow for better performance at higher current densities over AB, but it was not demonstrated here. The effect of conformal carbon coatings is demonstrated in subsequent chapters. The CE values are over 99.5% for almost all cycles, which is a significant improvement over SiO_2 NTs.

Figure 2.6.a shows the cyclic voltammetry (CV) curves for the first five cycles, which reveals an activation process. This activation process is not readily seen in galvanostatic cycling, because a scan rate of 0.1 mV s^{-1} does not permit complete lithiation of all SiNWs. It takes a few cycles of cycling for all SiNWs or the entire thickness of SiNWs to become electrochemically active. The increase in intensity, and hence current, of both the alloying (0.20 V and 0.01 V) and dealloying (0.33 V and 0.50 V) peaks associated with Si highlight this electrode activation. Cycles 6-10 are shown in Figure 2.6b, demonstrating activation is largely completed and the electrodes are electrochemically stable. The relatively high current achieved (~1 mA) compared to numerous published Si-based anodes demonstrates the high loading density (~2 mg cm^{-2}). Figure 2.6c shows the charge-discharge curves for SiNW anodes at select initial cycles. The voltage plateaus are in good agreement with the CV peaks. It is clear that most of the electrochemical activity happens well below 1 V despite testing up to 2 V. This low dealloying potential is crucial for full cell applications, for which an anode with a lowest possible discharge potential is

desired. Figure 2.6d shows the charge-discharge curves for the various C-rates tested in Figure 2.5b. Increasing current densities does not affect the shape of the curves or the locations of the voltage plateaus.

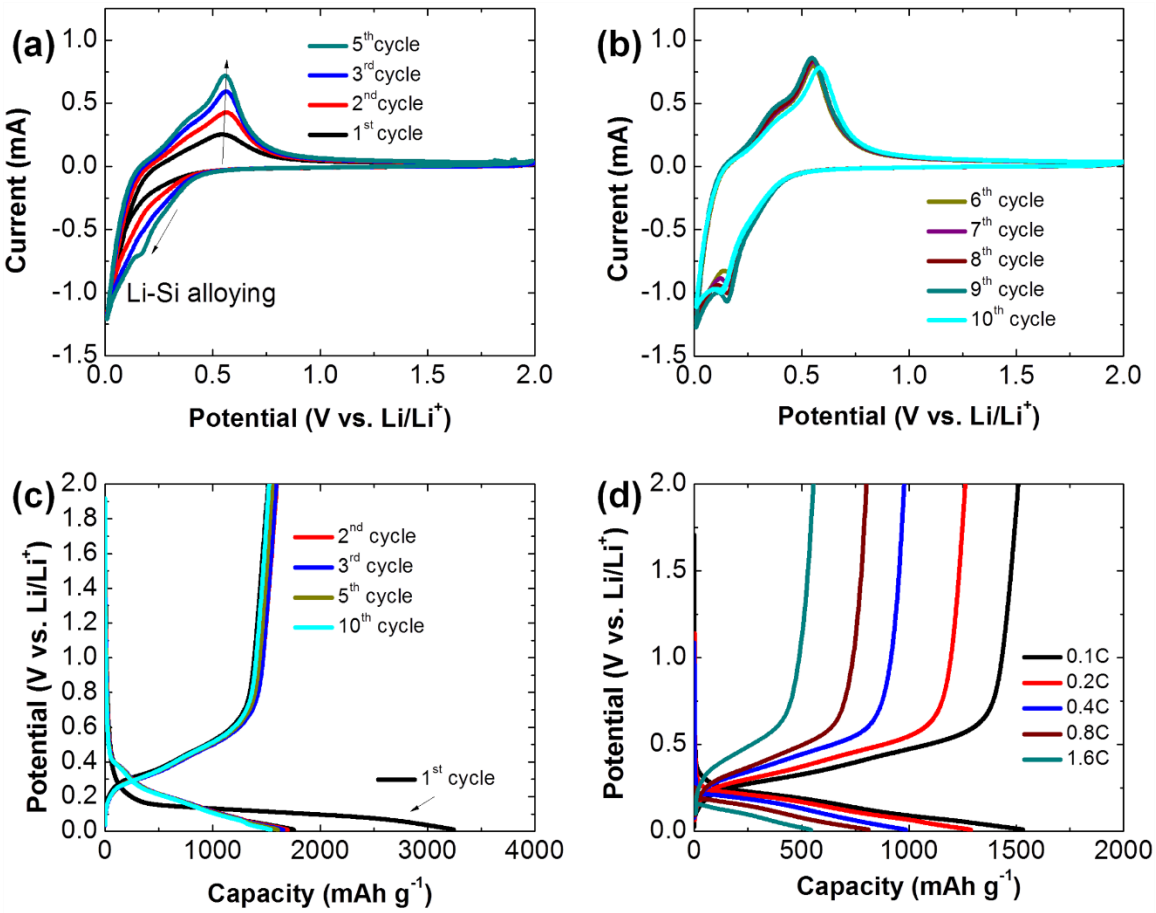

Figure 2.6 (a) CV curves for cycles 1-5 showing alloying and dealloying peaks associated with SiNW anodes. (b) CV curves for cycles 6-10. (c) Charge-discharge curves for SiNW anodes for select initial cycles. (d) Charge-discharge curves at select C-rates.

2.5 Synthesis and Characterization of SiNTs

Another exotic morphology that Si can take on at the nanoscale is silicon nanotubes (SiNTs), which has only been demonstrated by a handful of groups using different methods[9,10]. SiNTs, while inherently more challenging to synthesize, has the added advantage of internal void space to accommodate the large volume expansion associated with lithiation and a higher surface area. Much like patterning of an Au mesh for synthesizing SiNWs, SiNTs require a ring-like mesh or mask when synthesized via MACE; this has not been shown in the literature before and was attempted in this investigation.

In order to prepare the mask for the MACE etching, an *in situ* AAO template had to first be produced on Si wafers to generate a high density of nanoscale holes. This AAO template was produced in the exact same manner as the AAO template for synthesizing SiNWs. In lieu of a thin layer of evaporated Au, numerous transition metals such as Ni, Cr, Co, etc. were evaporated perpendicular to the templates. Normally a 15 nm thick layer of metal was deposited, which is thick enough to produce a continuous film and to provide sufficient material for nanoring (NR) formation. Evaporation will form a 15 nm layer that mimics the AAO pattern on the surface of the AAO while also depositing metal at the base of the pores on the Si substrate. This small amount of metal deposited in the pores is the useful material for producing the NRs while the surface deposited metal on top of the AAO will be blasted away. The synthesis process for NRs can be visualized in Figure 2.7.

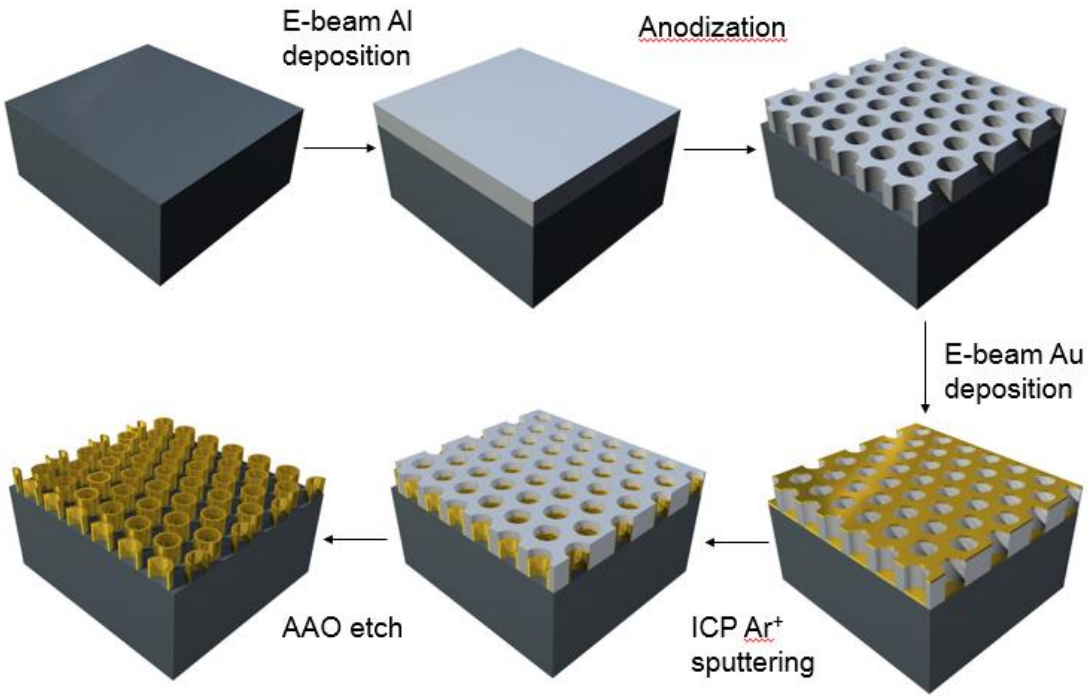

Figure 2.7 Schematic representation of the NR fabrication process including *in situ* AAO synthesis and subsequent ASR.

Inductively coupled plasma reactive ion etching (ICP-RIE) was used to create the metallic NR formation using argon plasma. Briefly, ICP-RIE is a form of dry etching that uses a high-energy reactive plasma generated under vacuum to attack the surface of wafers. Due to argon's inertness as a noble gas, the method of material removal from the wafer surface is not chemical but rather mechanical removal (sputter) through transfer of kinetic energy. Additionally, the ions travel in a vertical fashion, which allows for highly anisotropic etching. This vertical ion travel is ideal for reaching the deposited metal at the bottom of the AAO pores. The Ar ions sputter the surface-deposited metal off the top of

the AAO, but more importantly is the phenomena occurring inside the pores of the AAO template.

Ar ions bombard the metal deposited at the base of the pores and blast it away to the walls of the pore.[11] One would expect the metal to be completely blasted out of the pore due to the vertical nature of the pores, but there exists a shadow effect that effectively blocks Ar ions from removing redeposited metal along the pore walls. Thus, a ring (in the case of small heights) or a nanotube (for relatively larger heights) are formed within a few minutes of this process known as argon sputter redeposition (ASR). SEM images in Figure 2.8 show various morphologies of various metallic NRs that were formed via ASR. Figure 2.8a shows relatively short NRs composed of Ni, with inner pores that have been etched into the underlying Si substrate. The difference in contrast of the NRs and underling substrate informs us that these are indeed two different materials. In this case a longer ICP-RIE run etched into the underlying Si substrate, which may have deposited Si on the inside of the NRs. The slight color variation from the inner wall to outer wall suggests this may be the case.

Figure 2.8b shows chromium NRs of thinner wall thickness and larger heights. A single NR has been removed in the top left of the image showing the shadowing effect the ring causes in the underlying Si substrate. Again, given that the Si wafer has been partially bombarded, it is wise to assume that Si may be deposited on the inside of the CrNRs. Figure 2.8c shows the ability to fabricate theses NRs on a large (wafer) scale; here, showing a window of a few hundred microns. The dark streaks across the image are intentional tweezer scrapes to liberate the NRs from the surface and to reveal the Si substrate

morphology. While wafer-scale was not proven in the lab, there is little hindrance to scaling this process up to the wafer scale since this process relies on mostly traditional lithography techniques. This makes the process ideal for on-chip LIB fabrication. Figure 2.8d shows even taller NR formations of Ni that are in a much more disordered pattern.

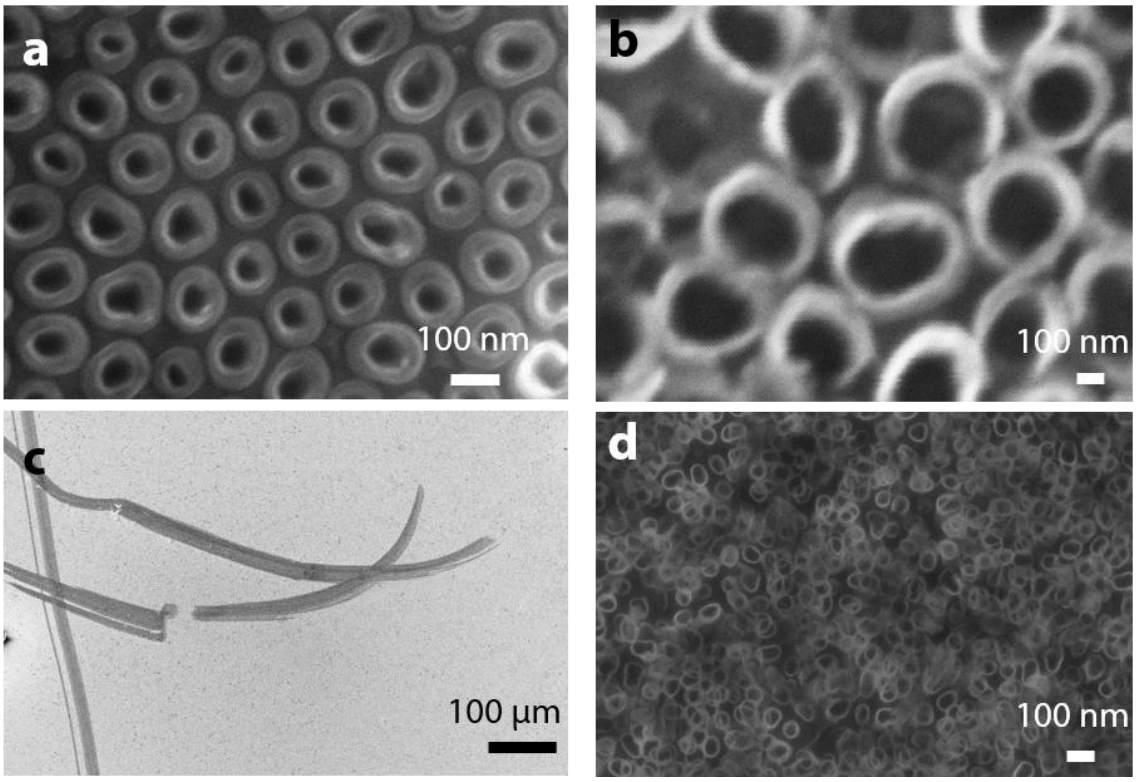

Figure 2.8 SEM images of (a) NiNRs, (b) CrNRs, (c) large are CrNRs with tweezer scratches used to reveal substrate, and (d) NiNRs with relatively large aspect ratios.

Once a metallic NR formation was achieved, an additional 5 nm of Au was e-beam evaporated onto the NR-coated surface. The NRs behave as etch blocking sites, thus shadowing any etching the Au performs on the Si wafer. This ring mask, in a 1D sense, allows for the creation of 2D nanotubes if MACE proceeds properly. The Au layer etches

the inside of the NR and along the outside of the NRs vertically into the wafer. Unfortunately, after numerous attempts, no evidence of SiNTs was observed via SEM. There may be numerous reasons as to why the etching does not proceed as it does in theory: 1. The rings may be too close together to allow for the creation of a Au mesh that can etch down into the wafer. 2. The AuNPs evaporated into the inside of the rings may not etch as quickly as the Au mesh, thus the inside of the SiNTs was never formed. 3. Lastly, and most probable, during MACE the Au film may oxidize the underlying NR mask and destroy any etch blocking capability that existed in the first place. This third scenario seems most probable in the light of no evidence of nanowire or nanotube morphology. Additionally, the Au film simply delaminated from the NR decorated wafer upon submersion in the etchant suggesting that the NRs may have prevented effective adhesion of the Au layer to the wafer surface.

2. 6 Conclusions

SiNWs synthesized via MACE of highly doped crystalline silicon wafers produce a reversible capacity of ~1500 mAh g^{-1} after 130 cycles and outperform graphite even at a rate of 1.6C. Unfortunately, this excellent electrochemical performance is hindered by the lack of scalability in synthesizing SiNWs. Only a few tens of milligrams could be produced across four inch wafers, which is not significant given the high cost of the wafers and extensive fabrication process. This technology would be much better suited for on-chip applications that only require minute amounts of active material in contrast to EVs, which require several kilograms of material per LIB bank. The added cost of noble metal etching

assistants such as Ag and Au also hinder large scale production of this material. Notably, the synthesis of SiNWs is carried out at room temperature without high temperature CVD or reduction environments needed. MACE is performed electrolessly which highlights the facileness of this step.

SiNTs face the same hinderances to industrial application as SiNWs based on the even more complex synthesis process and inability to effectively demonstrate SiNT synthesis herein. Had SiNT synthesis been successful, the scalability of the process still makes the structure unfeasible on an industrial scale in terms of a source of LIB active material powder. Besides the relatively high cost of the crystalline wafers, numerous lithography steps must be taken in addition to the utilization of Au as the etching assistant. However, ASR could be used in other fields of nanotechnology including plasmonics and on-chip energy storage.

2.7 References

1 Chan, C. K. *et al.* High-performance lithium battery anodes using silicon nanowires. *Nat. Nanotechnol.* **3**, 31-35 (2007).

2 To, W.-K., Tsang, C.-H., Li, H.-H. & Huang, Z. Fabrication of n-type mesoporous silicon nanowires by one-step etching. *Nano Lett.* **11**, 5252-5258 (2011).

3 Zamfir, M. R., Nguyen, H. T., Moyen, E., Lee, Y. H. & Pribat, D. Silicon nanowires for Li-based battery anodes: a review. *J. Mater. Chem. A* **1**, 9566-9586 (2013).

4 Huang, Z., Geyer, N., Werner, P., de Boor, J. & Gosele, U. Metal-Assisted Chemical Etching of Silicon: A Review. *Adv. Mater.* **23**, 285-308 (2011).

5 Ge, M., Rong, J., Fang, X. & Zhou, C. Porous Doped Silicon Nanowires for Lithium Ion Battery Anode with Long Cycle Life. *Nano Letters* **12**, 2318-2323 (2012).

6 Egan, E. & Tobias, C. Measurement of Interfacial Re-equilibration during Hydrogen Bubble Coalescence. *J. Electrochem. Soc.* **141**, 1118-1126 (1994).

7 Liu, X. H. *et al.* Size-Dependent Fracture of Silicon Nanoparticles During Lithiation. *ACS Nano* **6**, 1522-1531 (2012).

8 Dawood, M. *et al.* Modulation of surface wettability of superhydrophobic substrates using Si nanowire arrays and capillary-force-induced nanocohesion. *Soft Matter* **8**, 3549-3557 (2012).

9 Song, T. *et al.* Arrays of Sealed Silicon Nanotubes As Anodes for Lithium Ion Batteries. *Nano Lett.* **10**, 1710-1716 (2010).

10 Yoo, J.-K., Kim, J., Jung, Y. S. & Kang, K. Scalable Fabrication of Silicon Nanotubes and their Application to Energy Storage. *Adv. Mater.* **24**, 5452-5456 (2012).

11 Hobbs, K. L., Larson, P. R., Lian, G. D., Keay, J. C. & Johnson, M. B. Fabrication of nanoring arrays by sputter redeposition using porous alumina templates. *Nano Lett.* **4**, 167-171 (2004).

Chapter 3: SiO_2 NTs via CVD of PDMS on AAO

3.1 Introduction

While silicon has the highest known theoretical specific capacity of all Li-ion battery materials, its oxide forms may also serve as feasible anode materials due to their high specific capacity relative to graphite, non-toxicity, highest abundance in the earth's crust, and excellent chemical inertness.[1] As the most abundant compound in the earth's crust as a rock forming compound, silicon oxides are very low cost materials. Chang *et al.* were the first to propose quartz as a viable, electrochemically active anode material for LIBs with excellent cycling stability over 250 cycles while delivering a capacity of over two times that of graphite.[2] Yan *et al.* summarized the Li-ion storage capabilities of SiO_2 in the following Table 3.1:

	Reaction equations	**The molar ratio of SiO_2 and Li**	**Theoretical initial capacity of SiO_2**	**Theoretical reversible capacity of SiO_2**
Mechanism 1	$5SiO_2+4Li^+ + 4e \leftrightarrow 2Li_2Si_2O_5 + Si$	5:4	749 mAh g^{-1}	749 mAh g^{-1}
	$5Si + 22Li^+ + 22e \leftrightarrow Li_{22}Si_5$			
Mechanism 2	$2SiO_2 + 4Li^+ + 4e \rightarrow Li_4SiO_4 + Si$	1:2	1872 mAh g^{-1}	980 mAh g^{-1}
	$5Si + 22Li^+ + 22e \leftrightarrow Li_{22}Si_5$			
Mechanism 3	$SiO_2 + 4Li^+ + 4e \rightarrow 2Li_2O + Si$	1:4	3744 mAh g^{-1}	1961 mAh g^{-1}
	$5Si + 22Li^+ + 22e \leftrightarrow Li_{22}Si_5$			

Table 3.1 Theoretical capacities of SiO_2 based on various mechanisms (adapted from Yan *et al.*)[3]

In contrast to silicon, SiO_2 has several differing theories on how lithiation occurs in the initial charge cycle due to the presence of oxygen. Ideally, we desire the oxygen to be consumed entirely to form Li_2O. This produces the highest theoretical irreversible capacity of 3744 mAh g^{-1}; this is comparable to silicon's theoretical reversible capacity of 3579 mAh g^{-1}. The corresponding theoretical reversible capacity is 1961 mAh g^{-1}. If compounds such as lithium disilicate ($Li_2Si_2O_5$) and lithium orthsilicate ($LiSiO_4$) are formed during the initial lithiation, then the capacity is significantly reduced to as low as 749 mAh g^{-1}. In reality, the initial lithiation will produce all three compounds (Li_2O, $Li_2Si_2O_5$, $LiSiO_4$) as evidenced by work done by Song *et al*., which places the theoretical capacity somewhere in the middle of all three theories.[4]

SiO_2 anodes suffer from a few key drawbacks that may make real-world applications unfeasible. The evolution of Li_2O, $Li_2Si_2O_5$, and $LiSiO_4$ during initial charging produces a large irreversible capacity that significantly lowers the reversible capacity far below the theoretical value. Kim *et al.* confirmed the existence of Li_2O and $LiSiO_4$ and Miyachi *et al.* confirmed the existence of the $Li_2Si_2O_5$ phase.[5,6] In the same manner that SiO_2 can be reduced thermically via the aforementioned methods, it can also be electrochemically reduced by Li during cycling in a LIB; this is the primary operating mechanism during the first charge.[7] The reversible capacity is much lower than that of silicon due to the presence of ~53.3 wt.% oxygen in SiO_2. Oxygen is a completely inactive material after the initial charge and accounts for over half the weight of the SiO_2. However, the compounds produced from this oxygen result in an inactive matrix that serves to buffer

the expansion of silicon and may provide a mechanically stable framework, which is the reason SiO_2-based anodes have relatively low capacity fade rates compared to silicon.

SiO_2 is a wide bandgap insulator and, hence, has very poor electronic conductivity (~10^{11} times lower than silicon).[8] In a LIB setting we desire the electronic conductivity to be as high as possible such that electrons experience minimal resistance in traveling through the electrodes. Additives such as carbon black and carbon coatings assist in increasing conductivity but they do not change electron transport through SiO_2.[7,9] As a result, very low current densities have to be used when cycling SiO_2 based anodes in comparison to conventional graphite anodes.

Non-stoichiometric silicon oxides (SiO_x, $0<x<2$) have also been considered as viable anode materials with the added benefit of a lower oxygen content.[10] Silicon sub-oxides are essentially a hybrid of silicon and silica which carries the benefit of having a higher capacity than SiO_2 while still mainting the good cycle stability of SiO_2 anodes. SiO_2 and SiO_x anodes have only recently garnered significant attention and have taken forms such as thin films, tree-like structures, nanoparticles, and nanocubes.[3,9,11,12]

Herein, an exotic silica nanoscale morphology, silicon dioxide nanotubes (SiO_2 NTs), has been successfully demonstrated and thoroughly characterized as an anode material for LIBs. High aspect SiO_2 NTs with a diameter of 200 nm and a length of 50 μm were synthesized via commercial AAO templates and a benign, low cost SiO_2 precursor: polydimethylsiloxane (PDMS). PDMS is an optically transparent, non-toxic, and environmentally benign organosilicon widely used in pharmaceutical and consumer applications.[13,14] PDMS produces SiO_2 vapor species when heated in ambient atmosphere,

which makes it an ideal precursor for template (AAO) deposition of SiO_2 at the nanoscale. Beginning at 290°C, PDMS will thermally degrade into volatile cyclic oligomers via chain-folded scission of Si-O bonds by oxygen-catalyzed depolymerization.[15,16] The ability for PDMS to produce SiO_2 vapor allows for deposition of SiO_2 on a variety of templates. Specifically, hollow nanostructures are of interest for Li-ion batteries due to reduced Li-ion diffusion path distance via increased surface area and small wall thicknesses.[17,18] Alleviation of lithiation-induced mechanical stresses can also be accomplished through engineering interior voids in the active material.[19,20] Herein, I present a modified procedure for fabricating high aspect ratio SiO_2 NTs, previously presented by Hu *et al.*, and evaluate their performance as Li-ion battery anodes[21].

3.2 Synthesis of SiO_2 NTs

The fabrication process for SiO_2 NTs is illustrated schematically in Figure 3.1. An amorphous layer of SiO_2 is deposited onto commercial AAO templates via vapor phase deposition through thermal degradation of PDMS in air under vacuum. This improved synthesis procedure eliminates the need to sand excess SiO_2 deposits off of the fragile AAO templates after deposition. By placing the AAO templates downstream from, rather than covering, the PDMS blocks and performing the deposition process under vacuum, we are better able to control SiO_2 deposition throughout the AAO template, preventing unwanted thick deposits of SiO_2. The deposition of SiO_2 is not a self-limiting process and can therefore continually deposit SiO_2 until vaporization stops. SiO_2 conformally coats all exposed surfaces of the AAO including the top and bottom of the template, creating a

connected tubular network of SiO_2. The AAO is subsequently removed via a 2M phosphoric acid bath at 70ºC for 48 hours to leave SiO_2 NT bundles. After rinsing several times in DI water to remove phosphoric acid, the tubes are ultrasonicated for 1 hour to separate the bundles of SiO_2 NTs into individual tubes. The connected SiO_2 NT network obtained after AAO removal is not mechanically sound, therefore the tubes must be sonicated apart so that they may be handled facilely in powder form.

Drying of SiO_2 NTs on a flat substrate can produce a paper-like material after drying which can be handled facilely. However, the tubes are only 50 μm long and cannot entangle themselves enough to form a mechanically flexible paper-like material. Growing much longer NTs would allow for a realization of a binderless paper-like electrode, although AAO templates are not produced at thicknesses high enough to support this claim. Different high aspect ratio templates can be used in lieu of AAO to achieve a higher aspect NT. A 20 nm coating of SiO_2 on a 13 mm diameter AAO with a thickness of 50 μm produces a volumetric density of SiO_2 of 0.515 g cm^{-3} and an areal density of 2.57 mg cm^{-2}. By the numbers, this is a scalable process for producing the exotic NT morphology, but the single biggest limiting factor is the cost of producing the AAO templates.

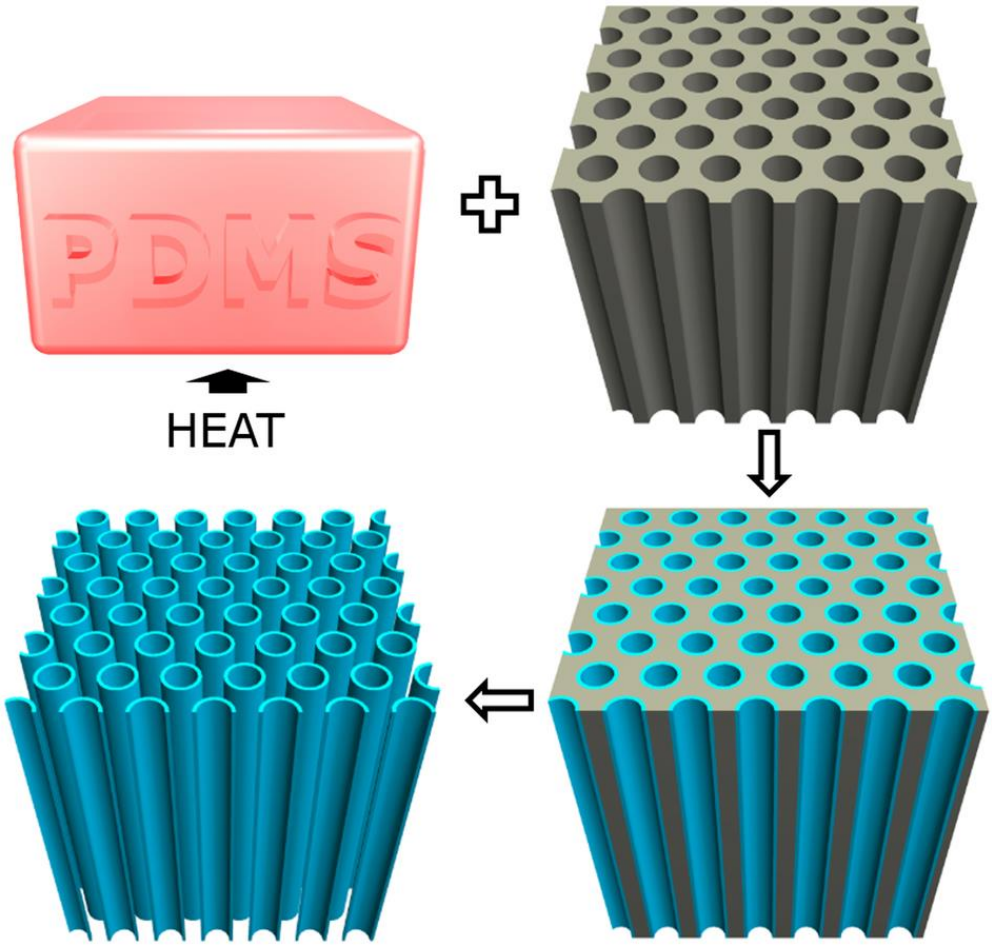

Figure 3.1 Schematic representation of the fabrication process for SiO_2 NTs.

3.3 Characterization of SiO_2 NTs

SEM images in Figure 3.2 reveal the tubular morphology of the SiO_2 NTs as well as their high aspect ratio. Bundles of SiO_2 NTs occur due to deposition of SiO_2 on the tops and bottoms of the AAO templates, but brief sonication serves to easily liberate the tubes. The SEM image in Figure 3.2a reveals the excellent uniformity of the SiO_2 coating across all dimensions of the AAO templates and the interconnected nature of the SiO_2 NTs after removal of the AAO template. These small bundles occur after a brief period of sonication

and further sonication serves to fully separate all of the tubes, as seen in Figure 3.2b. The tubes have a very high aspect ratio of 250:1 at a length of 50 μm and an average diameter of 200 nm. Lengthy periods of sonication fully separate and shorten the SiO_2 NTs, revealing their tubular morphology as seen in Figure 3.2c. The SEM image in Figure 3.2d reveals the branched morphology of the SiO_2 NTs, which serves to further increase the surface area of the tubes and is purely a result of anodization in the presence of aluminum imperfections.[22]

TEM images reveal the wall thickness is 20 nm and highly uniform throughout the length of the tubes as in Figure 3.2e. The branched nature of the NTs is confirmed via TEM and no evidence suggests porosity exists in the walls. TEM confirms the SiO_2 NTs have an average diameter of 200 nm, which is expected given the commercial AAO template specifications. Based on the highly random fracture patterns generated via sonication, we conclude that the tubes are composed of amorphous SiO_2. XRD analysis confirms that the SiO_2 NTs are amorphous as seen in Figure 3.2f. Regardless of initial crystallinity, SiO_2 NTs will undoubtedly be amorphous in subsequent cycles due to repeated lithiation of Si species.[23,24]

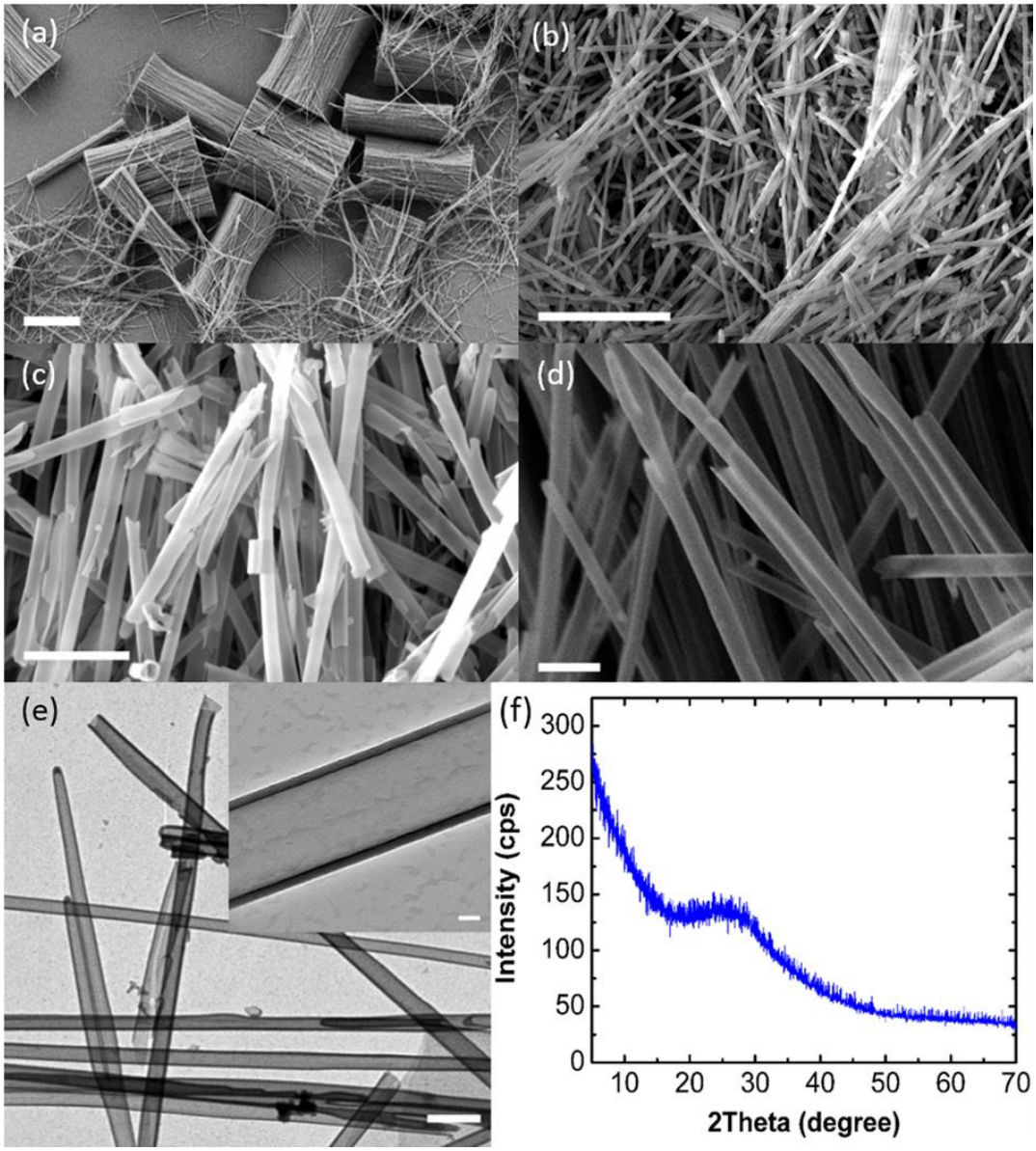

Figure 3.2 SEM image of (a) partially separated SiO_2 NTs showing NT bundles and dispersed NTs, (b) fully separated dispersed SiO_2 NTs, (c) separated SiO_2 NTs showing tubular morphology, and (d) image showing branched morphology. Scale bars are 25 μm, 10 μm, 2 μm, and 1 μm for (a), (b), (c), and (d), respectively. (e) TEM image of dispersed SiO_2 NTs and inset showing tube diameter and wall thickness. Scale bar is 400 nm and 50 nm for the inset. (f) XRD analysis of SiO_2 NTs.

Scanning transmission electron microscopy (STEM) and energy dispersive x-ray spectroscopy (EDS) were further performed to confirm the composition of the as-prepared nanotube samples. The STEM-EDS sample was simply prepared via transferring vacuum-dried SiO_2 NTs onto a copper TEM grid. As shown in Figure 3.3a, SiO_2 NTs are randomly oriented, and a selected area EDS mapping was performed on the region within the yellow box. EDS microanalysis on the selected region shows the SiO_2 NTs consists of primarily Si and O (Figure 3.3b). EDS element mapping micrographs of Si and O suggest a very uniform distribution of these two elements. Traceable amount of C, Al, P (wt% < 1%) were observed due to carbon contaminates, unetched AAO, and unremoved H_3PO_4 etchant, respectively. An EDS quantitative analysis on the selected region was performed to characterize the weight and atomic percentages of elements and to confirm the existence of SiO_2, as in Figures 3.3e and 3.3f. We believe the contaminants and the copper grid both contribute to the oxygen peak due to the existence of respective oxides from each.

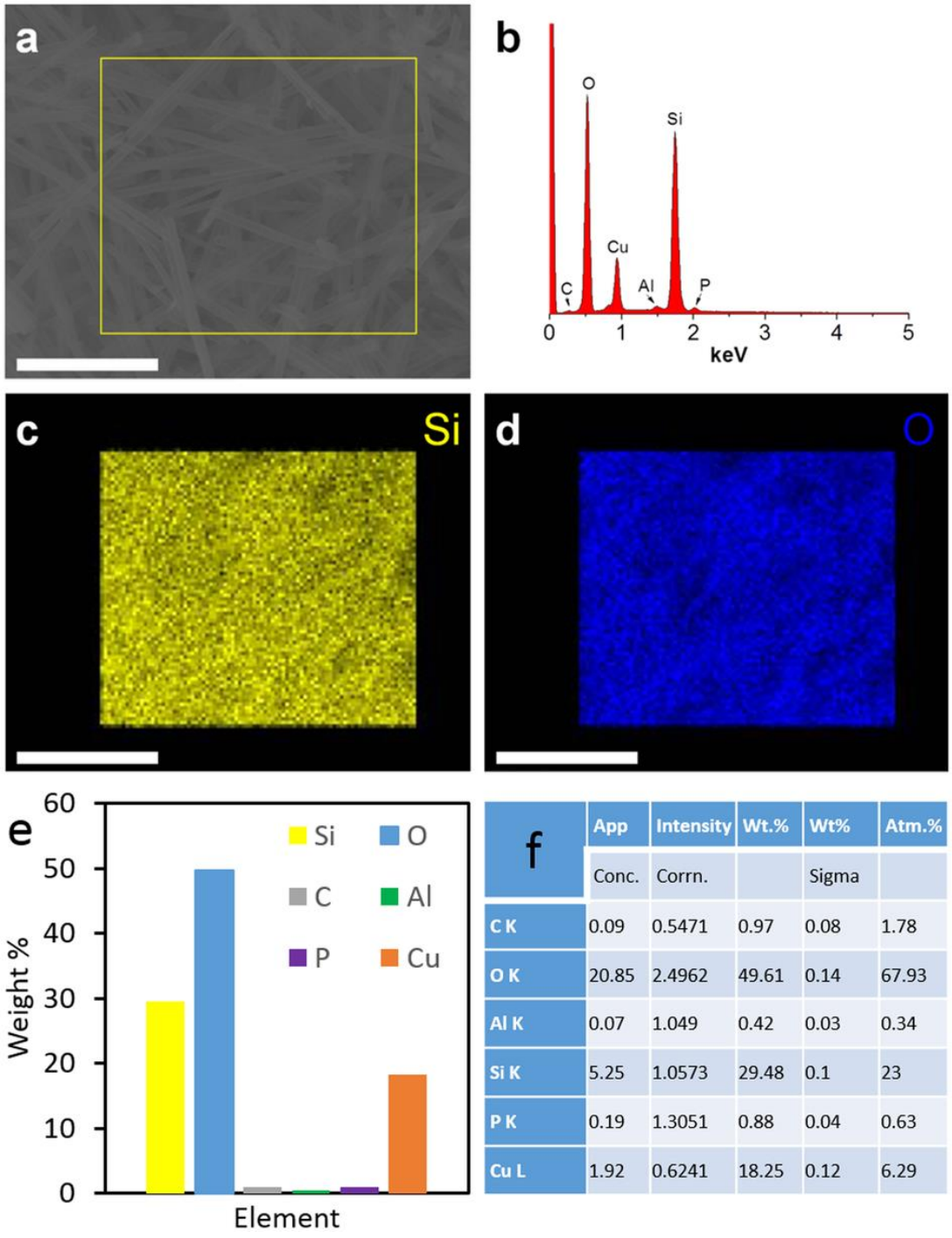

f

	App	Intensity	Wt.%	Wt%	Atm.%
	Conc.	Corrn.		Sigma	
C K	0.09	0.5471	0.97	0.08	1.78
O K	20.85	2.4962	49.61	0.14	67.93
Al K	0.07	1.049	0.42	0.03	0.34
Si K	5.25	1.0573	29.48	0.1	23
P K	0.19	1.3051	0.88	0.04	0.63
Cu L	1.92	0.6241	18.25	0.12	6.29

Figure 3.3 (a) SEM image of SiO_2 NTs. (b) EDS spectra of SiO_2 NTs on selected region (yellow rectangle) of image a. (c–d) show the EDS microanalysis of element Si and O for this selected region. Scale bar: 5 μm. (e–f) EDS quantitative analysis of selected region.

While a 20 nm coating of SiO_2 produces free standing SiO_2 NTs, an investigation into thinner SiO_2 coatings was performed to see if the tubes still retained their mechanical stability. One obvious drawback of a thinner silica coating is production of less material volumetrically, but more significant may be the lack of ability to retain a mechanically stable NT structure. To test this, the PDMS rubber amount was cut in half while all other CVD conditions were held constant. Not surprisingly, the thickness of the SiO_2 NT walls dropped to ~5 nm as indicated in the atomic force microscopy (AFM) measurements in Figure 3.4 below. Briefly, SiO_2 NTs were suspended in IPA and sonicated to thoroughly disperse them in solution. A drop of solution was cast onto a Si wafer chip and dried in air. The 5 nm thick walls of the NTs are not enough to effectively support the NT, and thus the tubes collapse via capillary force when dried on the wafer; this was not seen with thicker NTs. Height profiles were taken across a complete NT and a fractured NT to effectively characterize the thickness of a single and double wall. The fractured tube exhibits a single wall thickness of 5 nm and a double wall thickness of 10 nm; the complete NT sample confirms this measurement of a 10 nm double wall thickness. Sonication alone is enough to significantly shorten the length of the NTs as well as "unzip" many of the tubes into SiO_2 nanoribbons. The large population of dispersed NTs in Figure 3.4c demonstrates the uniformity of the silica coating.

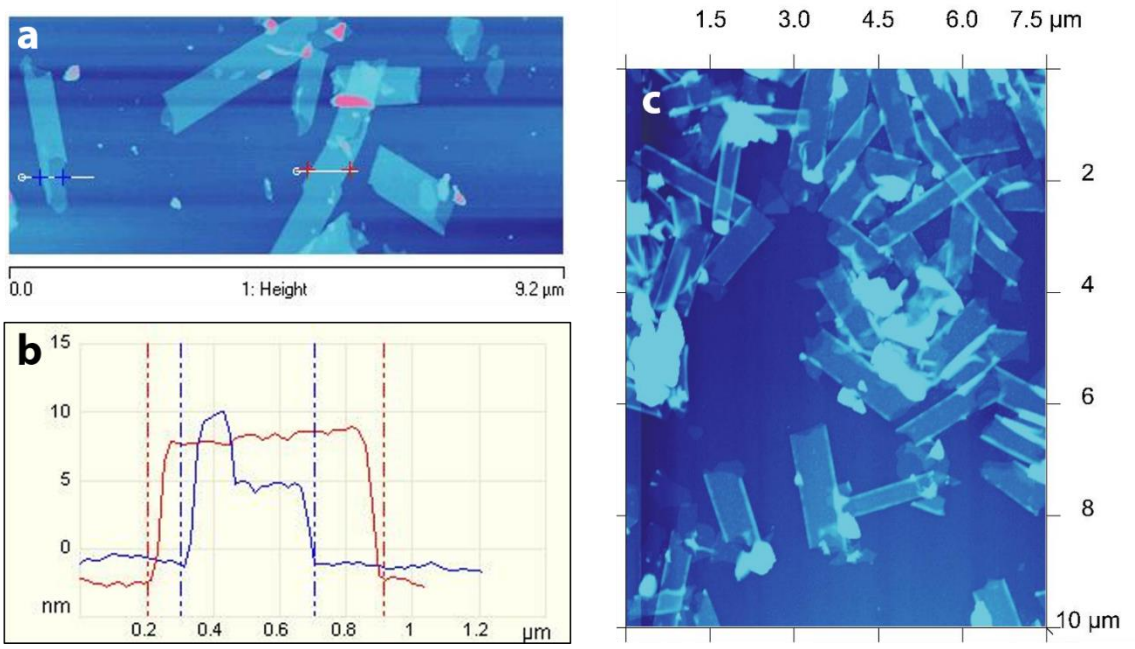

Figure 3.4 (a) AFM height profile of a few dispersed SiO_2 NTs with cross sections labeled in blue and red. (b) Height data for cross sections denoted in (a). (c) Large area AFM height profile of dispersed SiO_2 NTs.

The Langmuir and BET surface areas were measured to be 45.17 and 26.64 $m^2 g^{-1}$, respectively, for the as-prepared SiO_2NTs. The obtained surface area and pore distribution suggest the as-prepared SiO_2 NTs have limited surface area and porosity as in Figure 3.5. This surface area is more than double the surface area of as-received AAO templates which is expected given the tubular morphology.[25] This limited surface area is beneficial in reducing the amount of SEI layer formation in the first few cycles by limiting active material contact with the electrolyte.[26] However, the rate capability suffers as a result of the limited surface area due to a higher reliance on bulk diffusion of Li into SiO_2.

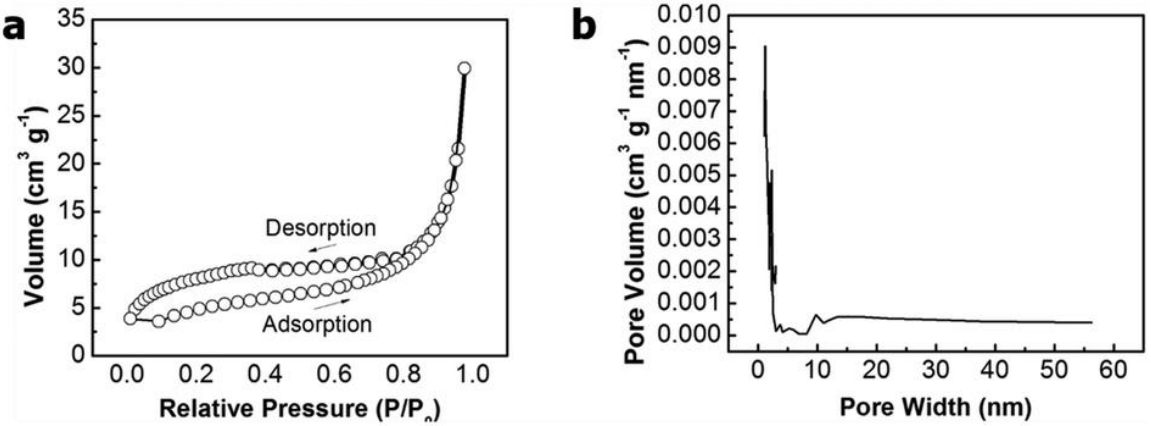

Figure 3.5 (a) Type IV N_2 adsorption and desorption isotherms for SiO_2 NTs. (b) Pore size distribution of SiO_2 NTs.

3.4 Electrochemical Characterization of SiO_2 NTs

The electrochemical performance of SiO_2 NTs was characterized by fabricating 2032 coin cells with SiO_2 anodes and Li metal counter electrodes. CV was performed in the 0.01–3.0 V range with a scan rate of 0.1 mV s^{-1}, shown in Figure 3.6a. The CV plot is shown to 1.75 V to emphasize the noteworthy reactions taking place at lower voltages, although SiO_2 is electrochemically active with SiO_2 in a wide voltage window. Decomposition of the electrolyte and formation of the SEI layer occurs at the broad peak of 0.43 V as in Figure. 3.6a. A much broader, less discernable peak occurs at 1.40 V which can be attributed to a reaction between electrolyte and electrode and the beginning of SEI formation.[27] Both of these peaks become undiscernible in the 2nd cycle suggesting SEI formation takes place mostly during the first cycle and that these initial reactions are irreversible. During the initial charge cycle a noticeable peak occurs at 0.33 V, which can be attributed to dealloying. In subsequent cycles this peak becomes very pronounced and

shifts downward to 0.25 V. The sharpening and growth of this dealloying peak implies a rate enhancement in the kinetic process of delithiation of SiO_2 NTs. The kinetic enhancement may be due to the formation of an embedded nano-Si phase as it has been reported that one of the oxidation peaks of Si is 0.25 V during Li extraction from Li_xSi.[28] By the 10th cycle there is an emergence of an anodic peak located at 0.22 V while the peak at 0.01 V has decreased. It is known in the literature that the 0.01 V and 0.22 V peaks are associated with the lithiation of Si.[27,29] The CV curves are in good agreement with the charge-discharge profiles in Figure 3.6c and 3.6d.

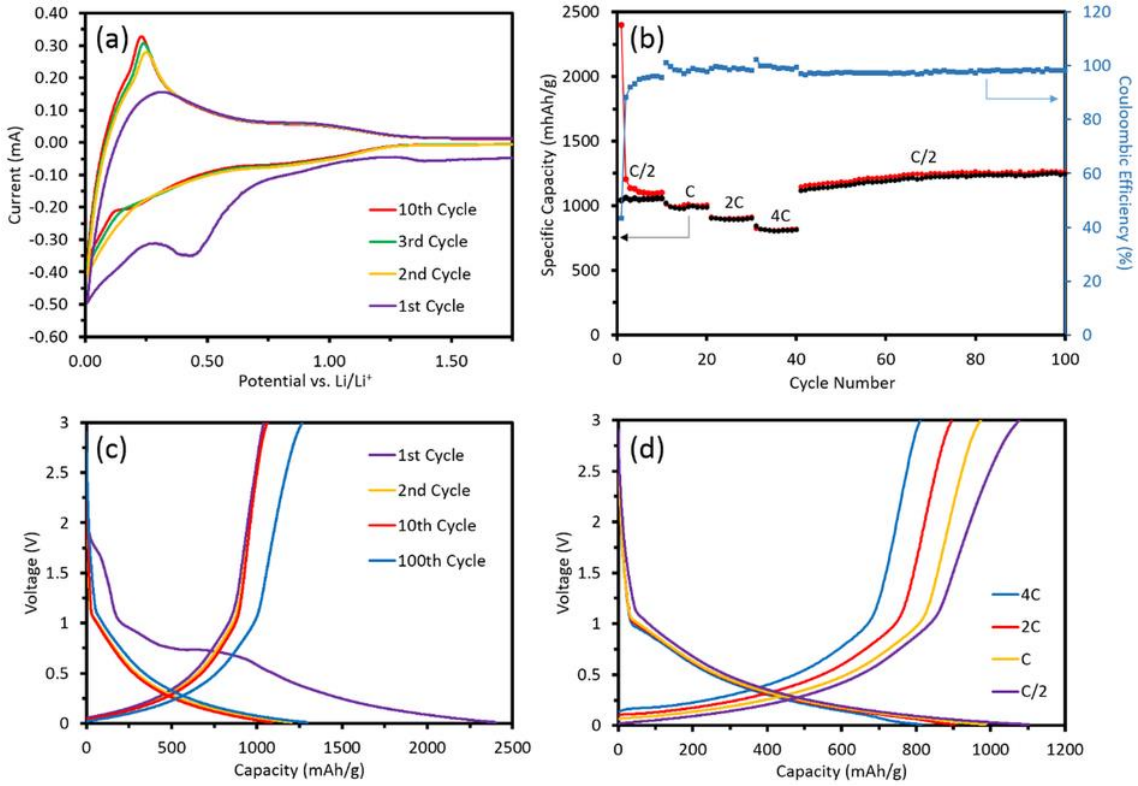

Figure 3.6 (a) CV of SiO_2 NTs using a scan rate of 0.1 mV s^{-1}. (b) Charge-discharge capacities versus cycle number using a C rate of 100 mA g^{-1}. (c) Galvanostatic voltage profiles for SiO_2 NTs at a C/2 rate at selected cycles. (d) Galvanostatic voltage profiles for SiO_2 NTs at selected C rates.

Galvanostatic cycling of SiO_2 NTs using a C rate of 100 mA g^{-1} was performed for 100 cycles at selected current densities. The initial sharp decrease in charge capacity over the first few cycles, seen in Figure 3.6b, can be attributed to the formation of the SEI layer. The very thin walls of the SiO_2 NTs allows for lithiation of a larger percentage of active material and thus the marked high capacity relative to other published SiO_2 anodes utilizing thicker structures.[10,30] The initial charge capacity is 2404 mAh g^{-1} using a rate of C/2, and the initial discharge capacity is 1040 mAh g^{-1} yielding a 1st cycle efficiency of 43.3%; this is attributed to the SEI formation. After 10 cycles the charge capacity levels off to 1101 mAh g^{-1} and the discharge capacity increases to 1055 mAhg^{-1}; this yields an efficiency of 95.8%. Expectedly, cycling at higher rates produces lower charge capacities as follows: 1008 mAh g^{-1} at 1C, 914 mAh g^{-1} at 2C, and 814 mAh g^{-1} at 4C. After 100 cycles the charge and discharge capacity increase to 1266 mAh g^{-1} and 1247 mAh g^{-1}, respectively; the efficiency is 98.5%.

After the initial decrease in capacity due to SEI formation, the capacity steadily increases until stabilizing at around 80 cycles. We believe this capacity increase is due to the increasing amount of silicon as the SiO_2 is partially reduced by Li and not fully reduced back to SiO_2. Ban *et al.* proposed capacity in SiO_2 anodes increases over time due to growth of the Si phase and, thus, a growth in Si volume. The formation of Li_ySiO_x at Si/SiO_x boundaries leads to the formation of three-fold coordinated Si [Si(III)] which reflects through SiO_4 tetrahedra to bond to the silicon phase. The capacity gained by inclusion of new Si atoms (~4 Li per Si) in the Si phase outweighs the loss in capacity due to the consumption of SiO_2 in the irreversible formation of Li_ySiO_x.[31] We do not attribute

this increase in capacity to increases in operating environment temperatures as several cells were tested in a staggered sequence with the same phenomenon observed in all cells. CV also supports this claim via the significant heightening and narrowing of the dealloying peak, suggesting more Li^+ is able to be dealloyed from the SiO_2 NTs in subsequent cycles. The emergence of an cathodic peak at 0.22 V in the CV plot by the 10^{th} cycle is consistent with the lithiation of Si.

Coin cells were disassembled after 100 galvanostatic charge-discharge cycles in an Ar-filled glovebox. Electrodes were fully charged to remove reversibly alloyed lithium from the tubes. SiO_2 NT electrodes were rinsed with acetonitrile to remove electrolyte and then etched in 0.1 M HCl to remove the SEI layer and reveal post-cycling tube morphology. The SiO_2 NTs have undergone slight changes in morphology as evidenced in the TEM image in Figure 3.7. Cycled SiO_2 NTs still retain their tubular morphology but have developed slight undulations in the walls with variations in wall thickness. This preservation of the SiO_2 tube morphology post-cycling has also been confirmed by Wu *et al.* even after 2000 cycles.[32]

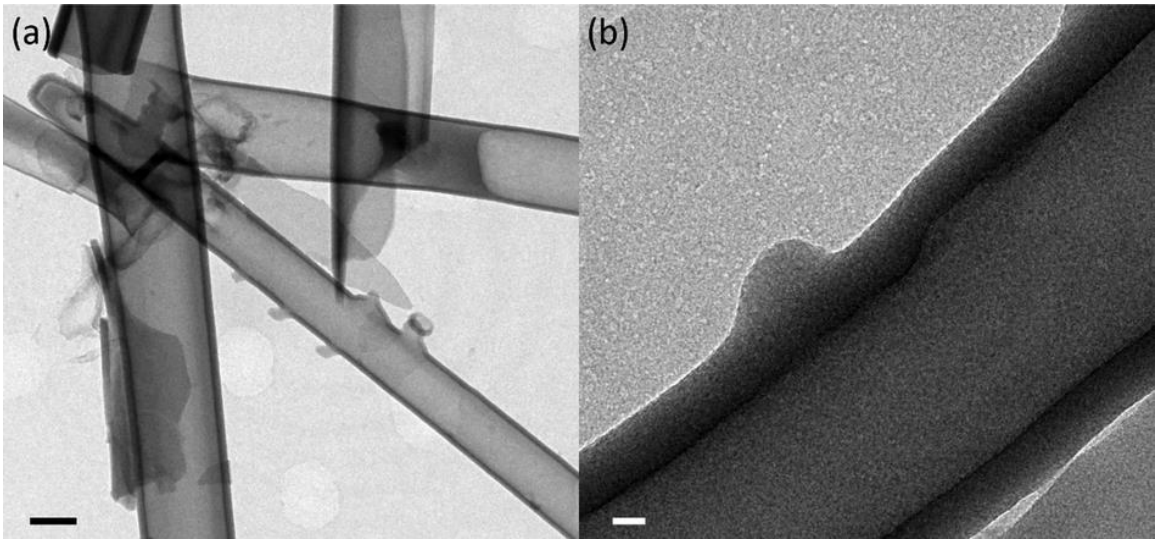

Figure 3.7 (a) TEM image of an isolated SiO_2 NT after 100 galvanostatic charge-discharge cycles. (b) Higher magnification TEM image of the same SiO_2 NT emphasizing tube wall thickness and morphology. The scale bars are 200 nm and 20 nm for (a) and (b), respectively.

3.5 Conclusions

SiO_2 NTs have been fabricated via facile two step templated process through thermal degradation of PDMS in air under vacuum. This environmentally friendly synthesis route uses abundant, non-toxic, and non-flammable precursors and yields SiO_2 NTs that produce a capacity of 1266 mAh g^{-1} after 100 cycles with minimal capacity fading. Galvanostatic cycling reveals a noticeable increase in capacity over the first 80 cycles, which is attributed to growth of a nano-Si phase upon generation of Li_ySiO_2 at Si/SiO_2 boundaries. The electrochemical performance of SiO_2 NTs is promising in

comparison to conventional graphite anodes and other published silica-based anode materials.

However, several negative conclusions can be drawn regarding the potential applications of this technology in real world LIBs. The synthesis of SiO_2 NTs relies on the use of AAO templates which are ~$20.00 for 47 mm diameter templates. A single 47 mm diameter template can produce as much as ~45 mg of SiO_2 NTs with a wall thickness of 20 nm. Considering the cost of only the template yields a SiO_2 NT cost of ~$445.00 g^{-1}, which is extraordinarily high for production on a large scale. This cost excludes the cost of the PDMS rubber and the energy required to perform the CVD of SiO_2 onto AAO. The AAO template is also sacrificed after it is coated with SiO_2, meaning the templates are not reusable as would be desired. While the number of templates used in a single CVD process can be increased to produce more material, the cost of the templates significantly hinders large scale applications of this technology as it does with other AAO based technologies.

Due to silica's high resistivity as an insulator, SiO_2 NT anodes cannot be cycled at current densities like those used for semiconductors such as Si or conductors such as 2D carbon allotropes. In real applications, users desire charging times approaching <1h, which is especially true for mobile electronics and future EVs. Hence, SiO_2 NTs may not be suitable for high power applications without the addition of conductive surface coatings. Despite this, the cost of synthesis alone may hinder large scale applications of SiO_2 NTs in LIBs.

3.6 References

1 Yaroshevsky, A. A. Abundances of Chemical Elements in the Earth's Crust. *Geochem. Int.* **44**, 48-55 (2006).

2 Chang, W.-S. *et al.* Quartz (SiO_2): a new energy storage anode material for Li-ion batteries. *Energy Environ. Sci.* **5**, 6895-6899 (2012).

3 Yan, N. W., Fang Zhong, Hao Li, Yan Wang, Yu Hu, Lin Chen, Qianwang. Hollow Porous SiO_2 Nanocubes Towards High-performance Anodes for Lithium-ion Batteries. *Sci. Rep.* **3** (2013).

4 Song, K. *et al.* Hierarchical SiO_x nanoconifers for Li-ion battery anodes with structural stability and kinetic enhancement. *J. Power Sources* **229**, 229-233 (2013).

5 Kim, T., Park, S. & Oh, S. M. Solid-State NMR and Electrochemical Dilatometry Study on Li^+ Uptake/Extraction Mechanism in SiO Electrode. *J. Electrochem. Soc.* **154**, A1112-A1117 (2007).

6 Miyachi, M., Yamamoto, H., Kawai, H., Ohta, T. & Shirakata, M. Analysis of SiO Anodes for Lithium-Ion Batteries. *J. Electrochem. Soc.* **152**, A2089-A2091 (2005).

7 Guo, B. *et al.* Electrochemical reduction of nano-SiO_2 in hard carbon as anode material for lithium ion batteries. *Electrochem. Commun.* **10**, 1876-1878 (2008).

8 Mitchell, B. S. *An Introduction to Materials Engineering and Science: For Chemical and Materials Engineers*. (John Wiley & Sons, Inc., 2004).

9 Yao, Y., Zhang, J., Xue, L., Huang, T. & Yu, A. Carbon-coated SiO_2 nanoparticles as anode material for lithium ion batteries. *J. Power Sources* **196**, 10240-10243 (2011).

10 Kim, J.-H., Sohn, H.-J., Kim, H., Jeong, G. & Choi, W. Enhanced cycle performance of SiO-C composite for lithium-ion batteries. *J. Power Sources* **170**, 456-459 (2007).

11 Sun, Q., Zhang, B. & Fu, Z.-W. Lithium electrochemistry of SiO_2 thin film electrode for lithium-ion batteries. *Appl. Surf. Sci.* **254**, 3774-3779 (2008).

12 Li, X. *et al.* Nanoporous tree-like SiO_2 films fabricated by sol-gel assisted electrostatic spray deposition. *Micropor. Mesopor. Mat.* **151**, 488-495 (2012).

13 AISBL, E. Linear Polydimethylsiloxanes. (European Centre for Ecotoxicology and Toxicology of Chemicals, Joint Assessment of Commodity Chemicals, 2011).

14 Graiver, D., Farminer, K. W. & Narayan, R. A Review of the Fate and Effects of Silicones in the Environment. *J. Polym. Environ.* **11**, 129-136 (2003).

15 Camino, G., Lomakin, S. M. & Lazzari, M. Polydimethylsiloxane Thermal Degredation Part 1. Kinetic Aspects. *Polymer* **42**, 2395-2402 (2001).

16 Camino, G., Lomakin, S. M. & Lageard, M. Thermal polydimethylsiloxane degradation. Part 2. The degradation mechanisms *Polymer* **43**, 2011-2015 (2002).

17 Wang, Z., Zhou, L. & Lou, X. W. D. Metal Oxide Hollow Nanostructures for Lithium-ion Batteries. *Adv. Mater.* **24**, 1903-1911 (2012).

18 Wang, J., Du, N., Zhang, H., Yu, J. & Yang, D. Large-Scale Synthesis of SnO2 nanotube Arrays as High-Performance Anode Materials of Li-Ion Batteries. *J. Phys. Chem. C* **115**, 11302-11305 (2011).

19 Wu, H. *et al.* Engineering Empty Space between Si Nanoparticles for Lithium-Ion Battery Anodes. *Nano Lett.* **12**, 904-909 (2012).

20 Wang, B. *et al.* Contact-Engineered and Void-Involved Silicon/Carbon Nanohybrids as Lithium-Ion-Battery Anodes. *Adv. Mater.* **25**, 3560-3565 (2013).

21 Hu, Y., Ge, J. & Yin, Y. PDMS rubber as a single-source precursor for templated growth of silica nanotubes. *Chem. Commun.*, 914-916 (2009).

22 Kasi, A. K., Kasi, K. J., Afzulpurkar, N., Hasan, M. M. & Mahaisavariya, B. Bending and branching of anodic aluminum oxide nanochannels and their applications. *J. Vac. Sci. Technol. B.* **30**, 031805-031807 (2012).

23 Obravac, M. N. & Christensen, L. Structural Changes in Silicon Anodes during Lithium Insertion/Extraction. *Electrochem. Solid-State Lett.* **7**, A93-A96 (2004).

24 Wu, H. & Cui, Y. Designing nanostructured Si anodes for high energy lithium ion batteries. *Nanotoday* **7**, 414-429 (2012).

25 Tee, J. C., Sanip, S. M., Aziz, M. & Ismail, A. F. Template Synthesis of Carbon Nanotubes. *AIP Conference Proceedings* **1217**, 217-221 (2009).

26 Nadimpalli, S. P. V. *et al.* Quantifying capacity loss due to solid-electrolyte-interphase layer formation on silicon negative electrodes in lithium-ion batteries. *J. Power Sources* **215**, 145-151 (2012).

27 Schroder, K. W., Celio, H., Webb, L. J. & Stevenson, K. J. Examining Solid Electrolyte Interphase Formation on Crystalline Silicon Electrodes: Influence of Electrochemical Preparation and Ambient Exposure Conditions. *J. Phys. Chem. C* **116**, 19737-19747 (2012).

28 Ren, Y. *et al.* Preparation and characterization of silicon monoxide/graphite/carbon nanotubes composite as anode for lithium-ion batteries. *J. Solid State Electrochem.* **16**, 1453-1460 (2012).

29 Jiang, T., Zhang, S., Lin, R., Liu, G. & Liu, W. Electrochemical Characterization of Cellular Si and Si/C Anodes for Lithium Ion Battery. *Int. J. Electrochem. Sci.* **8**, 9644-9651 (2013).

30 Yang, J., Takeda, Y., Capiglia, C., Xie, J. Y. & Yamamoto, O. SiO_x-based anodes for secondary lithium batteries. *Solid State Ionics* **152-153**, 125-129 (2002).

31 Ban, C. *et al.* Lithiation of silica through partial reduction. *Appl. Phys. Lett.* **100** (2012).

32 Wu, H. *et al.* Stable cycling of double-walled silicon nanotube battery anodes through solid-electrolyte interphase control. *Nat. Nanotechnol.* **7**, 310-315 (2012).

Chapter 4 Nano-Silicon from Beach Sand via MTR

4.1 Introduction

Despite researchers developing hundreds of novel Si-based anode materials that outperform graphite in terms of capacity by several times (including one discussed in the previous chapter), very few have demonstrated the ability to be scaled to the industry level in a manner that is environmentally friendly and low cost. While the electrochemical performance of these Si-based anodes is an important consideration when bringing a technology to industry, the scalability is of equal importance in determining the viability of the technology in consumer applications which require large production volumes. LIBs used in portable electronics and electric vehicles are produced in massive quantities and sold to consumers around the world. The energy storing materials in these batteries constitute a large portion of the final cost of these LIBs.

In order to address the issue of scalability while maintaining superior electrochemical performance I demonstrated a highly scalable synthesis route for producing high-performance nano-Si powder from beach sand (or in general, sand). Sand, depending on the location, is composed of a myriad of minerals that have been pulverized over millions of years by natural forces. Visibly, sands take on numerous colors which is indicative of the minerals dispersed in the sand, ranging from white sand deposits (high quartz content), brown sand deposits (zircon), to black sand deposits (augite and magnetite). The composition and location of these deposits, whether marine or continental must be taken into account as well when deciding on harvesting a raw material in large quantities. Within the scope of this work, a sand that has a high concentration of fine-grained quartz is the most ideal raw material. A high quartz content is critical because we desire to maximize the overall yield of the process. For example, starting with a sand that is 90

wt.% quartz allows for a maximum yield of 42.03% (90% * 46.7%) while a sand that is only 50 wt.% quartz allows for a maximum yield of 23.35% (50% * 46.7%). These numbers are based on the fact that quartz is ~46.7 wt.% silicon, which is the final material that will be produced.

Another desirable attribute is to have relatively small sand grain size, which is accomplished via natural pulverization processes over millions of years. Carbothermic reduction uses high purity quartzite rock as its SiO_2 source. Harvesting quartzite rock requires extensive mining operations that incur large energy and monetary budgets. In contrast, sand has already been crushed by natural forces into a fine powder and lies largely on the surface of the earth, which means minimal destructive mining operations are required and less energy must be expended. In turn, we only have to pulverize the fine-grained sand into a fine mesh size via milling. If we start with large quartzite rock, significant energy and time must be expended to get the quartzite to a comparable mesh size. Sand, too, comes in various mesh sizes that must be considered when selecting a sand source.

When considering a technology for large scale applications such as LIBs, one must consider the production and life cycle roadmap that must be taken to produce a material and not just the performance said material can deliver. Starting from its undisturbed place in nature all the way through its lifetime until it is considered waste, all steps in a material's life incur environmental and monetary costs. Silicon nanostructures derived from the pyrolization of silane (SiH_4), such as silicon nanospheres, nanotubes, and nanowires, have all demonstrated excellent electrochemical performance.[1-3] However, CVD using highly toxic, expensive, and pyrophoric silane requires costly setups and cannot produce anode material on the industry level.[4] MACE of crystalline silicon wafers has been extensively

investigated (here and elsewhere) as a means of producing highly tunable silicon nanowires via templated and non-templated approaches.[5,6] However, electronic grade wafers are relatively costly to produce and the amount of nanowires produced via MACE is on the milligram level.[5] Crystalline wafers have also been used to produce porous silicon via electrochemical anodization in an HF solution.[7] Again, anodization is a lengthy and energy intensive process, which is added to the already high cost of the crystalline Si wafers.

As before, quartz (SiO_2) itself has been demonstrated as a high capacity anode material without further reduction to silicon, with a reversible capacity of ~800 mAh g^{-1} over 200 cycles.[8] However, SiO_2 is a wide bandgap insulator with a conductivity ~10^{11} times lower than that of silicon.[9] Additionally, SiO_2 anodes carry 53.3% by weight oxygen which reduces the gravimetric capacity of the anodes. The highly insulating nature of SiO_2 is also detrimental to the rate capability of these anodes.[10] Tetraethyl orthosilicate (TEOS) has garnered significant attention recently due its ability to produce nano-SiO_2 via hydrolysis.[11] The SiO_2 has been subsequently reduced to silicon in such structures as nanotubes and mesoporous particles.[2,12] However, examining Figure 4.1a reveals the extensive production process needed to produce TEOS; each step incurring added costs and environmental impacts. Conversely, Liu et al. have demonstrated a method of synthesizing nano-Si via magnesiothermic reduction (MTR) of rice husks (SiO_2), an abundant by-product of rice production measured in megatons per year.[13] However, material synthesis technologies linked to food staples are unattractive due to the possible instabilities in that staple's production and strain on existing food supply chains.

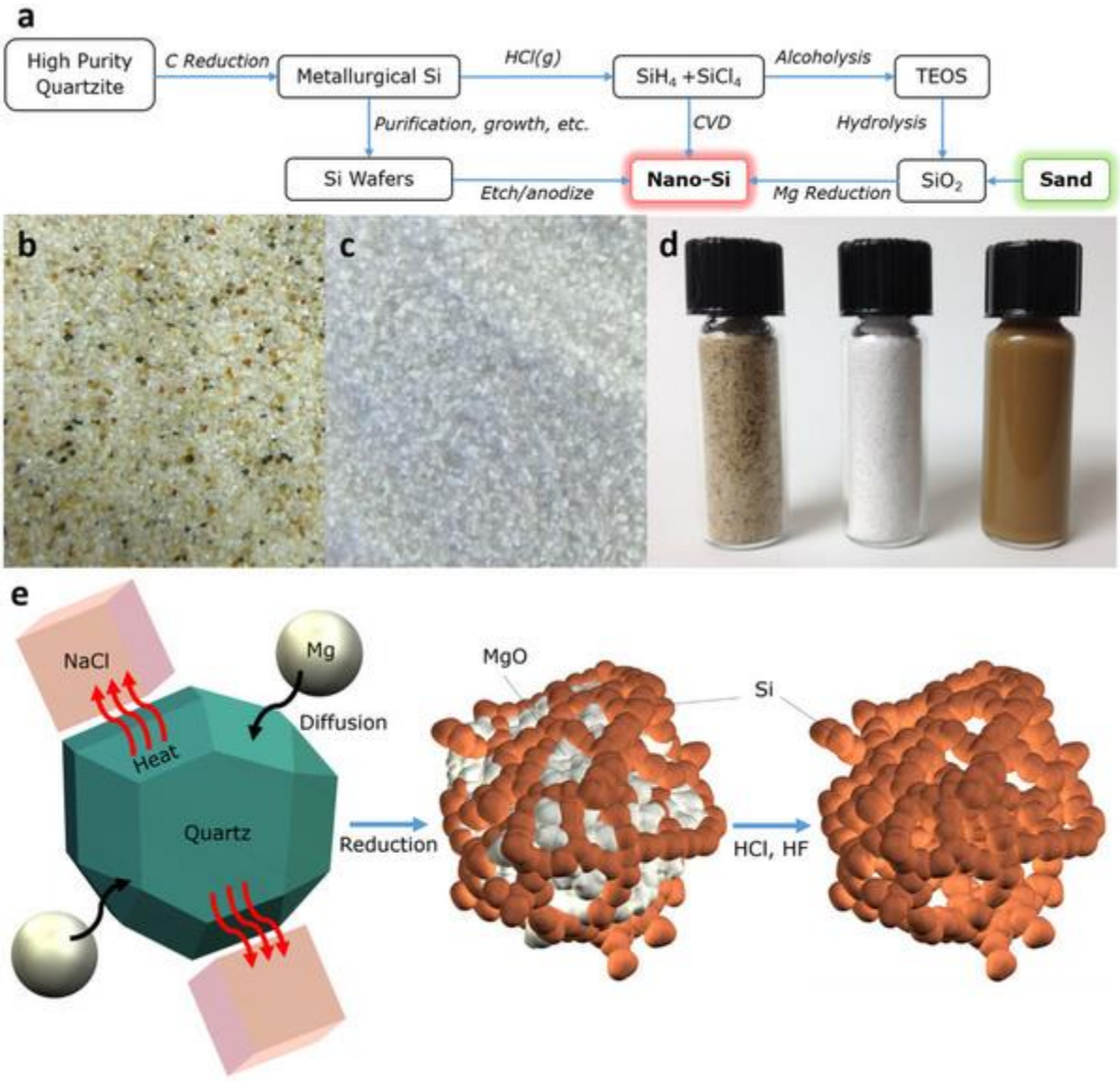

Figure 4.1 (a) Flow chart showing conventional synthesis routes of nano-Si, including the introduction of my synthesis route from sand. Optical images of (b) unpurified sand, (c) purified sand, and (d) (from left to right) vials of unpurified sand, purified sand, and nano-Si. (e) Schematic of the heat scavenger-assisted Mg reduction process.

Recently, MTR has gained attention due its much lower operating temperatures (~650°C). Typically, Mg powder is placed adjacent to SiO_2 powder and the furnace is heated until the Mg vaporizes. However, this reduction scheme produces zonal variations in composition with Mg_2Si forming near the Mg powder, Si in the middle, and unreacted SiO_2 furthest from the Mg.[12] Luo *et al.* have shown that adding a relatively large amount of NaCl to the reduction process aids in scavenging the large amount of heat generated during this highly exothermic reaction. NaCl effectively halts the reaction temperature rise at 801°C during fusion, preventing the reaction from surpassing the melting point of silicon and thus aiding in preserving the original SiO_2 morphology.[14] Herein, I propose a facile and low cost alternative to production of nano-Si with excellent electrochemical performance using a highly abundant, non-toxic, and low cost Si precursor: sand.

4.2 Synthesis of Nano-Si via MTR of Sand

The sand used in this analysis was collected from the loamy surface of the shores of Cedar Creek Reservoir in the Claypan region of Texas. The soil of this region is classified as an Alfisol, specifically a Paleustalf, comprising >90% quartz with minor amounts of feldspars and chert.[15,16] The sand grains utilized herein have a grain size of ~0.10 mm, as in Figure 4.1b. Further mechanical milling by hand in an alumina mortar easily reduces the grain size to the micrometer and nanometer scale within minutes. At an industrial level this milling would be accomplished via ball milling, but for the purposes of this lab-scale investigation hand milling produces significant quantities of powder. Organic species are removed via washing and ultrasonication with DI water, acetone, and

isopropyl alcohol. Unwanted silicate species are removed via a 49% HF etch, as crystalline quartz etches much slower than other silicate species such as feldspars.[17] The HF etch consumes quartz to some degree, but more importantly is its ability to consume unwanted mineral species at a faster rate than quartz. In most cases, about 50% of the original mass of the sand is lost to these purification steps. After purification, the sand assumes a bright white appearance in stark contrast to the brown hue of the unpurified sand, as in Figure 4.1c. The peaks associated with unpurified sand in the XRD analysis in Figure 4.2a confirm that the sample comprises mostly quartz with very minor peaks corresponding to impurities. After purifying the sand, the peaks associated with quartz greatly increase in intensity relative to the impurity peaks, confirming that most of the impurities have been successfully etched away.

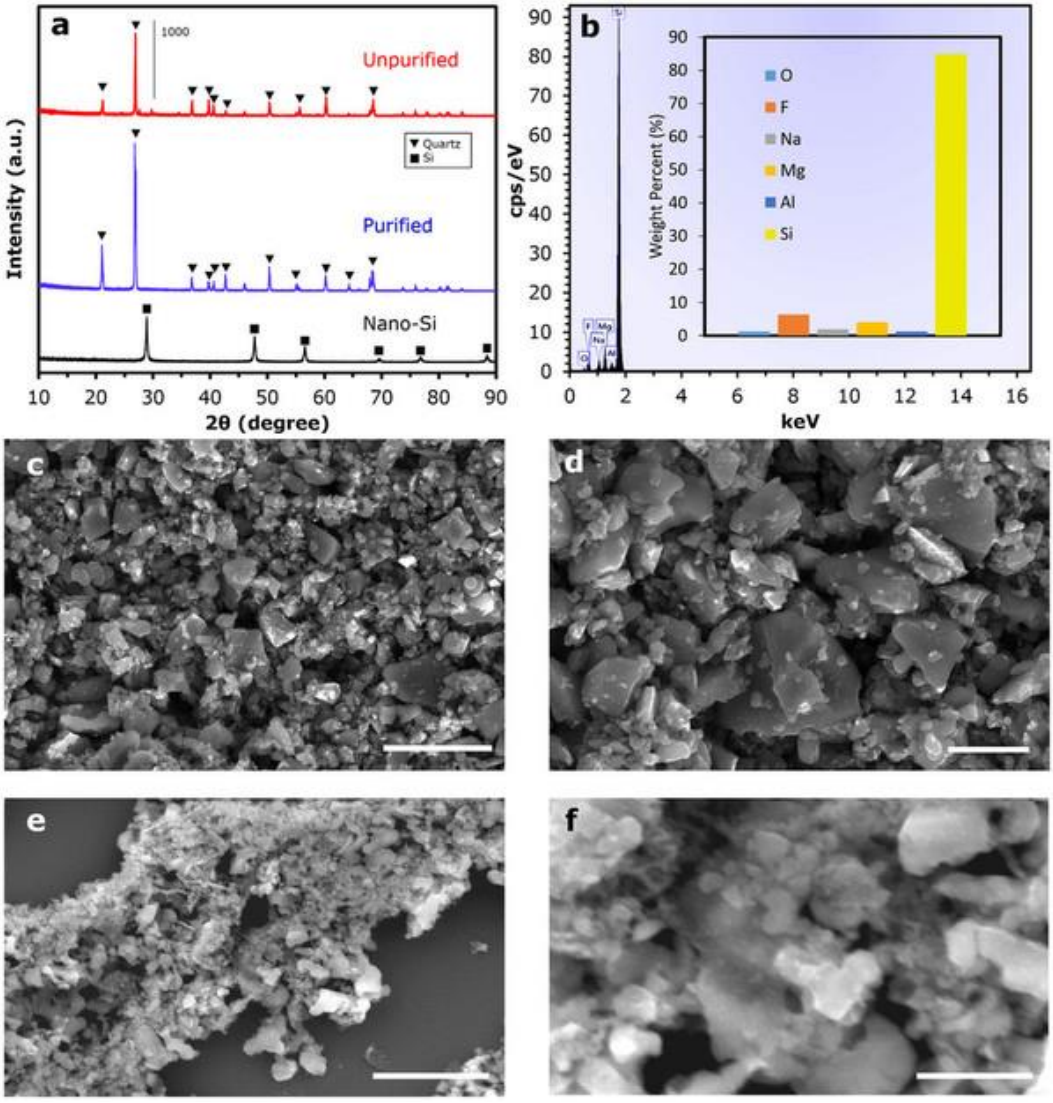

Figure 4.2 (a) XRD plot displaying characteristic peaks of quartz in both pre-reduction samples and Si peaks in the post-reduction nano-Si. (b) EDS analysis with inset displaying weight percent of elements in nano-Si after HCl and HF etching. Low magnification (c) and higher magnification (d) SEM images of quartz powder after purification and milling. Low magnification (e) and higher magnification (f) SEM images of nano-Si after reduction and etching. Scale bars for (c),(d), (e), and (f) are 5µm, 2µm, 2µm, and 500 nm, respectively.

After purification, quartz powder and NaCl are ground together in a 1:10 SiO_2:NaCl weight ratio and ultrasonicated and vigorously stirred for 2 hours. After drying, the SiO_2:NaCl Powder is ground together with Mg powder in a 1:0.9 SiO_2:Mg weight ratio. The resultant powder is loaded into Swagelok-type reactors and sealed in an argon-filled (0.09 ppm O_2) glovebox. The reactors are immediately loaded into a 1" diameter quartz tube furnace purged with argon. The furnace is slowly heated at 5°C min^{-1} to 700°C and held for 6 hours to ensure complete reduction of all SiO_2. This slow heating rate is crucial for avoiding melting of the silicon. Heat added by the furnace in conjunction with the large amount of heat generated from the MTR can create local hot spots that may melt Si.

The ability to mitigate the volume expansion related effects is due to the ability to produce a highly porous interconnected 3D network of nano-Si. This is achieved via the addition of a relatively large amount or NaCl, which serves to absorb the large amount of heat generated in this highly exothermic Mg reduction, as in Equation. 4.1.

$$2Mg(g) + SiO_2 \rightarrow Si(s) + 2MgO(s) \quad (4.1)$$

$$Mg(g) + Si(s) \rightarrow Mg_2Si(s) \quad (4.2)$$

Mg reduction evolves a large amount of heat that can cause local melting of Si and, consequently, aggregation of nano-Si particles (Mg (*g*): $\Delta H = -586.7$ kJ/mol_{SiO2}).[14] However, by surrounding the milled quartz particles with a large amount of NaCl (ΔH_{fusion} = 28.8 kJ/mol) the heat is used in the fusion of NaCl rather than in the fusion of Si. Additionally, NaCl is a highly abundant, low cost, and environmentally benign salt that can be subsequently recycled for further reductions. We also observe that the addition of NaCl also serves to reduce the presence of Mg_2Si, an unwanted product that can result from

excess Mg alloying with Si, as in Equation 2. Etching of this silicide with HCl produces silane, which is a highly toxic and pyrophoric gas. The presence of Mg_2Si also reduces the overall yield of the reduction process.

After reduction the resulting brown powder is washed with DI water to remove NaCl and then etched with 1 M HCl for 6 hours to remove Mg, Mg_2Si, and MgO. The $MgCl_2$ that is produced via HCl etching of MgO can be easily recycled back to Mg via electrolysis, which is the predominant industrial synthesis route for Mg production.[18] The powder is washed several times with DI H_2O and EtOH to remove the etchant and dried overnight under vacuum. A visual comparison, without magnification, of unpurified beach sand, purified quartz, and nano-Si stored in glass vials can be seen in Figure 4.1d, and the entire synthesis process can be visualized in Figure 4.1e.

4.3 Characterization of Nano-Si

SEM imaging in Figure 4.2 reveals the broad size distribution and highly irregular morphology of the milled quartz powder before and after reduction. For the milled quartz powder, the particle size ranges from several microns to 50 nm, as in Figure 4.2c and 4.2d. The quartz powder and nano-Si reduction product are both highly irregular in shape as expected. After reduction, the nano-Si is absent of particles with dimensions in excess several microns and has a much smaller size distribution than the quartz powder, as in Figure 4.2e and 4.2f. We can attribute this to the breakdown of relatively larger particles during reduction and ultrasonication, which is due to the reduced mechanical integrity of the porous 3D nano-Si networks in comparison to the solid pre-reduction quartz particles.

In lieu of the solid crystalline particles found in the quartz powder, the nano-Si powder is composed of a highly porous network of interconnected crystalline silicon nanoparticles (SiNPs).

HRTEM in Figure 4.3a and 4.3b reveals the interconnected SiNPs that comprise the 3D Si networks, and the diameter of the SiNPs is ~8–10 nm, with larger particles existing sparingly. This high porosity can be attributed to the selective etching of imbedded MgO and Mg_2Si particles after reduction. Through the use a NaCl as a heat scavenger during the reduction process, I am able to synthesize a highly uniform porous structure throughout the width of the particle by avoiding localized melting of Si. This uniform 3D network is achieved via removal of oxygen (53.3% by weight) from the original quartz particles through reduction and a conservation of volume via the heat scavenger (NaCl). The XRD peaks in Figure 4.2a indicate a successful reduction to silicon after Mg reduction.

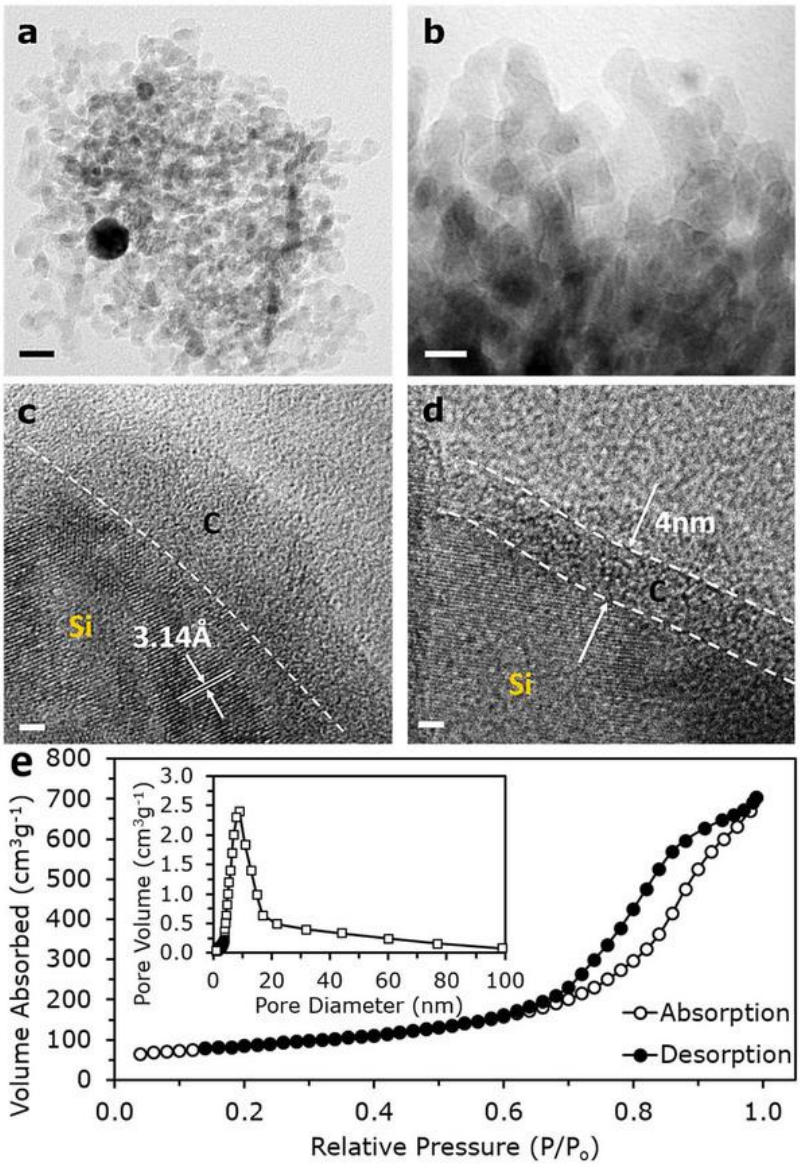

Figure 4.3 Low magnification (a) and high magnification (b) TEM images of nano-Si. (c) HRTEM image of nano-Si showing the conformal carbon coating and characteristic lattice spacing of Si(111). (d) HRTEM image of C-coated nano-Si showing thickness of the carbon layer. Scale bars for (a), (b), (c), and (d) are 20 nm, 10 nm, 2 nm, and 2 nm, respectively. (e) BET surface area measurements of nano-Si with type IV N_2 sorption isotherms and inset showing pore diameter distribution.

Energy Dispersive X-ray Spectroscopy (EDS) in Figure 4.2b reveals the weight percentage of elements present in the nano-Si powder. The quantitative analysis shows Si is the predominant element present with non-negligible amounts of F, Na, Mg, Al, and O. The F and Na peaks may be due to the existence of Na_2SiF_6, which is produced via a reaction between residual NaCl and H_2SiF_6 produced during HF etching of SiO_2. The existence of Al may be derived from the original sand or from the alumina mortar. While the existence of metallic contaminants at these levels may present deleterious effects for some applications, for battery applications these metallic impurities may increase the conductivity of nano-Si. Despite silicon's relatively high surface diffusion capability with respect to bulk diffusion of Li, silicon has relatively low electrical conductivity.[19] Thus, nano-Si powders were conformally coated with a ~4 nm amorphous carbon coating to enhance conductivity across all surfaces, as in Figure 4.3c and 4.3d.

Briefly, nano-Si powder was loaded into a quartz boat and placed in the center of a quartz tube furnace purged with an H_2/Ar mixture. After heating to 950°C, acetylene was introduced into the tube to produce a conformal C-coating. The weight ratio of Si to C was determined to be 81:19 after coating. Brunauer-Emmett-Teller (BET) surface area measurements were performed for nano-Si before C-coating yielding a specific surface area of 323 m^2g^{-1}, as in Figure 4.3e. The inset in Figure 4.3e reveals a pore diameter distribution with a peak centered at 9 nm. The pore diameter is in good agreement with the TEM images of porous nano-Si. This high surface area confirms that NaCl effectively scavenges the large amount of heat generated during Mg reduction, preventing agglomeration of nano-Si. The high surface area and pore volume distribution also confirm

the existence of large internal porosity available for volume expansion buffering and, thus, minimal capacity fading due to SEI layer degradation and active material pulverization.

4.4 Electrochemical Characterization of Nano-Si

Nano-Si@C derived from sand was electrochemically characterized using the half-cell configuration with Li-metal as the counter-electrode. Electrodes comprised nano-Si@C, AB, and PAA in a 7:1:2 nano-Si@C:AB:PAA weight ratio. Figure 4.4a demonstrates the rate capability of the C-coated nano-Si electrodes up to the C/2 rate, with additional cycling up to 1000 cycles at the C/2 rate. Initial cycling at C/40 is necessary for proper activation of all Si and development of a stable SEI layer. This activation process is confirmed via cyclic voltammetry measurements, as in Figure 4.4b. The peaks corresponding to the lithiation (0.22 V and 0.10 V) and delithiation (0.33 V and 0.50 V) grow in intensity over the first 12 cycles before stabilizing, which suggests a kinetic enhancement occurs in the electrode. After a kinetic enhancement is achieved via this low current density activation process, the electrodes are cycled at much higher rates. Even at the C/2 rate the nano-Si electrodes demonstrate a reversible capacity of 1024 mAh g^{-1} and a CE of 99.1% after 1000 cycles. The excellent cycle stability of the nano-Si@C electrodes can be attributed to a combination of the conformal C-coating, PAA binder, and the porous 3D nano-Si network.

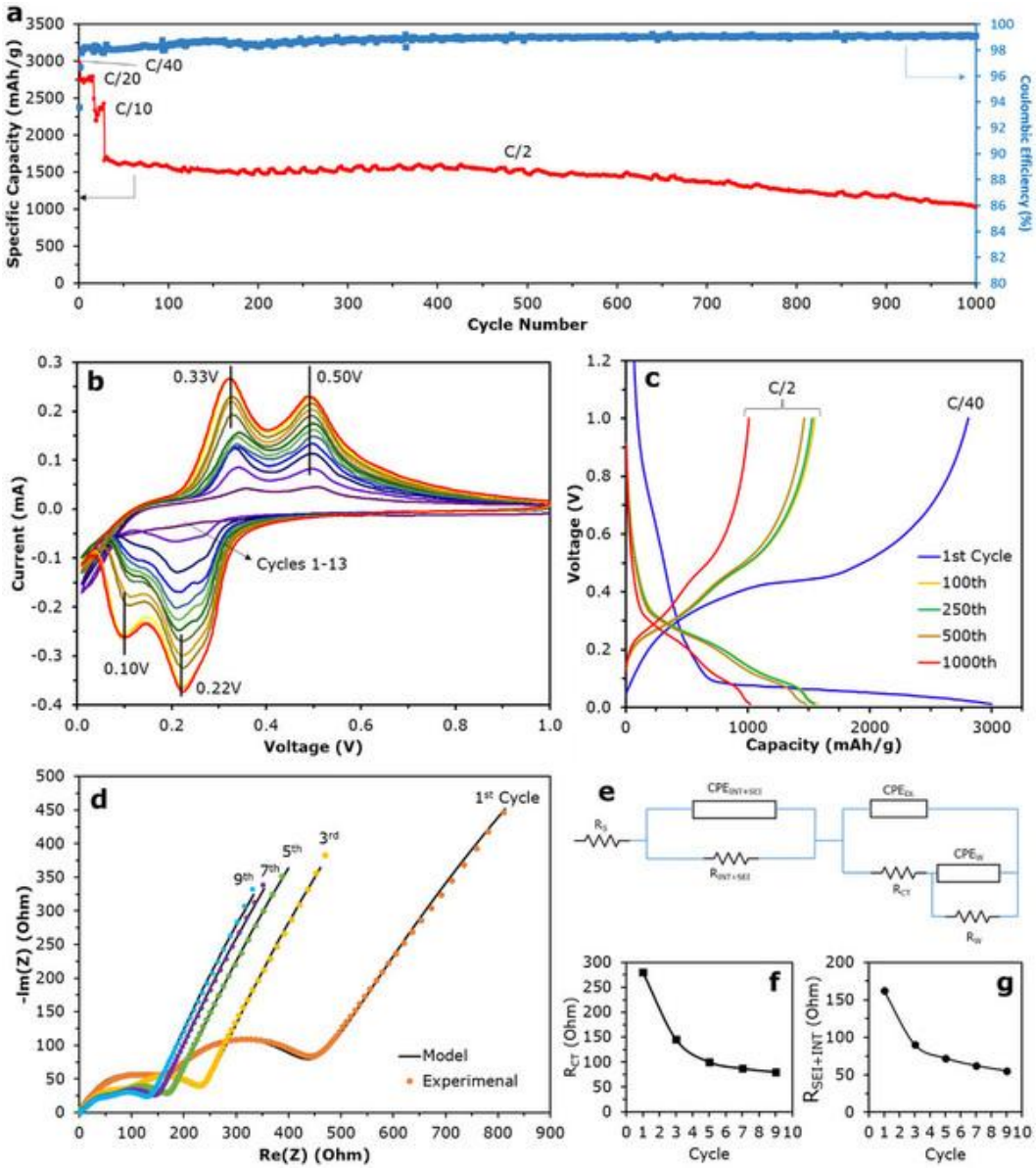

Figure 4.4 (a) Cycling data of nano-Si@C anodes with selected C-rates (C = 4 A g^{-1}). (b) CV plot of the first 13 cycles using a scan rate of 0.02 mV s^{-1}. (c) Charge-discharge curves for selected cycles. (d) EIS curves for selected cycles showing both experimental and fitted-model data. (e) Equivalent circuit of nano-Si@C electrodes used to produce fitted-model data. Extracted resistance values from the EIS curves for (f) charge transfer resistance and (g) SEI + INT resistance.

The addition of a C-coating alters the makeup of the SEI layer and may also partially alleviate the lithiation-induced volume expansion effects in nano-Si.[20] The use of PAA as the binder also greatly enhances the cyclability of the electrodes. Magasinski *et al.* have recently reported on the improved cycling performance of PAA-bound electrodes relative to conventionally used binders such as PVDF and carboxymethylcellulose (CMC).[21] The improved stability is attributed to PAA's similar mechanical properties to that of CMC but higher concentration of carboxylic functional groups. The mechanical properties of PAA prevent the formation of large void spaces created during lithiation and delithiation of Si. The higher concentrations of carboxylic groups form strong hydrogen bonds with hydroxyl groups on C and Si, minimizing separation of binder from active material during cycling. The porous nature of the nano-Si is also partly responsible for the good cyclability due to the internal void space available for the interconnected network of Si to expand. Despite the fact that some of the 3D nano-Si networks have diameters of several hundreds of nanometers, the SiNPs that comprise these networks are only 8–10 nm in diameter.

Complex impedance plots for nano-Si@C anodes obtained via potentiostatic electrochemical impedance spectroscopy (PEIS) are shown in Figure 4.4. The equivalent series resistance (ESR), or high frequency real axis intercept, decreases for the first 5 cycles and stabilizes thereafter. The high frequency semicircle also decreases in diameter with cycling, represented by $R_{SEI + INT}$. This is the resistance representing the SEI layer and resistance resulting from imperfect contact between current collector and active material. This contact impedance decreases with cycling, as in Figure 4.4g. The mid frequency

semicircle representing charge transfer impedance decreases sharply for the first 5 cycles, and stabilizes thereafter, as in Figure 4.4f. Interfacial impedance remains fairly constant with increasing number of cycles. Therefore, contact impedance among the active particles and the current collector is not affected by cycling. Evidently, the nano-Si@C anodes are not drastically affected by the volume expansion of a typical Si-based anode.

The PEIS measurements performed after 1^{st}, 3^{rd}, 5^{th}, 7^{th}, and 9^{th} cycles show two distinct arcs. The high frequency semicircle corresponds to SEI film and contact impedance while the mid frequency semicircle corresponds to charge transfer impedance on electrode-electrolyte interface.[22] The Warburg element represents impedance due to diffusion of ions into the active material of the electrode.[23] The low-frequency (<200 MHz) Warburg impedance tail can be attributed to bulk diffusional effects in nano-Si This includes the diffusion of salt in the electrolyte and lithium in the nano-Si@C electrodes.[24] We observe that the biggest change occurs in impedance between the 1^{st} and the 5^{th} cycle. The change in impedance hereafter (from 5^{th} cycle to 9^{th} cycle) is relatively less pronounced, confirming that the anode tends to stabilize as it is repeatedly cycled.

4.5 Conclusions

A highly scalable, low cost, and environmentally benign synthesis route for producing nano-Si with outstanding electrochemical performance over 1000 cycles has been demonstrated. The outstanding performance of the nano-Si@C electrodes can be attributed to a number of factors including the highly porous interconnected 3D network of nano-Si, the conformal 4 nm C-coating, and the use of PAA as an effective binder for C

and Si electrodes. Nano-Si@C electrode fabrication follows conventional slurry-based methods utilized in industry and offers a promising avenue for production of low cost and high-performance Si-based anodes for portable electronics and electric vehicle applications.

The production of nano-Si from sand offers an environmentally friendly route for synthesis of next-generation LIB materials based on its use of MTR and carbon neutral approach. Obviously, one must consider the energy input required to perform all of the processes listed herein, but that is beyond the immediate scope of this thesis. Most importantly is the scalability demonstrated in this investigation. Even at the lab scale, a single MTR batch can produce 500 mg of nano-Si, which is only limited by the reaction vessel size (fits in the palm of your hand). Achieving gram-level production at the lab scale highlights the ease of scalability to the industry scale. The use of low cost and carbon free precursors, Mg and quartz, makes this synthesis route highly attractive for large scale production.

The electrochemical performance of nano-Si is far superior to conventionally used graphite but can be improved in the future. Better purification of the material may result in higher capacities. Use of graphene oxide powders in lieu of a CVD carbon coating process would decrease the energy required in the synthesis roadmap while potentially increasing electrochemical performance. In this manner, the synthesis is more powder-based, which is the most common method for production of LIB electrodes in industry.

4.6 References

1 Ge, M., Rong, J., Fang, X. & Zhou, C. Porous Doped Silicon Nanowires for Lithium Ion Battery Anode with Long Cycle Life. *Nano Lett.* **12**, 2318-2323 (2012).

2 Yoo, J.-K., Kim, J., Jung, Y. S. & Kang, K. Scalable Fabrication of Silicon Nanotubes and their Application to Energy Storage. *Adv. Mater.* **24**, 5452-5456 (2012).

3 Yao, Y. *et al.* Interconnected Silicon Hollow Nanospheres for Lithium-Ion Battery Anodes with Long Cycle Life. *Nano Lett.* **11**, 2949-2954 (2011).

4 Kondo, S., Tokuhashi, K., Nagai, H., Iwasaka, M. & Kaise, M. Spontaneous ignition limits of silane and phosphine. *Combust. Flame* **101**, 170-174 (1995).

5 Vlad, A. *et al.* Roll up nanowire battery from silicon chips. *PNAS* **109**, 15168-15173 (2012).

6 Huang, Z. *et al.* Extended Arrays of Vertically Aligned Sub-10 nm Diameter [100] Si Nanowires by Metal-Assisted Chemical Etching. *Nano Lett.* **8**, 3046-3051 (2008).

7 Sun, X., Huang, H., Chu, K. & Zhuang, Y. Anodized Macroporous Silicon Anode for Integration of Lithium-Ion Batteries on Chips. *J. Electron. Mater.* **41**, 2369-2375 (2012).

8 Chang, W.-S. *et al.* Quartz (SiO_2): a new energy storage anode material for Li-ion batteries. *Energy Environ. Sci.* **5**, 6895-6899 (2012).

9 Mitchell, B. S. *An Introduction to Materials Engineering and Science: For Chemical and Materials Engineers*. (John Wiley & Sons, Inc., 2004).

10 Favors, Z. J., Wang, W., Bay, H. H. George, A., Ozkan, M., Ozkan, C. Stable Cycling of SiO_2 Nanotubes as High-Performance Anodes for Lithium-Ion Batteries. *Sci. Rep.* **4** (2014).

11 Dingsoyr, E. & Christy, A. A. Effect of reaction variables on the formation of silica particles by hydrolysis of tetraethyl orthosilicate using sodium hydroxide as a basic catalyst. *Surf. Colloid Sci.* **116**, 67-73 (2001).

12 Richman, E. K., Kang, C. B., Brezesinski, T. & Tolbert, S. H. Ordered Mesoporous Silicon through Magnesium Reduction of Polymer Templated Silica Thin Films. *Nano Lett.* **8**, 3075-3079 (2008).

13 Liu, N., Huo, K., McDowell, M. T., Zhao, J. & Cui, Y. Rice husks as a sustainable source of nanostructured silicon for high performance Li-ion battery anodes. *Sci. Rep.* **3** (2013).

14 Luo, W. *et al.* Efficient Fabrication of Nanoporous Si and Si/Ge Enabled by a Heat Scavenger in Magnesiothermic Reactions. *Sci. Rep.* **3** (2013).

15 *Land Resource Regions and Major Land Resource Areas of the United States, the Caribbean, and the Pacific Basin*. Vol. 296 (United States Department of Agriculture, 2006).

16 Huang, P. M., Li, Y. & Sumner, M. E. *Handbook of Soil Sciences*. 2nd edn, (CRC Press, 2012).

17 Mauz, B. & Lang, A. Removal of the feldspar-derived luminescence component from polymineral fine silt samples for optical dating applications: evaluation of chemical treatment protocols and quality control procedures. *Ancient TL* **22** (2004).

18 Kipouros, G. J. & Sadoway, D. R. The chemistry and electrochemistry of magnesium production. *Adv. Molt. Salt Chem.* **6**, 127-209 (1987).

19 Zhang, Q., Zhang, W., Wan, W., Cui, Y. & Wang, E. Lithium Insertion In Silicon Nanowires: An ab Initio Study. *Nano Lett.* **10**, 3243-3249 (2010).

20 Yen, Y.-C., Chao, S.-C., Wu, H.-C. & Wu, N.-L. Study on Solid-Electrolyte-Interphase of Si and C-Coated Si Electrodes in Lithium Cells. *J. Electrochem. Soc.* **156**, A95-A102 (2009).

21 Magasinski, A. *et al.* Toward Efficient Binders for Li-ion Battery Si-Based Anodes: Polyacrylic Acid. *ACS Applied Materials and Interfaces* **2**, 3004-3010 (2010).

22 Hu, L. *et al.* $CoMn_2O_4$ spinel hierarchical microspheres assembled with porous nanosheets as stable anodes for lithium-ion batteries. *Sci. Rep.* **3** (2013).

23 Wang, X. & al., e. TiO2 modified FeS Nanostructures with Enhanced Electrochemical Performance for Lithium-Ion Batteries. *Sci. Rep.* **3** (2013).

24 Dees, D., Gunen, E., Abraham, D., Jansen, A. & Prakash, J. Alternating current impedance electrochemical modeling of lithium-ion positive electrodes. *J. Electrochem. Soc.* **152**, 1409-1417 (2005).

Chapter 5 Electrospun SiNFs via MTR

5.1 Introduction

As mentioned prior, one of the major drawbacks of Si as an anode material is its low conductivity relative to other potential anode candidate materials. In light of this, Si has been used it is used in conjunction with conductive matrices such as carbon nanotubes (CNTs), carbon nanofibers (CNFs), or conformal carbon coatings.[1,2] Electrospinning has been extensively used to produce carbonaceous nanofibrous matrices of wide ranges of composition for applications in energy storage. Traditionally, polymers dissolved in organic solvents along with dispersed active material, such as Si or Fe_2O_3, are electrospun to produce polymer fibers with embedded nanoparticles.[3,4] However, these polymer-based fibers can require lengthy thermal oxidative stabilization (TOS) and carbonization steps for applications in energy storage devices.[5] TOS must be performed for many polymers before carbonization can occur in order to prevent melting the nanofibers during carbonization.

Briefly, electrospinning is a very simple technique for creating large quantities of nanoscale materials, generally in a fiber-like form. As in Figure 5.1a, a voltage (5-45 kV) is applied across an air gap (10-12 cm) with the positive terminal usually being a metallic nozzle. The ground (0 kV) is generally a stationary metallic collector plate or in some cases a rotating drum that collects fibers like a spool. Typically, the nozzle emits a polymer-based solution at a controlled rate into a bead on the tip of the nozzle. The large voltage drop applied across the air gap overcomes the surface tension on the droplet to form a Taylor cone, which is pulled into the shape of a fiber. A balance between nozzle pump rate,

applied voltage, solution viscosity, temperature, and humidity is crucial for achieving a continuous fibrous material in lieu of particles, intermittent fibers, or a mix of the two.

Extraordinarily slow heating rates of 1-2^{o}C/min are necessary to avoid melting the polymer during the exothermic TOS, which then must be held at elevated temperatures for lengthy periods of time. Once stabilized, the polymers can then be carbonized to transform the polymer nanofiber matrices into a conductive carbon network. Unfortunately, this lengthy heating steps make many electrospun materials undesirable in an industrial setting. Additionally, the final weight percent of active material in the fibers can be much less than 50% which significantly reduces the total electrode capacity. The majority of the weight of the fibers corresponds to the conductive carbon matrix, which stores much less Li than the embedded active materials.[6]

In industrial settings, battery electrodes are produced via the decades-old slurry method in which metallic current collectors are coated with a slurry comprising an inactive polymer binder, carbon black, and active material dispersed in an organic solvent (usually NMP). However, the necessity of these metal current collectors and inactive polymer binders adds significant cost and weight to the final battery assembly, especially in large battery banks used in EVs. In order for a leap in full cell capacity to occur, significant changes in the way electrodes are manufactured must take place in addition to the introduction of high capacity materials such as Si. Herein, I report on the first synthesis of a binderless Si nanofiber (SiNF) paper with a Si weight percent in excess of 80% for application as LIB anodes, which forgoes the need for inactive polymer binders or metallic current collectors.

5.2 Synthesis and Characterization of SiNFs

SiNF paper is synthesized via MTR of electrospun SiO_2 nanofiber (SiO_2 NF) paper, which is produced by an *in situ* acid-catalyzed polymerization of TEOS in-flight. Two solutions comprising TEOS:EtOH 1:2 (mol:mol) and H_2O:HCl (mol:mol) are prepared separately under vigorous stirring to produce a sol with a 1:1 EtOH:H_2O molar ratio. Once the TEOS comes into contact with water it begins a slow polymerization process through hydrolysis and condensation in the following general fashion (Equation 5.1)[7]:

$$Si(OEt)_4 + 2H_2O \rightarrow SiO_2 + 4EtOH \quad (5.1)$$

TEOS may be catalyzed by minute additions of either an acid or base to produce desired levels of polymerization. Acid-catalyzed polymerization, as used in this work, is slower than base-catalyzed polymerization, but the polymerization proceeds in a much different manner. In acidic sols, TEOS tends to polymerize into long linear molecules that may be cross-linked. These long chains become entangled, forming a viscous gel, as noted in this work during the aging of the sol. This chain entanglement is critical for having the ability to spin nanofibers in contrast to bead-like structures. Base-catalyzed polymerization tends to form short-chained molecules that cluster into individual particle that may produce SiO_2 nanoparticles as in the Stöber method.[8,9] In this sense, base-catalyzed polymerization of TEOS is undesirable for electrospinning.

The sol is aged at 70°C for 2 hours in open air in order to increase the viscosity of the sol; a higher viscosity is necessary for electrospinning to form nanofibers. Aging the sol evaporates a large portion of the ethanol and increases the degree of polymerization.

Once the sol is visibly viscous in a syrup-like state, it is loaded into a polypropylene syringe and connected to an Inovenso Nanospinner Ne300 multinozzle electrospinner.

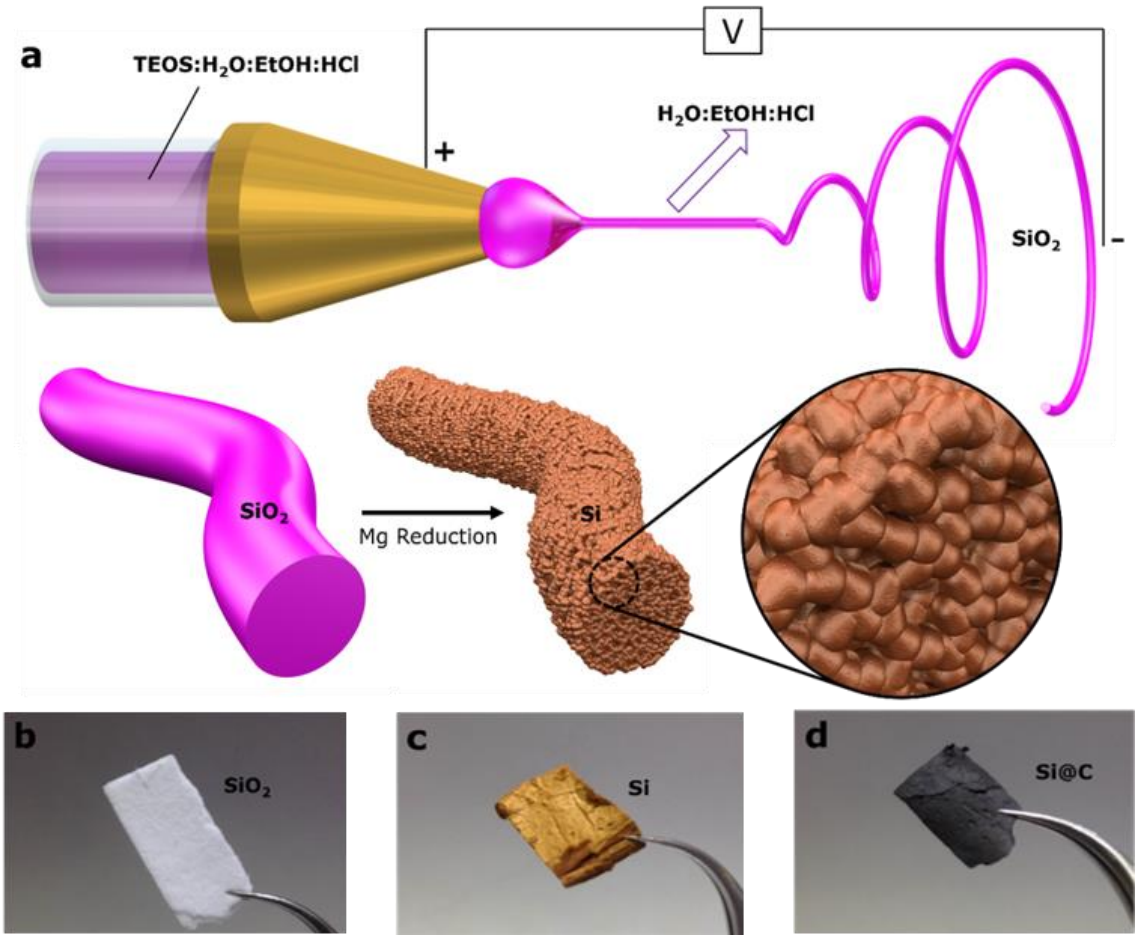

Figure 5.1 (a) Schematic representation of the electrospinning process and subsequent reduction process. Digital photographs of (b) as-spun SiO_2 NF paper, (c) etched SiNF paper, and (d) C-coated SiNF paper as used in the Li-ion half-cell configuration.

After electrospinning, the SiO_2 NF paper sheets were dried at 200°C under vacuum for 1 hour to remove residual H_2O and EtOH and to ensure the full polymerization of all

NFs. Noticeable shrinkage was observed in the NF paper, suggesting a partially incomplete polymerization or residual amounts of H_2O and EtOH within the NFs. However, the paper retains its original shape and ease of handling after drying, and no cracking or warping was observed in the sheets.

The *in situ* polymerization of TEOS that occurs in-flight during the short travel distance of 12cm from tip to collector plate, proceeds in the following general fashion in Equation 5.2:

$$Si(EtOH)_4(l) + 2H_2O(l) \rightarrow SiO_2(s) + EtOH(l) \quad (5.2)$$

In contrast to the conventional Stöber method, which may take as much as 24 hours to precipitate appreciable amounts of silica NPs, my *in situ* polymerization of TEOS in-flight is comparatively instantaneous.[9] This may be due to the relatively high surface area for solvent evaporation afforded by the formation of a nanoscale fiber immediately proceeding the Taylor cone. The absence of silica NPs in the as-spun SiO_2 NFs also confirms this rapid polymerization of TEOS in-flight. Subsequent MTR of the SiO_2 NFs proceeds as in Equation 5.3 and removal of MgO proceeds as in Equation 5.4:

$$SiO_2(s) + 2Mg(g) \rightarrow Si(s) + 2MgO(s) \quad (5.3)$$

$$MgO(s) + 2HCl(l) \rightarrow MgCl_2(aq) + H_2O(l) \quad (5.4)$$

It is worth noting that $MgCl_2$ can be recycled back into Mg via electrolysis, which is a common industrial route for producing Mg from brine.[10] The Mg reduction route operates at a much lower operating temperature (700°C) than carbothermic reduction, which requires electric arc furnaces operating at >2000°C. Carbothermic reduction is the predominant method used to produce metallurgical grade Si, but it is not a carbon neutral

process in itself. Conversely, Mg reduction produces a solid, environmentally benign, and recyclable MgO product at much lower operating temperatures.

SEM imaging in Figure 5.2a and 5.2b shows the morphology of as-spun SiO_2 NFs. XRD data in Figure 5.2e reveals the amorphous nature of the as-spun SiO_2 NFs. There is no evidence of nanoparticle-like SiO_2 structures, which are commonly produced via the Stöber method; instead, the SiO_2 NFs are an amorphous, solid network of silica.[8] SiO_2 NF paper is then cut into strips and loaded into steel-capped brass union Swagelok reactors with -50 mesh Mg powder in a SiO_2:Mg weight ratio of 1:1. This setup is very similar to that used in the previous chapter, but no salt is used in this reaction due to the generous spacing between fibers. Salt is used in powder-based MTR due to the dense packing of reactants, whereas electrospun SiO_2 has very large spaces in between the fibers for heat dissipation. The reactors are sealed in an Ar-filled glovebox (0.05 ppm O_2) and immediately transferred to an MTI GSL1600X quartz tube furnace. The furnace is purged with Ar and heated at 5°C/min to 700°C and held for 2 hours to ensure complete reaction of Mg and SiO_2.

A 2 hour reduction corresponds to a yield of 43.2%, which is very near the theoretical yield of Si from SiO_2 (46.7%), as in Figure 5.3a. Beyond this time only marginal gains in yield are achieved, thus it is not necessary to reduce for longer periods of time. Yield data was calculated by measuring the weight of the etched SiNF paper in comparison

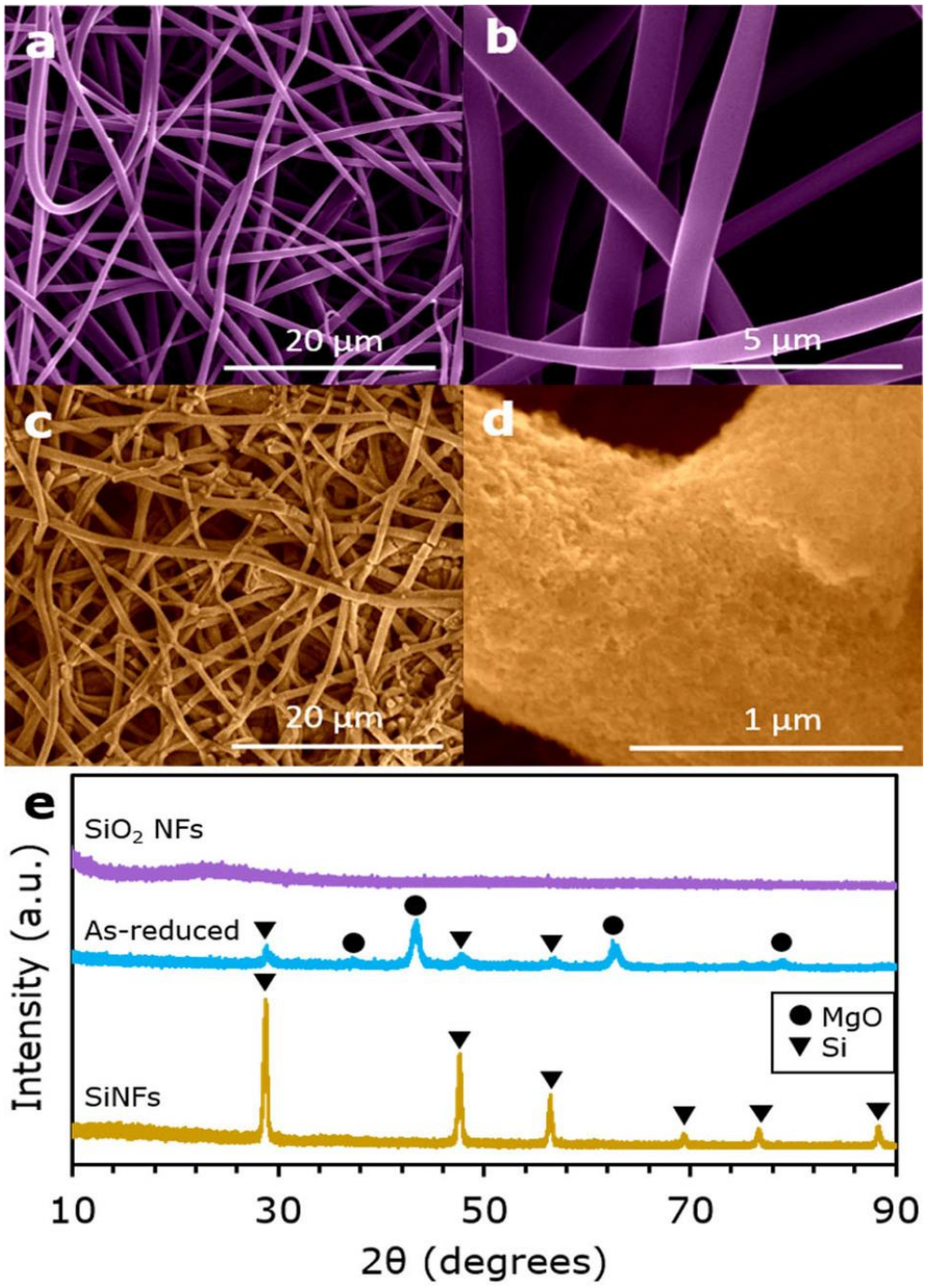

Figure 5.2 SEM images of (a) SiO_2 NFs after drying, (b) SiO_2 NFs under high magnification (c) SiNFs after etching, and (d) SiNFs under high magnification. (e) XRD analysis of NFs at select synthesis steps.

to the weight of the original SiO_2 NF paper. XRD data in Figure 5.2e reveals the existence of both MgO and Si, as expected, in the as-reduced SiNF paper. The reduced NF paper is submerged in 2 M HCl for 3 hours to remove the reaction products MgO and possibly Mg_2Si. No evidence of SiH_4 was observed, suggesting minimal or no Mg_2Si was formed. Etched SiNF paper assumes a brownish-yellow color as in Figure 5.1c. After rinsing the SiNF paper several times in EtOH and H_2O, the sheets are dried under vacuum at 105°C overnight. SiNF paper after etching can be seen in the SEM images in Figure 5.2c and 5.2d.

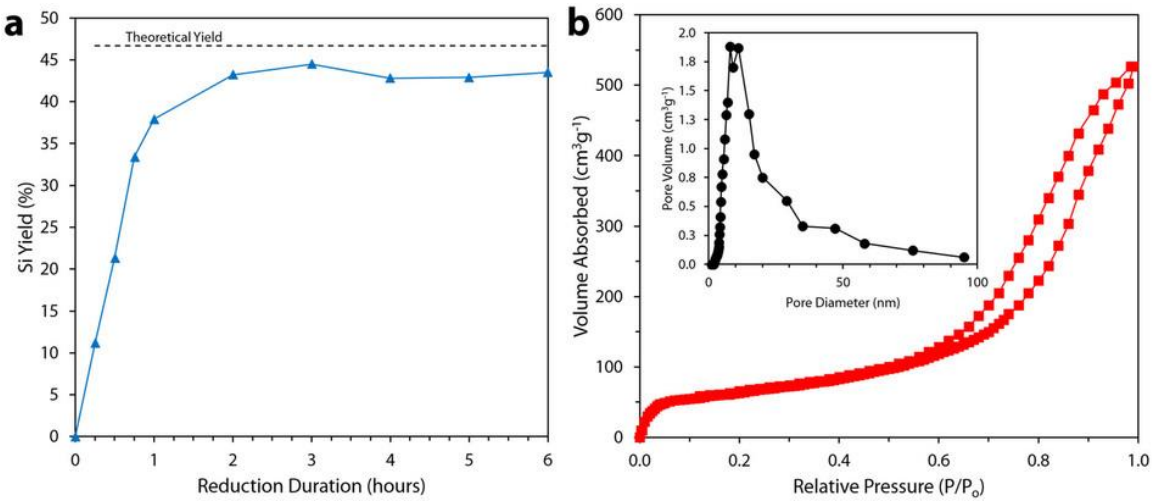

Figure 5.3 (a) Yield data for SiNF paper as a function of reduction time. (b) BET surface area measurements of SiNF paper with type IV N_2 sorption isotherms and inset showing the distribution of pore diameters.

In contrast to the solid SiO_2 NFs, SiNFs have a noticeable porosity that exists throughout the diameter of the fiber, as evidenced in the fractured SiNF in Figure 5.2d. This porosity is derived from the selective etching of MgO and possibly Mg_2Si sites. XRD data in Figure 5.2e reveals the existence of crystalline Si after etching of reaction products.

BET surface area measurements in Figure 5.3b confirm the existence of a large population of mesopores centered around ~10 nm and a relatively high surface area of 281 $m^2 g^{-1}$. The pore distribution is in good agreement with the TEM images in Figure 5.4.

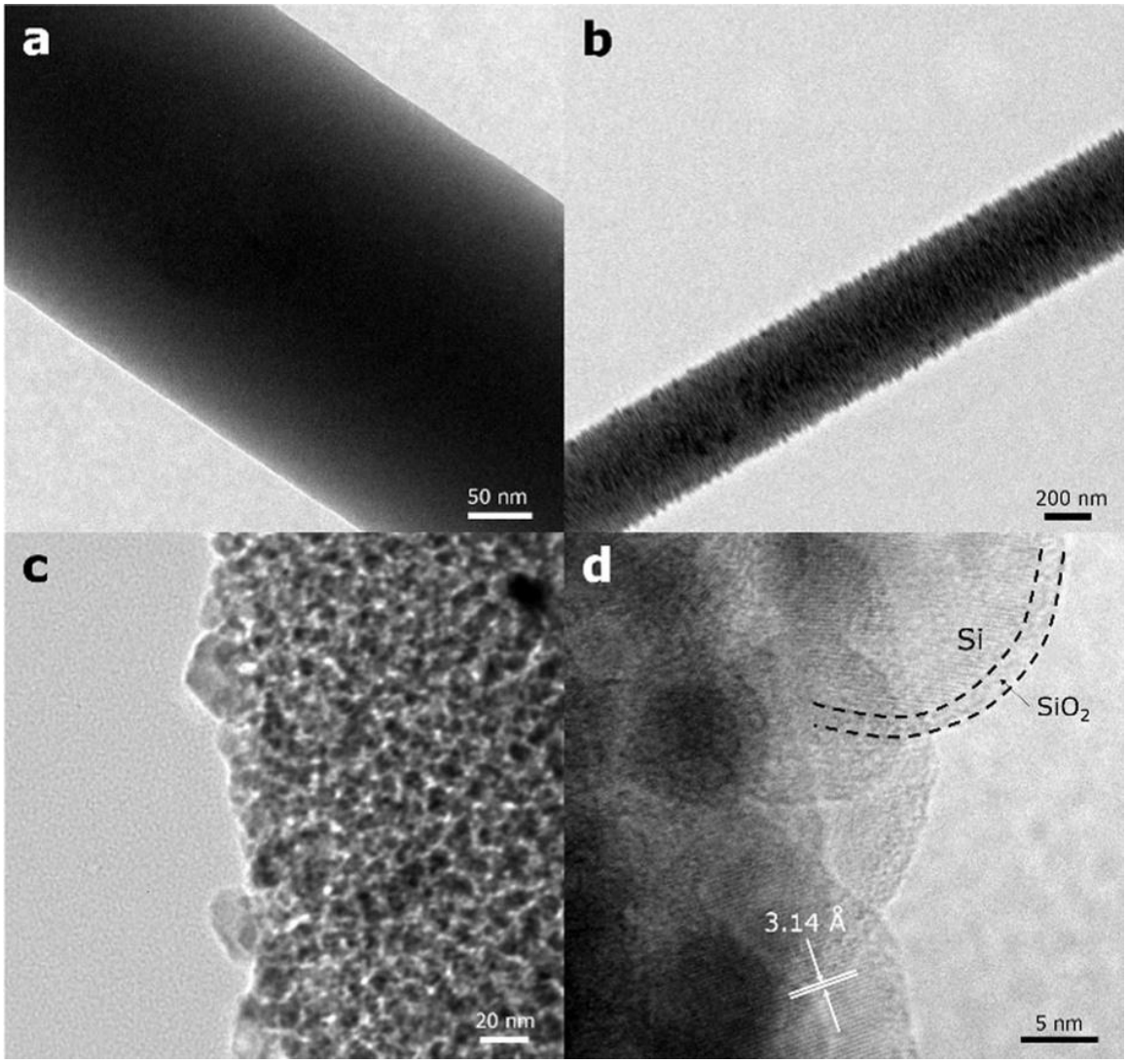

Figure 5.4 TEM images of (a) SiO_2 NF after drying, (b) SiNF after etching, (c) SiNF after etching showing porosity. (d) HRTEM image of SiNF showing 3.14 Å lattice spacing of Si(111).

TEM imaging in Figure 5.4 reveals the morphology of the fibers before and after Mg reduction. No porosity is observed in the SiO_2 NFs, as in Figure 5.4a, which reveals a uniform solid fiber. After reduction and etching the SiNFs assume a highly porous morphology as evidenced in Figure 5.4b and 5.4c. This porous structure is present throughout the thickness of the fibers, which was previously observed in the SEM images in Figure 5.2d and 5.2e. The HRTEM image in Figure 5.4d reveals the presence of not only silicon nanoparticles (SiNPs) but also the existence of a native SiO_2 shell on all SiNPs with a thickness of 1–2 nm. The SiO_2 shell may not only serve to mitigate volume expansion effects experienced by the SiNPs during lithiation, but it is also a lithiatable shell with a theoretical reversible capacity of 1961 mAh g^{-1}.[11,12] The diameter of the interconnected SiNPs that comprise the SiNFs are 8–25 nm, which is well below the critical size for the fracture of Si during lithiation. The small size of the SiNPs also reduces the bulk diffusion length for Li into Si.

5.3 Electrochemical Characterization of SiNFs

Due to silicon's low conductivity, we applied a ~4 nm carbon coating to all SiNF paper electrodes to enhance the surface conductivity of the electrodes. The carbon coating process was proven in our previous work and the effects of the thickness or crystallinity of the carbon coating on performance are beyond the immediate scope of this investigation.[13] The advantages and limitations of a carbon coating have been extensively studied in both anode and cathode settings.[14-16] SiNF paper was loaded into a quartz tube furnace in a quartz boat and heated to 950°C in 15 minutes under a flow of Ar:H_2 at 700 torr. At 950°C,

C_2H_2 was introduced for 15 minutes and then the system was cooled to room temperature under flow of Ar:H_2. The C-coated electrodes assume a black color as in Figure 5.1d. Weighing after C-coating reveals a carbon content of ~18.5% with the remainder corresponding to Si. C-coated SiNF paper electrodes were used as-is without the addition of acetylene black or a binder and were cut down to fit inside of 2032-type coin cells. Li metal was used as the counterelectrode with a 1:1 EC:DMC (v:v) electrolyte with a 3% vol. VC additive for improved cycle life, and Celgard PP was used for the separators. Charge-discharge cycling was performed on an Arbin BT300 and CV and PEIS measurements were performed on a Biologic VMP3. All capacity values were calculated on the total electrode weight (carbon + silicon).

Charge-discharge cycling in Figure 5.5a reveals the excellent performance of the C-coated SiNF electrodes over 659 cycles, with minimal capacity fading after the first 20 cycles. Even after 659 cycles, the SiNF electrodes can deliver a reversible capacity of 802 mAh g^{-1} with a CE of 99.9%. We attribute this excellent stability to the internal porosity of the SiNFs, which allows for internal volume expansion of the small SiNPs. This internal expansion of Si within the SiNFs effectively preserves the crucial SEI layer that coats the outside of the SiNFs. The existence of the native oxide shell and C-coating also contribute to mitigating volume expansion related effects through creation of a buffer layer. For comparison, cycling data for bare uncoated SiNFs is presented in Figure 5.5a to emphasize the importance of the C-coating process. The capacity rapidly decays below the theoretical capacity of graphite within 100 cycles when no coating is present.

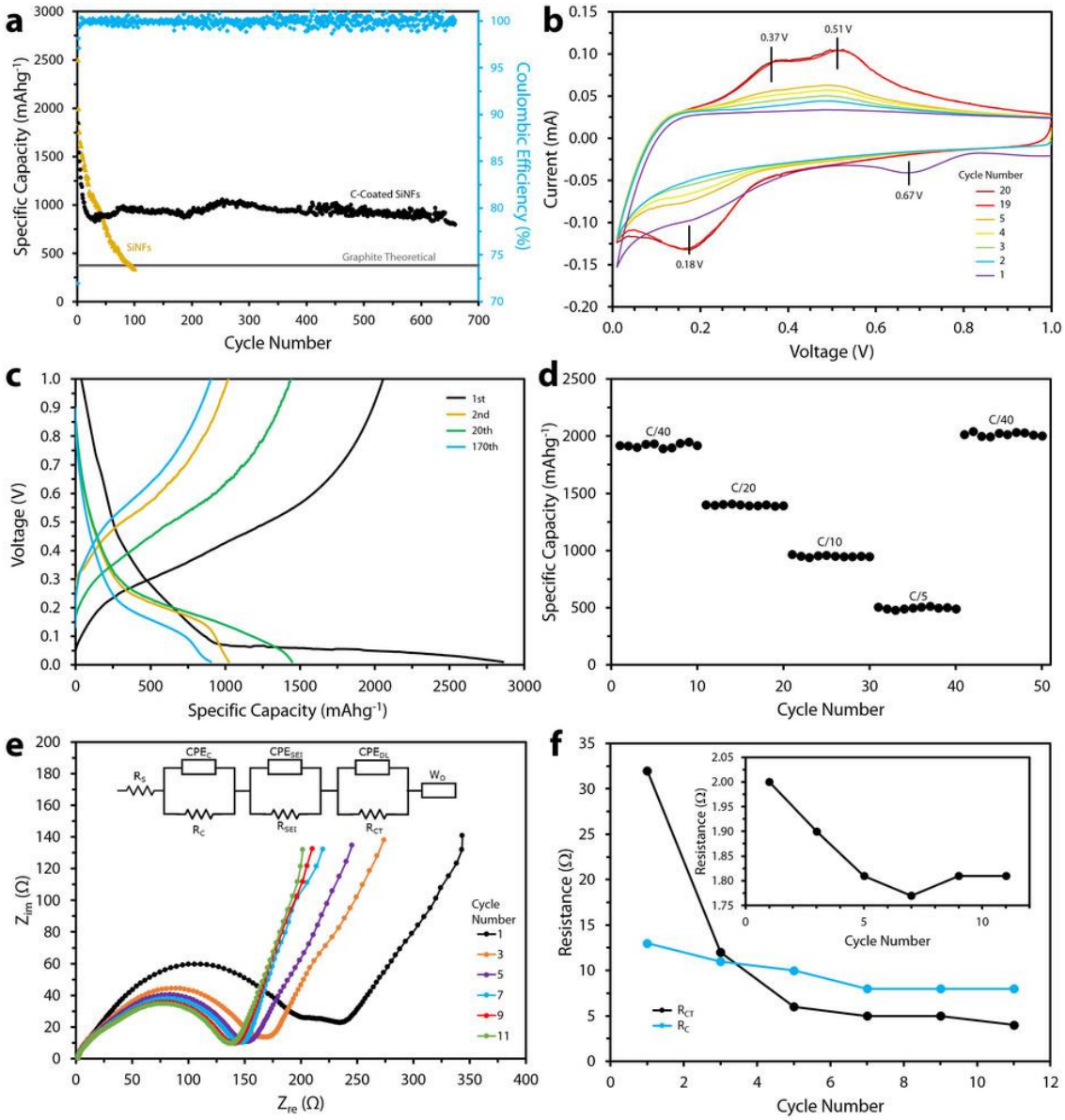

Figure 5.5 (a) Cycling data for C-coated SiNFs compared to uncoated SiNFs at C/10 (1C = 4 A g^{-1}). (b) Cyclic voltammograms for select cycles for C-coated SiNFs using a scan rate of 0.05 mV s^{-1} (c) Charge-discharge curves for select cycles for C-coated SiNFs. (d) C-rate data for C-coated SiNFs at select rates. (e) PEIS curves for select cycles for C-coated SiNFs with inset showing equivalent circuit used for modelling. (f) Resistance data for select cycles for C-coated SiNFs, with inset graph displaying ESR values.

CV measurements in Figure 5.5b demonstrate the activation process of the electrodes over the first 20 cycles. The 19th and 20th cycle curves largely coincide with each other, which signals the stabilization of the electrode. This activation process may be due to the gradual lithiation of the native SiO_2 shell and SiNPs located in the interior regions of the NFs.[17] The peak associated with the formation of SEI occurs at 0.67 V and is non-existent in subsequent cycles. Peaks closely associated with the dealloying (0.51 V and 0.37 V) and alloying (0.18 V) of Si sharpen with increased cycling, confirming the existence of the activation process. After activation for 20 cycles to allow for capacity stabilization, C-rate testing was performed on C-coated SiNFs, as in Figure 5.5d. Even up to the C/5 rate, C-coated SiNFs outperform the theoretical capacity of graphite.

The 1st cycle is performed at C/40 and the 2nd at C/20 in order to allow for activation of a majority of the active material while fostering the formation of a well-structured SEI. The capacity of SiNF paper anodes is slightly lower compared to other published silicon anodes on a pure active material basis due to the thick nature of the electrodes and large diameter of some NFs. However, SiNF paper electrodes have the remarkable benefit of having no metallic current collectors or polymer binders. When the copper foil weight is taken into account in the slurry-based electrodes, the capacity is significantly lower than reported. Additionally, all of my capacity values are reported on a total electrode weight basis, unlike much of the reported values in literature which exclude weight contributions of carbon additives, binders, or current collectors. In this sense, SiNF electrodes outperform the slurry-based electrodes if the weight of the copper foil is taken into account. The SiNF paper has a loading of Si in excess of 80% by weight and is a completely binder-

free approach. SiNF paper electrodes demonstrate excellent CEs between 99–100% after the first three cycles. Charge-discharge curves in Figure 5.5c are in good agreement with the CV curves and demonstrate the low discharge potential of the SiNF electrodes. PEIS measurements in Figure 5.5e also coincide with the activation process of the electrodes during initial cycling.

To prove the superiority of free-standing C-coated SiNF anodes to that of other electrospun slurry-cast anodes in terms of gravimetric capacity, I provide the following example. Jeong *et al.* recently synthesized a core-shell structured SiNPs@TiO_{2-x}/carbon composite Li-ion anode material via electrospinning.[18] However, the long-range 3D nanofiber network produced during electrospinning is destroyed via turning the fibers into a powder which is then cast in the traditional slurry cast method onto Cu foil. A 12 mm diameter Cu current collector disk with a thickness of 10 µm corresponds to a weight of 10.133 mg. Additionally, carbon black and an inactive polymer binder were added which constitute 10 wt.% each of the electrode. Their reported capacity of 939 mAh g^{-1} is solely based on the active material weight and excludes the weight contributions of the Cu foil, carbon black, and polymer binder. With a reported maximum loading of 3 mg of active material, this corresponds to a capacity of 2.817 mAh. Taking into account the 10 wt.% contributions of the polymer binder and carbon black (0.375 mg each), plus the 10.133 mg Cu foil, the actual capacity of the entire anode is 202.7 mAh g^{-1}. Comparing this value to that of free-standing C-coated SiNF anodes (802 mAh g^{-1}), it is clear that my anodes can provide nearly four times the gravimetric capacity based on consideration of the weight of all anode components.

PEIS was used to analyze interfacial and diffusion related kinetics in the SiNF electrodes in the delithiated state. The equivalent circuit used in this work, as in Figure 5.5e, contains the following major components: i) equivalent series resistance (ESR), ii) contact impedance within the active material (R_C and CPE_C), iii) impedance due to the SEI layer formation (R_{SEI} and CPE_{SEI}), iv) interfacial impedance at the surface of the NFs (R_{CT} and CPE_{DL}), and v) diffusion impedance (W_O). Constant phase elements (CPEs) are used to describe non-ideal capacitances that arise due to non-uniformity in the size and shape of the NFs. EIS data for select initial cycles is plotted in Figure 5.5e and 5.5f. All associated resistances tend to decrease initially and then stabilize, which coincides with the activation and stabilization of the electrode. Charge transfer resistance decreases the most drastically, with a 700% reduction from the 1^{st} to the 11^{th} cycle. The decrease of resistances such as ESR and R_C is a result of the electrode activation process, where the conductivity between SiNPs is enhanced. The lithiation of the native oxide shell may also enhance the conductivity between the interconnected SiNPs with cycling. The extraordinarily low ESR of these electrodes relative to other published Si anodes is most likely due to the absence of a polymer binder and existence of very large void spaces between SiNFs, which permits relatively facile Li-ion travel. The very low charge transfer resistance can be attributed to the highly conductive C-coating.

5.4 Conclusions

I have successfully demonstrated the first synthesis of a scalable carbon-coated silicon nanofiber paper for next generation binderless free-standing electrodes for Li-ion

batteries that will significantly increase total capacity at the cell level. The excellent electrochemical performance coupled with the high degree of scalability make this material an ideal candidate for next-generation anodes for electric vehicle applications. C-coated SiNF paper electrodes offer a highly feasible alternative to the traditional slurry-based approach to Li-ion battery electrodes through the elimination of carbon black, polymer binders, and metallic current collectors.

As discussed prior, TEOS is a product of a multistep synthesis process that begins with carbothermic reduction of quartzite rock, reaction with HCl to form $SiCl_4$, and finally alcoholysis of $SiCl_4$ to form TEOS. Despite this, TEOS is a relatively inexpensive, and non-toxic chemical that is widely used in the semiconductor industry. Electrospinning of TEOS using a single nozzle, as demonstrated here, produces several grams per hour even at the lab scale. MTR of the electrospun SiO_2 NFs has process yields of up to ~43%, which is very high compared to many industrial processes. All of these factors combined make this technology feasible in an industrial setting.

As discussed prior, MTR is an environmentally benign process in itself as is the electrospinning of TEOS based sols. The intermediate product, SiO_2 NFs, and most importantly the final SiNF product are both environmentally benign and non-toxic materials which is important for life cycle considerations of LIBs. Most importantly, this material technology demonstrates a significant leap in battery capacity by eliminating metallic current collectors and polymer binders. Despite numerous reports of powder-based Si anodes significantly boosting capacity, ultimately they all require heavy copper current collectors and inactive polymer binders which can reduce the actual capacity by a

factor of 4 (as calculated in this chapter). Capacity values reported in this chapter are a *true* report of the *complete* anode as it would be found in a full cell; all components (Si + carbon coat) are taken into account in the reported capacity values.

5.5 References

1 Xue, L. *et al.* Carbon-coated Si Nanoparticles Dispersed in Carbon Nanotube Networks As Anode Material for Lithium-Ion Batteries. *ACS Appl. Mater. Interfaces* **5**, 21-25 (2013).

2 Ji, L., Jung, K., Medford, A. J. & Zhang, X. Electrospun polyacrylonitrile fibers with dispersed Si nanoparticles and their electrochemical behaviors after carbonization. *J. Mater. Chem.* **19**, 4992-4997 (2009).

3 Cherian, C. T. *et al.* Electrospun α-Fe_2O_3 nanorods as a stable, high capacity anode material for Li-ion batteries. *J. Mater. Chem.* **22**, 12198-12204 (2012).

4 Zhou, X., Wan, L. & Guo, Y. Electrospun Silicon Nanoparticle/Porous Carbon Hybrid Nanofibers for Lithium-Ion Batteries. *Small* **9**, 2684-2688 (2013).

5 Lee, B.-S. *et al.* Novel multi-layered 1-D nanostructure exhibiting the theoretical capacity of silicon for a super-enhanced lithium-ion battery. *Nanoscale*, doi:10.1039/C4NR00318G (2014).

6 Wu, Y., Reddy, M. V., Chowdari, B. V. R. & Ramakrishna, S. Long-Term Cycling Studies on Electrospun Carbon Nanofibers as Anode Material for Lithium Ion Batteries. *ACS Appl. Mater. Interfaces* **5**, 12175-12184 (2013).

7 Ng, L. V. & McCormick, A. V. Acidic sol-gel polymerization of TEOS: effect of solution composition on cyclization and bimolecular condensation rates. *J. Phys. Chem.* **100**, 12517-12531 (1996).

8 Rossi, L. M., Shi L., Quina F. H., Rosenzweig Z. Stober Synthesis of Monodispersed Luminescent Silica Nanoparticles for Bioanalytical Assays. *Langmuir* **21**, 4277-4280 (2005).

9 Tadanaga, K., Morita, K., Mori, K. & Tatsumisago, M. Synthesis of monodispersed silica nanoparticles with high concentration by the Stober process. *J. Sol-gel Sci. Technol.* **68**, 341-345 (2013).

10 Kipouros, G. J. & Sadoway, D. R. The chemistry and electrochemistry of magnesium production. *Adv. Molt. Salt Chem.* **6**, 127-209 (1987).

11 Yan, N. W., Fang Zhong, Hao Li, Yan Wang, Yu Hu, Lin Chen, Qianwang. Hollow Porous SiO2 Nanocubes Towards High-performance Anodes for Lithium-ion Batteries. *Sci. Rep.* **3** (2013).

12 Favors, Z. J., Wang, W., Bay, H. H. George, A., Ozkan, M., Ozkan, C. Stable Cycling of SiO_2 Nanotubes as High-Performance Anodes for Lithium-Ion Batteries. *Sci. Rep.* **4** (2014).

13 Favors, Z. *et al.* Scalable Synthesis of Nano-Silicon from Beach Sand for Long Cycle Life Li-ion Batteries. *Sci. Rep.* **4** (2014).

14 Dimov, N., Kugino, S. & Yoshio, M. Carbon-coated silicon as anode material for lithium ion batteries: advantages and limitations. *Electrochem. Acta* **48**, 1579-1587 (2003).

15 Aurbach, D. *et al.* Review on electrode–electrolyte solution interactions, related to cathode materials for Li-ion batteries. *J. Power Sources* **165**, 491-499 (2007).

16 Fu, K. *et al.* Effect of CVD carbon coatings on Si@ CNF composite as anode for lithium-ion batteries. *Nano Energy* **2**, 976-986 (2013).

17 Liu, N., Huo, K., McDowell, M. T., Zhao, J. & Cui, Y. Rice husks as a sustainable source of nanostructured silicon for high performance Li-ion battery anodes. *Sci. Rep.* **3** (2013).

18 Jeong, G. *et al.* Core–Shell Structured Silicon Nanoparticles@ TiO2–x/Carbon Mesoporous Microfiber Composite as a Safe and High-Performance Lithium-Ion Battery Anode. *ACS Nano* **8**, 2977-2985 (2014).

Chapter 6 Full Cell LIB Applications of Nano-Si

6.1 Introduction

While the half-cell LIB configuration serves its purpose with regards to isolating the electrochemical performance characteristics of either anodes or cathodes, half-cells are not meaningful in a real-world setting. This is because half-cells using anodes (such as Si) have output voltages in a few mV with respect to Li metal. For full cell applications we desire a high output voltage coupled with a high specific capacity. The product of these two, or more specifically the integral of specific capacity with respect to voltage, gives specific energy (Wh kg^{-1}). When discussing full cell LIBs this is the meaningful value on a per weight basis. Also important is energy density (Wh L^{-1}) which is important when discussing how volumetrically dense a material is. Some materials may be very energetically dense on a weight basis, but poor volumetrically. This is an important distinction because we desire a material that does not require a large amount of weight to deliver a high amount of energy, but we also desire a material that can deliver a large amount of energy in the smallest possible volume. Portable electronics and EVs require very volumetrically dense LIBs as space is limited. Stationary applications are not as limiting with regards to the volume or weight of the LIBs, and thus other battery chemistries with lower costs can be used.

Additionally, half-cells utilize large Li wafers which allow the battery to operate with excess amounts of Li.[1-3] Therefore, materials with relatively low Coulombic efficiencies (NiO, Li metal anodes) can operate for thousands of cycles due to the relatively "limitless" supply of Li-ions.[4-6] Losses associated with poor CE due not present themselves

readily in half-cell electrochemical cycling data. Figure 6.1 below presents the predicted cycle lifetime of LIB full cells with varying CEs. For EV applications, full cells must have a CE of 99.99% or higher to allow for at least 74% capacity retention after 3000 cycles, which roughly corresponds to a lifetime of 10 years.[7] Even reducing the CE by 0.09% to 99.9% drastically reduces the lifetime of the battery with just 5% predicted capacity retention after 3000 cycles. While CE is normally an afterthought in many half-cell publications, it is of equal importance to specific energy or specific capacity in the full-cell realm.

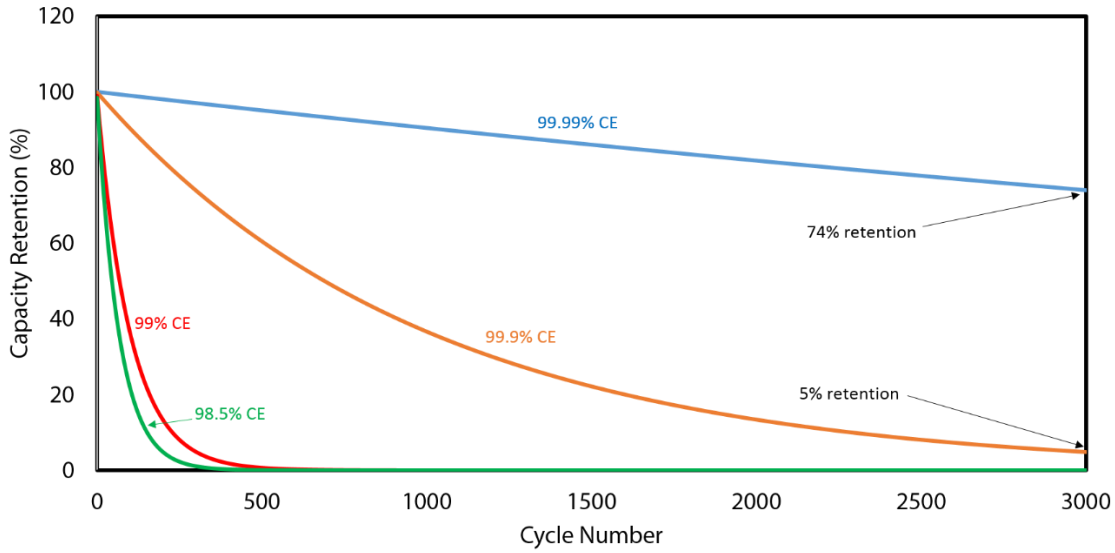

Figure 6.1 Theoretical relationship between CE and cycle number for select CE values.

Portable electronics may require significantly less battery lifetime (3 years) than EVs due to the fact that these devices are quickly phased out by newer models every year. Additionally, these tiny battery packs are relatively easy and cheap to replace (few tens of $) in stark contrast to a battery bank in an EV which can cost more than $10,000. Users

rarely keep portable electronic devices for longer than the lifetime of the battery. In these instances, full-cells may only require a few hundred cycles rather than thousands; thus, materials with lower CEs may be permitted.

In the half-cell configuration, specific capacity values (mAh g^{-1}) are almost always reported on an active material basis. This active material weight comes solely from the electrode material of interest, whether cathode or anode. In the case of Si-based anodes, the specific capacity is normally reported on a per gram of Si basis, which excludes the weights of the conductive additives, polymer binders, and metallic current collectors. This calculation also excludes the large weight of Li present in the counterelectrode which ensures ample supply of Li. In portable electronics and EVs, the weight of all of these components cannot be ignored.

Full cell capacity is also drastically different than capacities reported in half-cell publications because we must now take into account the weights of both electrodes plus the Li that has either intercalated or allowed with the anode or cathode material. Full cell capacity is calculated as follows in Equation 6.1:[8]

$$C_{total} = \left(\frac{1}{C_{anode}} + \frac{1}{C_{cathode}}\right)^{-1} \tag{6.1}$$

Based on the theoretical capacity of a commercially available $LiCoO_2$ cathode, if graphite is used (372 mAh/g theoretical) the total capacity is actually less than both the anode and cathode individually. This relationship makes sense because as we increase the specific capacity of the anode (and thus reduce the mass required) the total capacity tends towards the theoretical value of the cathode. The total theoretical capacity for the graphite:$LiCoO_2$

full cell is ~158 mAh g^{-1}, which is a sobering number in comparison to the half-cell reported values.

With this in mind, it makes sense to research higher capacity anode materials such as Si or SiO_2, which is the predominate focus of this dissertation. Using SiO_2 (theoretical 1961 mAh g^{-1}) we can achieve a theoretical capacity of ~240 mAh g^{-1} and with Si (theoretical 3759 mAh g^{-1}) we can achieve a full cell theoretical capacity of ~255 mAh g^{-1}. This is a potentially significant improvement in full cell capacity that warranted significant research into these higher capacity materials.

In addition to CE and specific total capacity of full cells, the discharge potential is of equal importance and a determining factor in the discharge specific energy and energy density. In reality, we care about the amount of energy consumed by these devices and vehicles with respect to time, which is a product of the discharge potential and specific capacity. The specific energy of full cells can be calculated as follows in Equation 6.2:[8]

$$E_{total} = V_{avg}\left(\frac{1}{C_{anode}} + \frac{1}{C_{cathode}}\right)^{-1} \tag{6.2}$$

In most cases, voltage profiles in LIBs are approximately linear and the average discharge voltage, V_{avg}, can be taken when calculating energy density. For more complex voltage profiles it may make sense to calculate the specific energy as the integral of specific capacity with respect to voltage as follows:

$$E_{total} = \int C dV \tag{6.3}$$

All specific energy values from full cells in this work are calculated via the software in the Arbin BT300, which takes the specific energy at 15 second intervals based on the average

voltage in that interval and the capacity. More specifically, the discharge potential (and charge potential) is determined by the difference between the cathode and anode potentials as in Equation 6.4:

$$V_{full} = V_{C,cathode} - V_{D,anode} \quad (6.4)$$

It is important to note that we use the charge potential of the cathode, $V_{C,cathode}$, and the discharge potential of the anode, $V_{D,anode}$, because the cathode is being lithiated (charged) while the anode is being delithiated (discharged) during discharge of a full cell LIB. In this sense, we desire cathodes with the highest possible charge potential (within limits of the electrolyte) and lowest possible anode discharge potential such that the voltage window is as large as possible. It is very important to consider that the electrolyte is the single biggest barrier to the use of high voltage cathodes materials (~5 V), since most organic electrolytes cannot be exposed to voltages greater than 4.3 V for extended periods of time without significant oxidation.[9,10]

The ideal anode material that meets this criteria is Li metal, which has a discharge potential of 0 V vs. Li/Li+.[11] Anode materials such as graphite (~0.15 V), tin (0.4 V), and silicon (0.4 V) all have relatively low discharge potentials, which means there is not a lot of room for improvement in terms of anode potential lowering.[12-14] It is not possible to have a material operating at a potential lower than 0 V vs. Li/Li+ since Li has the lowest potential vs. the standard hydrogen electrode.[1] Additionally, any operating time spent at 0 V or below simply results in Li metal plating. The only room for improvement in terms of operating voltage lies within the cathode side so long as improvements in electrolytes afford operation at voltages exceeding 4.3 V. The discussion of cathode improvements is

beyond the immediate scope of this work. Summarizing, we desire a full cell system that can deliver a high specific energy with a high CE.

Construction of a half cell LIB is much simpler than a full cell because the amount of active material is of no concern due to the essentially unlimited supply of Li. This unlimited supply of Li means that the Li counterelectrode has significantly greater capacity than the electrode being characterized. In this sense, there is no need to balance the capacity of the anode and cathode. Balancing of the LIB full cell with the correct ratio of anode to cathode active material weight (and, thus, anode capacity to cathode capacity) is very important in the full cell setting. This is especially important when pairing high capacity anodes with relatively low capacity cathodes such as $LiCoO_2$, $LiFePO_4$, etc.[15,16] The benefit of using high capacity anodes such as Si and SiO_2 lies in the fact that less anode weight is required, thus thinner electrodes can be used and the overall weight of the cell is reduced as in Figure 6.2:

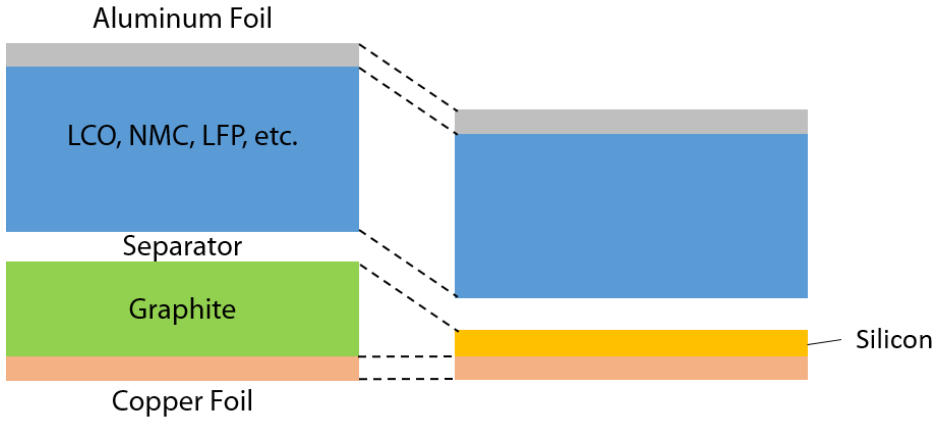

Figure 6.2 Schematic representation of low and high capacity anodes and their sizes.

The use of thinner electrodes means less material requirement and lower cost as well. For example, a commercial $LiCoO_2$ can deliver on average 140 mAh g^{-1} reversibly. If we assume a loading density of 25 mg cm^{-2} and a 1 cm^2 disc then we can reasonably expect a reversible capacity of 3.5 mAh. In order to maximize the use of this capacity, we need to create an anode with a corresponding amount of Si.

6.2 Full Cell LIB Preparation and Characterization using Nano-Si

In a full cell LIB, either the cathode or anode must contain the source of Li that will drive the battery to make it rechargeable. The amount of Li found in the electrolyte is not sufficient enough to supply enough lithium for both electrodes. Hence, prelithiation, or lithium injection prior to cell fabrication, must be used to provide ample Li for the full cell to operate with meaningful performance. Next-generation cathode materials such as sulfur or MoO_3 do not contain any lithium and must therefore be lithiated chemically (Li_2S) or electrochemically.[17] Cathodes materials are generally easier to lithiate than anodes given anodes require a much more reactive Li source; this is the basic operating principle of the Li-ion battery given the spontaneous movement of Li from the anode to cathode.[18] Prelithiated anodes are generally unstable in ambient conditions (Li_xSi for example) and are highly reactive with moisture or oxygen.[19]

Prelithiation was attempted in this investigation via molten Li metal in a Swagelok-type reactor. Briefly, Li metal wafers were heated to 600^{o}C (well above the melting temperature of Li: 180.5^{o}C) in the presence of SiNF paper electrodes. Li metal and SiNFs were placed on opposite sides of the reactor to avoid direct contact. It was noted that when

Li metal came into direct contact with Si the structure was completely destroyed. A crystalline Si wafer chip was used as a control in one prelithiation run, and the wafer was completely destroyed when Li metal contacted the wafer directly. In lieu of a wafer, a fine powder of Si was observed all over the reaction chamber. This is quite troublesome when attempting to preserve a controlled morphology such as SiNFs. Li metal, when molten, tends to creep up the walls of the reactor to spread itself out evenly and is a very corrosive substance in the molten state; as evidenced by the complete pulverization of the Si wafer chip. The reaction was very uncontrollable due to the non-repeatability of lithiating SiNFs despite similar reaction conditions. Lastly, this reaction is highly dangerous given Li vapor and molten Li metal are incredibly reactive and could pose serious danger if exposed to ambient air; this poses serious issues with regards to scalability.

For the purposes of proof-of-concept, prelithiation was performed electrochemically via assembling nano-Si electrodes into half cells using Li metal counterelectrodes. This method of lithiation is highly controllable and the amount of Li metal injected into the electrode can be calculated exactly based on Coulomb's law. Lithiation was accomplished via a slow galvanostatic (C/40) charge to 0.01 V followed by a potentiostatic (0.01 V) charge until the ambient current dropped asymptotically towards zero (Figure 6.3). At 0.01 V we expect Li and Si to alloy into a crystalline, metastable $Li_{3.75}Si$ phase, which is the maximum Li insertion into Si at room temperature.

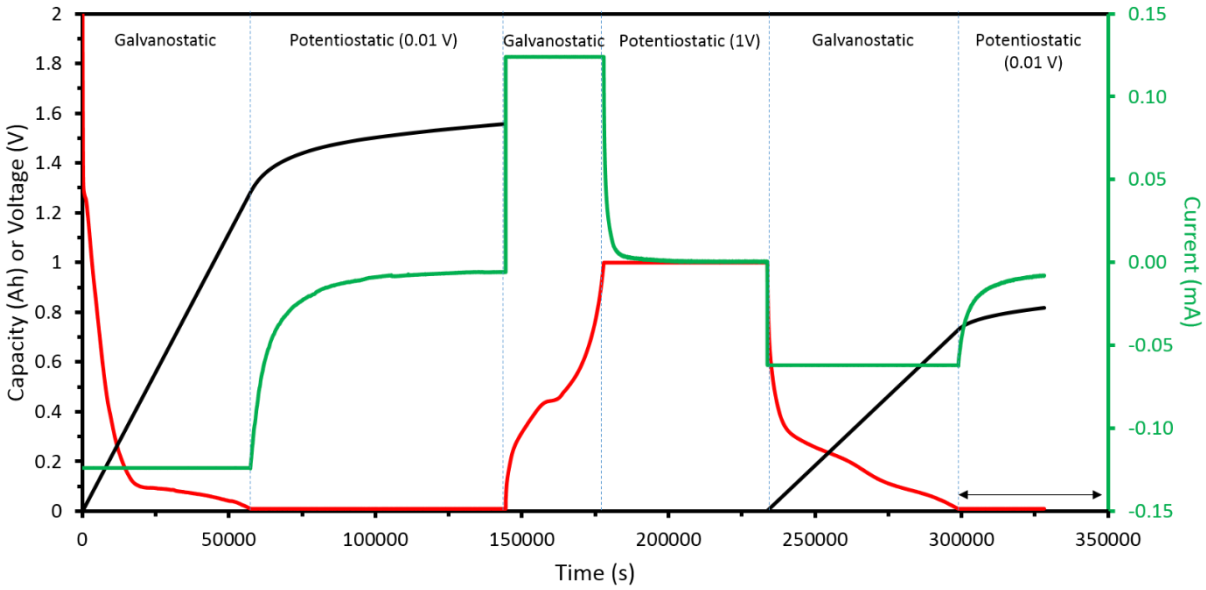

Figure 6.3 Prelithiation scheme for nano-Si based anodes showing charge-discharge curves, current response, and capacity.

Nano-Si from sand was tested versus select cathode materials, both commercial and in-lab synthesized. LCO, NMC, and LFP commercial cathodes were tested in the full cell configuration with nano-Si that was prepared via a rapid thermal treatment of the PAA binder. In previous chapters, carbon coating was performed via CVD using acetylene as a carbon precursor. In this chapter, carbon coating was performed in very similar conditions but without acetylene flow. Instead, LIB electrodes containing nano-Si were synthesized first using as-synthesized nano-Si powder and PAA binder in a 3:2 weight ratio on copper foils without the addition of AB or carbon coatings. Electrodes were punched into 16 mm diameter discs, for 2032-type coin cells, and placed into an alumina boat. The alumina boat was placed into a quartz tube furnace just outside of the heat zone of the furnace. A ceramic radiation shield was placed in between the boat and heat zone of the furnace to keep the

electrodes near room temperature while the furnace was ramped in 15 minutes to 900°C. The furnace was purged with a mixture of Ar (0.180 slm) and H_2 (30.0 sccm) for 10 minutes and kept flowing throughout the carbonization process. The pressure was kept constant at 700 torr throughout the entire process. After the furnace reached 900°C, the quartz tube was slid into the heat zone of the furnace such that the boat containing the electrodes was fully exposed to the 900°C core of the furnace. The tube was held in this position for 20 minutes until the PAA was fully carbonized, and then the tube was slid back to its original position and cooled via forced convection to room temperature. This process was adopted from Hassan *et al.*[20]

In lieu of PVDF, as used by Hassan *et al.*, PAA was used due to the non-toxicity of both PAA and the ethanol solvent. Additionally, ethanol dries much faster than NMP, which is a toxic solvent used for PVDF that takes several hours of drying under vacuum to completely evaporate. When the polymer binder is rapidly exposed to the heat zone of the furnace, the polymer is dissociated into its various components, with carbon being the remaining element. Through rapid thermal treatment of PAA graphene oxide-like material is left as per the Raman spectroscopy analysis in Figure 6.4. The SEM image in Figure 6.4 visibly shows a thin layer of graphene-like material covering the nano-Si particles.

This carbonization process is much more desirable than the one described in previous chapters using CVD in acetylene is not required and the resultant electrode solely contains carbon and silicon. All of the remaining materials are electrochemically active with Li except for the copper foil. No inactive polymer binder is left; instead the graphene-like carbon acts as both a highly conductive network for electron transport, an active Li

storing material, and a mechanical binder that holds the nano-Si particles in place. This high conductivity is electrochemically confirmed via charge-discharge cycling at exceptionally high rates that were not possible using the CVD-based carbon coating technique in previous chapters. Rates as high as 6C (1C = 4 A g^{-1}) were achieved while still outperforming graphite on a capacity basis, as in Figure 6.4c. Even after 1200 cycles the rapidly carbonized carbon-silicon hybrid still outperforms graphite; this relatively high C-rate time corresponds to an actual charge-discharge time of 1-2 minutes.

Figure 6.4b demonstrates the first cycle irreversible capacity loss due to the formation of an SEI layer. Without carbonization, a higher initial charge capacity is achieved, but a larger irreversible capacity loss occurs as a result (28.2%). This is due to the fact that bare SiNPs do not have the graphene-like coating, which serves as a buffer layer for expansion and the crucial SEI layer. The carbonized anodes afford a lower initial charge capacity but only produce an irreversible capacity loss of 21.3%. The difference of ~7% is a significant savings in Li despite the lower initial capacity. Once Li is irreversibly lost to SEI formation and other reactions it is no longer electrochemically active.

Figure 6.4d demonstrates the comparison between carbonized and non-carbonized nano-Si anodes. Without the carbon coating the anodes produce an initial charge capacity of more than 4000 mAh g^{-1}. This exceeds the theoretical capacity of Si, but it is possible due to the large irreversible formation of SEI. Even at the C/10 rate the non-carbonized anodes quickly degrade within a 100 cycles to below the reversible capacity of graphite. This is unacceptable for portable electronics and EV applications. Conversely, the carbonized anodes produce an initial charge capacity of ~3000 mAh g^{-1} but do not show

significant capacity fading in subsequent cycles. This proves that a stable SEI layer forms on the carbon-silicon composite and does not significantly degrade in subsequent cycles. The undulations in capacity over time are due to changes in the room temperature throughout the day.

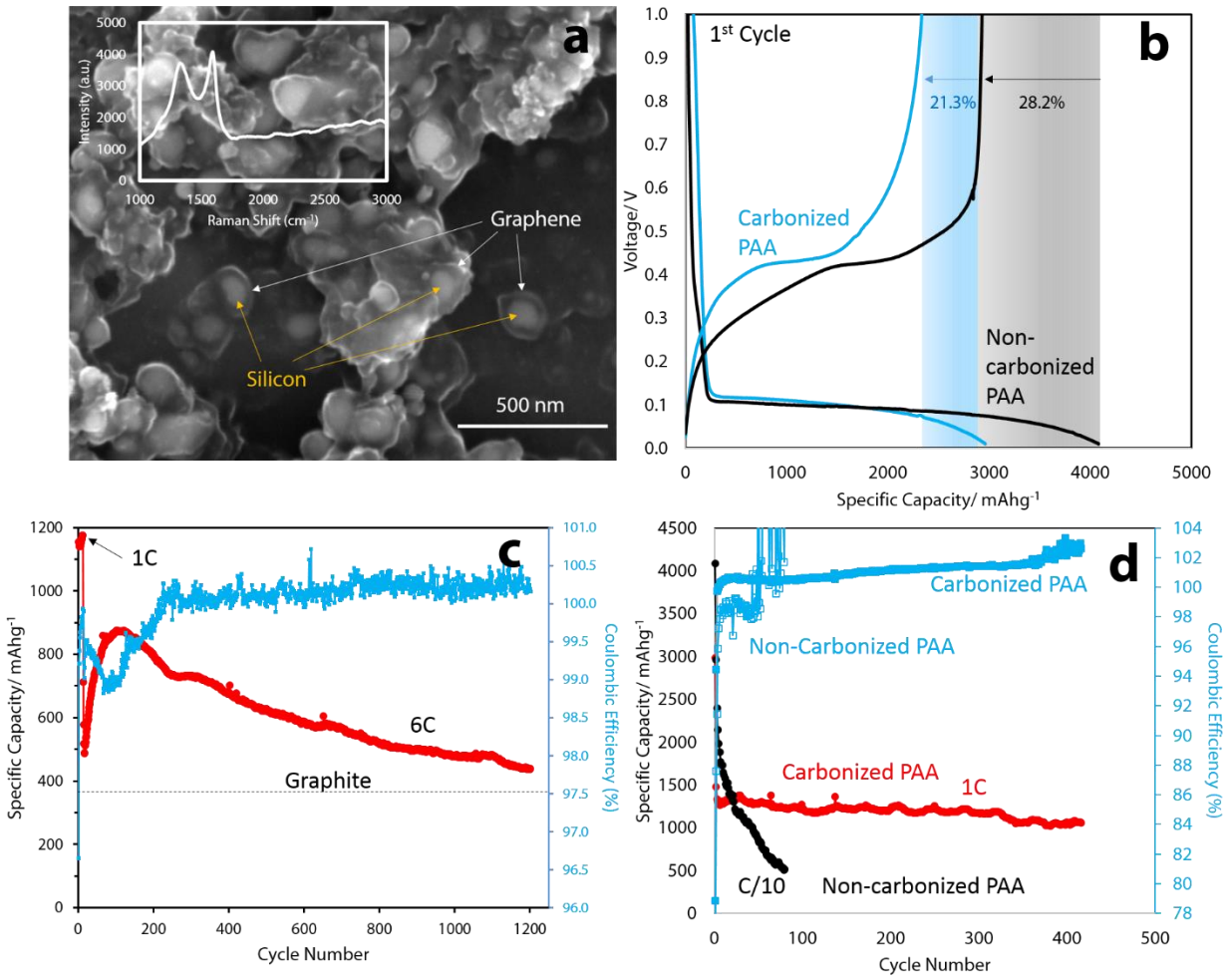

Figure 6.4 (a) SEM image of graphene-silicon composite with inset showing Raman spectra. (b) Charge-discharge profiles for carbonized and non-carbonized anodes showing first cycle capacity loss. (c) Cycling data performed at 6C (1C = 4 A g^{-1}) with first cycles performed at slower rates. (d) Comparison of cycling performance for carbonized and non-carbonized anodes.

Flash carbonized nano-Si anodes were paired with commercially available cathode materials from MTI (LCO, NMC, and LFP), which are the most common cathode materials used in devices and EVs today. Use of commercial cathodes provides a benchmark for comparison to commercially available LIBs that use graphite anodes. Figure 6.5 displays performance results for the best full cell chemistry achieved using a commercial cathode (NMC). Unfortunately only preliminary cycling data could be gathered (<100 cycles) due to the inferior quality of the cathode materials in comparison to the nano-Si anodes.

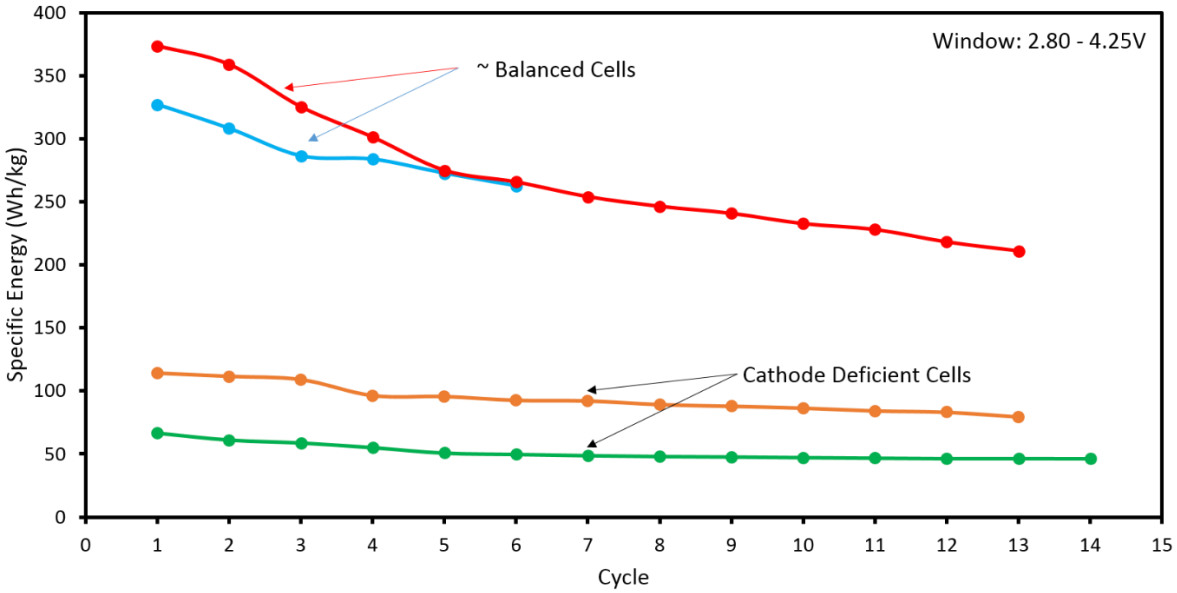

Figure 6.5 Initial cycling data for NMC-Si full cells showing comparison of well-balanced and unbalanced full cells. All cycling performed at C/10 rate (1C = 2 A g^{-1}).

Another crucial aspect of full cell construction is demonstrated in Figure 6.5, which is capacity balancing. As explained earlier in this chapter, materials with different capacities must be used in different amounts in a full cell such that each electrode of the battery can store the same amount of Li. The red and blue curves demonstrate two separate

full cells that were relatively well balanced and, thus, could deliver very high specific energies. In contrast, highly unbalanced cells that lacked sufficient cathode material weight (orange and green curves) produced significantly less energy due to the incomplete use of Li ions in the system.

Figure 6.6 below demonstrates a full cell comprising an in-lab synthesized molybdenum trioxide nanobelt (MoO_3 NB) cathode and a carbonized nano-Si anode. Briefly, MoO_3 is a potential cathode material candidate based on its high theoretical reversible capacity of 200-250 mAh g^{-1}, which is significantly higher than the reversible capacity of LCO (~140 mAh g^{-1}). Synthesis of MoO3 NBs are beyond the immediate scope of this dissertation, but can be found in my colleague's publication by Ionescu *et al.*[21] Figure 6.4 demonstrates an unbalanced MoO_3-Si full cell that was deficient in terms of cathode material weight. Despite the deficiency in cathode material, the full cell still outperformed commercial LIB packs over the initial cycles.

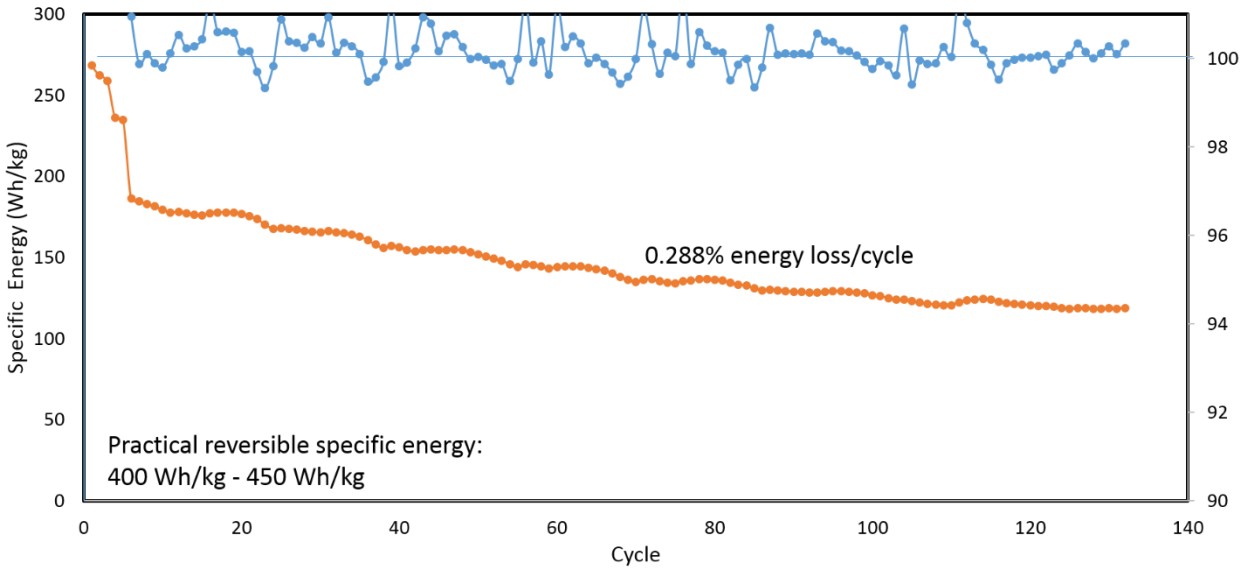

Figure 6.6 Cycling data for a MoO_3-Si full cell under a C/10 rate (1C = 2 A g^{-1}).

6.3 Conclusions

Herein, an overview of full cell fabrication was discussed and full cell data was presented for select cathode materials paired with carbon coated nano-Si. NMC-Si full cells delivered an initial discharge energy of ~380 Wh/kg, which is significantly higher than commercial LIB packs that can deliver ~110 Wh/kg. Prelithiation was thoroughly discussed as a means of introducing Li into Li-deficient systems such as the MoO_3-Si system. Preliminary results suggest nano-Si offers a boost in performance over conventional graphite even when paired with traditionally used cathode materials. This initial electrochemical testing only demonstrates cycling over a few tens of cycles based on the un-optimized cathode materials. However, a direct comparison cannot be drawn to commercial LIB packs due to the difference in depth of discharge (DoD), which is a measure of how completely discharged/charged the battery is. In all of these half-cell and full-cell analyses the DoD is near 100%, which essentially pushes the battery to its limits every cycle. Taking an LIB to its maximum electrochemical limits every cycle significantly reduces the cycle life of the battery due to changes in the electrodes.

6.4 References

1 Park, M. S. *et al.* A Highly Reversible Lithium Metal Anode. *Sci. Rep.* **4** (2014).

2 Xu, W. *et al.* Lithium metal anodes for rechargeable batteries. *Energy Environ. Sci.* **7**, 513-537 (2014).

3 Zheng, G. *et al.* Interconnected hollow carbon nanospheres for stable lithium metal anodes. *Nat. Nanotechnol.* **9**, 618-623 (2014).

4 Zhu, X.-J., Hu, J., Dai, H.-L., Ding, L. & Jiang, L. Reduced graphene oxide and nanosheet-based nickel oxide microsphere composite as an anode material for lithium ion battery. *Electrochim. Acta* **64**, 23-28 (2012).

5 Poizot, P., Laruelle, S., Grugeon, S., Dupont, L. & Tarascon, J. Nano-sized transition-metal oxides as negative-electrode materials for lithium-ion batteries. *Nature* **407**, 496-499 (2000).

6 Aurbach, D. *et al.* The Study of Electrolyte Solutions Based on Ethylene and Diethyl Carbonates for Rechargeable Li Batteries I. Li Metal Anodes. *J. Electrochem. Soc.* **142**, 2873-2882 (1995).

7 Dahn, J. *What causes Lithium-ion to die?*, (2015).

8 Yang, Y. *et al.* New nanostructured Li2S/silicon rechargeable battery with high specific energy. *Nano Lett.* **10**, 1486-1491 (2010).

9 Yang, L., Ravdel, B. & Lucht, B. L. Electrolyte reactions with the surface of high voltage LiNi0. 5Mn1. 5O4 cathodes for lithium-ion batteries. *Electrochem. Solid-State Lett.* **13**, A95-A97 (2010).

10 McMillan, R., Slegr, H., Shu, Z. & Wang, W. Fluoroethylene carbonate electrolyte and its use in lithium ion batteries with graphite anodes. *J. Power Sources* **81**, 20-26 (1999).

11 Yan, K. *et al.* Ultrathin Two-Dimensional Atomic Crystals as Stable Interfacial Layer for Improvement of Lithium Metal Anode. *Nano Lett.* **14**, 6016-6022 (2014).

12 Chen, P., Wu, F. & Wang, Y. Four-Layer Tin–Carbon Nanotube Yolk–Shell Materials for High-Performance Lithium-Ion Batteries. *Chem. Sus. Chem.* **7**, 1407-1414 (2014).

13 Yazami, R. & Touzain, P. A reversible graphite-lithium negative electrode for electrochemical generators. *J. Power Sources* **9**, 365-371 (1983).

14 Arie, A. A., Song, J. O. & Lee, J. K. Structural and electrochemical properties of fullerene-coated silicon thin film as anode materials for lithium secondary batteries. *Mater. Chem. Phys.* **113**, 249-254 (2009).

15 Cho, J., Kim, Y. J. & Park, B. Novel LiCoO2 cathode material with Al2O3 coating for a Li ion cell. *Chem. Mater.* **12**, 3788-3791 (2000).

16 Zhou, X., Wang, F., Zhu, Y. & Liu, Z. Graphene modified LiFePO4 cathode materials for high power lithium ion batteries. *J. Mater. Chem.* **21**, 3353-3358 (2011).

17 Yang, Y. *et al.* High-capacity micrometer-sized Li2S particles as cathode materials for advanced rechargeable lithium-ion batteries. *JACS* **134**, 15387-15394 (2012).

18 Liu, N., Hu, L., McDowell, M. T., Jackson, A. & Cui, Y. Prelithiated silicon nanowires as an anode for lithium ion batteries. *ACS Nano* **5**, 6487-6493 (2011).

19 Cloud, J. E. *et al.* Lithium Silicide Nanocrystals: Synthesis, Chemical Stability, Thermal Stability, and Carbon Encapsulation. *Inorg. Chem.* **53**, 11289-11297 (2014).

20 Hassan, F. M., Chabot, V., Elsayed, A. R., Xiao, X. & Chen, Z. Engineered Si electrode nanoarchitecture: A scalable postfabrication treatment for the production of next-generation Li-ion batteries. *Nano Lett.* **14**, 277-283 (2013).

21 Ionescu, R. *et al.* Synthesis of Atomically Thin MoS2 Triangles and Hexagrams and their Electrical Transport Properties. *IEEE* **13**, 749-755 (2014)